
Università di Firenze, Università di Perugia, INdAM consorziate nel CIAFM

**DOTTORATO DI RICERCA**
**IN MATEMATICA, INFORMATICA, STATISTICA**

CURRICULUM IN INFORMATICA

CICLO XXXV

**Sede amministrativa Università degli Studi di Firenze**

Coordinatore Prof. Matteo Focardi

# On image restoration via nonlinear anisotropic PDE with non-standards growth conditions

Settore Scientifico Disciplinare INF/01

**Dottorando**
Antonino Parisi

**Tutore**
Prof. Vincenzo Vespri

**Coordinatore**
Prof. Matteo Focardi

Anni 2023/2024

# Contents

# List of Figures

# List of Tables

# Introduction

The advent of the digital age and the fast evolution of Information Technology have allowed the creation of sophisticated devices for data acquisition. Hence, in recent years, various mathematicians and computer scientists have been devoted to the analysis and the interpretation of digital information, consisting of processing algorithms and implementation of paradigms. This has produced a strong interdisciplinarity in order to study and analyze acquisition techniques and visualization methods within the context of Engineering and Mathematics.
Image processing is a very broad discipline that includes techniques to analyze and modify digital images. Among these techniques there are, for example, *deblurring* (anti-blurring), *denoising* (noise elimination), *inpainting* (restoring missing or corrupted parts), *segmentation* (extraction) and *reconstruction* of surfaces. In recent years, the analysis of digital images is arousing a strong interest for the developments in various fields, such as the academic one as well as the scientific, industrial, military, medical, artistic, technological and forensic contexts.
*Enhancement* techniques are generally based on heuristic procedures that manipulate the image in order to take advantages from the psychovisual aspects of the human perceptual system. An example is the application of a deblurring function to reduce blurring on an image. These disciplines have in common the aim to extract information from the image or to improve its quality. Among the processing procedures, there are methods which play an important role, aimed at reducing the noise in each real image, a phenomenon due to the recording phase which occurs by using electronic and digital devices. Image noise is a random variation of image information. It represents an unwanted byproduct of image acquisition that adds incorrect and extraneous information. Image denoising aims to remove noise from a noisy image in oder to restore the true image. However, as noise, edge, and texture are high frequency components, it is difficult to distinguish them in the process of denoising and the denoised images could inevitably lose some details. Improving the quality of an image from the noise means to increase the perceptibility of objects in the scene by increasing the brightness difference among the objects and their background.
In this thesis, a variational approach is introduced for contrast enhancements of

color images and denoising of each spectral channel. For this aim, it is used energy functional with non-standard growth, in particular a special form of anisotropic diffusion tensor for the regularization term and a term which is inspired by the variational model of Bertalmio et al. The proposed approach does not strongly modify the histogram of the original image, preserves the global lighting sensation and shows that the hue of the main objects does not drastically change with the illumination. One of the most important advantages of this approach is that the proposed model allows to synthesize, at a high level of accuracy, noise and blur-free color images, that are captured in extremely low light conditions.
The thesis is organized as follows.
Chapter 1 presents some basic reviews about the denoising problem and the consequences due to the image acquisition by digital devices. Some classical methodologies are presented: the possibility of erasing noise is done through the computation of the grey value of each pixel via correlation between pixel/image patches. Some techniques, based on transforms, are considered: the possible noise erase is done considering that noise and image information have different features in the transformed domains. Some approaches, based on convolutional neural networks, are analyzed. Then, metrics for denoising performances and applications are described. Finally, the issue of image denoising is presented by some classical variational approaches with variable exponent or with variable nonlinearity order.
Chapter 2 deals with known variational models, based on partial differential equations (PDEs), in image processing. A generic image, corrupted by noise, is restored via the resolution of an inverse problem, that foresees the minimization of a cost functional whose terms, in some cases, are solutions of PDEs. Such an approach is widely studied in literature and it still remains an open issue. Classical techniques are first described and then some numerical results are presented: the restoration of satellite optical images using synthetic aperture radar; the denoising and deblurring of non-smooth hyperspectral satellite images; a two-level variational model to predict daily surface reflectance at Landsat high spatial resolution and Modis temporal frequency and, finally, the contrast enhancement of color images.
Chapter 3 is devoted to the original and novel aspects of the conducted research. In this chapter, a new variational model in Sobolev-Orlicz spaces with non-standard growth conditions of the objective functional is proposed. Its applications are discussed for the simultaneous contrast enhancement and denoising of color images. The main feature of the proposed model is that we deal with a constrained non-convex minimization problem in variable Sobolev-Orlicz spaces, where the variable exponent is unknown a priori and it depends on a particular function that belongs to the domain of the objective functional. Unlike the standard approach, no spatial regularization to the image gradient is applied and no color image restoration using saturation-value total variation is considered; on the contrary, we work just with

the RGB representation of color images. The aim is to increase the perceptibility of objects in the scene and the noise robustness of the proposed model albeit it makes such variational problems completely non-smooth, non-convex, and, hence, significantly more difficult from a minimization point of view.
We discuss the consistency of the variational model, provide the scheme for its regularization, derive the corresponding optimality system, and propose an iterative algorithm for practical implementations. Some accurate numerical methods have been implemented for the coercive parabolic boundary control problem, facing stability problems. There are numerous approaches to solve quasi-linear partial differential equations. As we deal with pixels in image processing, finite differences approaches and an explicit scheme of the forward Euler method are arguably the best options. For acceleration of computation, efficient Bernstein polynomials approximation could be used. The contrast scale and level in our model are adjustable, so that the proposed approach is classified as fully adaptive. Our enhancement method for color images works directly on the RGB images without any pre- and/or post-processing. The automatic adaptation of the parameters to the content of the considered image could be a future direction of research.
The main contributions of the thesis are summarized as follows:

- The variational statement for the simultaneous contrast enhancement and denoising of multispectral images in the form of minimization problem in Sobolev-Orlicz spaces with non-standard growth conditions of the objective functional.
- Rigorous substantiation of the well-posedness of the variational problem with non-standard growth functional.
- The proof of existence results to the approximation variational problems.
- The iterative algorithm for numerical implementations.
- Derivation of the first order necessary conditions for the original problem and their substantiation.
- Numerical experiments to study the performances of the new approach.

The results of the research activity have been submitted for publication to *Communications on Applied Mathematics and Computation*.

# Chapter 1

# The denoising problem

Photography has always fascinated many people and nowadays it has a great importance due to the digital technologies. The purely analogical sector made up of films and chemical agents, is now represented by the large-scale diffusion of digital photographs thanks to the evolution of information technology and the continuous development of technological devices, such as smartphones. In recent years, the analysis of digital images has a strong interest in the developments of applications, not only in the academic field but also in the scientific, industrial and military contexts.
Because of the explosion of the number of digital images, the demand for more accurate and visually pleasing images is increasing. However, the images captured by modern cameras are inevitably degraded by noise, which leads to deteriorated visual image quality. Image noise is a random variation (it is not inside the captured object) in the brightness or color information in the image. It can be produced by the sensor and the various circuits of a scanner or digital camera. Image noise is an unwanted by-product of image capture that adds extraneous and incorrect information. The magnitude of image noise can range from almost imperceptible specks on a digital photograph taken in good light, to images that can be almost entirely noise. The main sources of noise in digital images arise during acquisition. For example, sensor noise caused by low light and/or high temperature, and/or transmission channel, compression or for example electronic circuit noises.
Image denoising is to remove noise from a noisy image, so as to restore the true image. However, since noise, edge, and texture are high frequency components, it is difficult to distinguish them in the process of denoising and the denoised images could inevitably lose some details. The purpose of digital image enhancement is to sharpen elements such as edges, outlines, or provide more contrast to the image itself.
Researchers work to reduce noise without losing image features (edges, corners, and other sharp structures). Image denoising plays an important role in modern

image processing systems. In fact, image denoising is a classic problem and has been studied for a long time. However, it remains a challenging and open task.

## 1.1 Problem statement

The problem, described in [1], is shortly represented as:

$$y = x + n \tag{1.1}$$

where $y$ is the observed noisy image, $x$ is the original image unaffected by noise, and n is the noise which is represented as an additive white Gaussian noise (AWGN) by a value of standard deviation $\sigma_n$ which is estimated through different approaches, among which:

- median absolute deviation [2];
- block-based estimation [3];
- principle component analysis (PCA) based methods [4].

The main objective is to achieve a reduction of noise in the image acquired through digital systems and to minimize the loss of information of the starting image to reach the improvement of the signal-to-noise ratio (SNR).
The finalities, that the image denoising techniques aim to achieve, are:

- edges should be detected, recognized and protected without blurring;
- textures should be preserved;
- incorrect and extraneous information should not be added.

## 1.2 Image denoising techniques

Possible image denoising methods are grouped into [5]:

- classical denoising method;
- transform techniques in image denoising.

They are described by the scheme in Fig. 1.1.

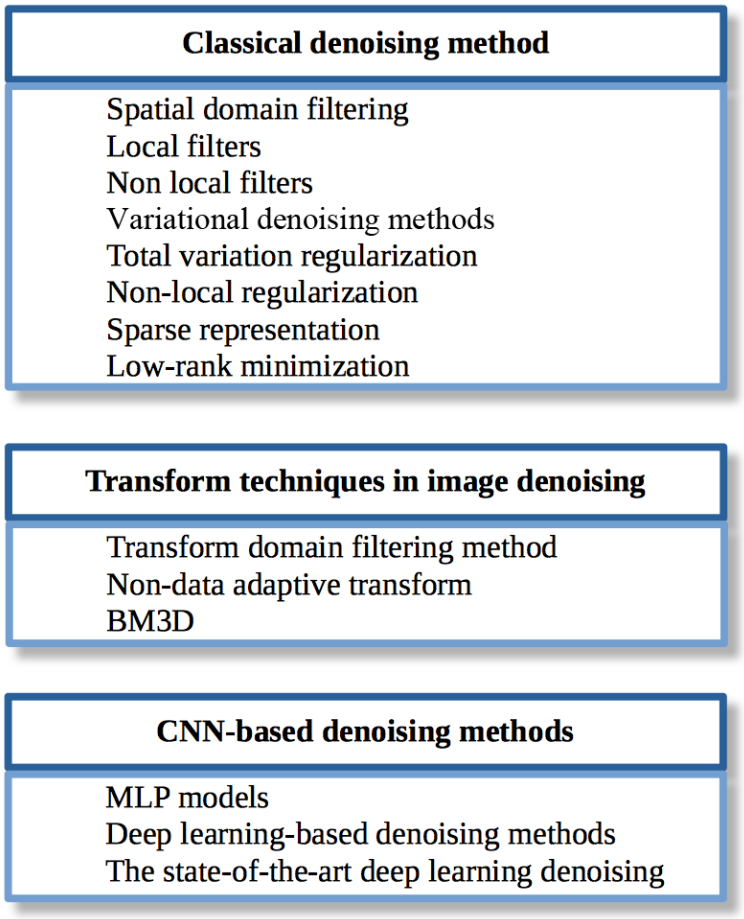


Figure 1.1: Classification of image denoising methods.

### 1.2.1 Classical denoising method

The methods, that belong to this category and are traced back to the spatial domain, tend to eliminate noise by calculating the gray value of each pixel through the correlation between pixels/image patches in the original image [6]. Spatial domain methods in turn are divided into two further categories: spatial domain filtering and variational denoising methods.

#### Spatial domain filtering

It is generally believed that filtering is one of the main mean of image processing and the solution to eraise noise from the image, i.e. one proceeds with the suppression of the unwanted variation in the intensity values of the pixels. Filtering

has been long used for smoothness, sharpness, edge detection, and contrast enhancement. If an algorithm is applied in a spatial domain, the set of operations are directly employed on the image matrix, whereas in the case of transformation domain filtering, the image matrix is first mapped into the corresponding transformed coefficients and then performed a further threshold.
Depending on the selection mode of the candidate pixels used in the filtering process, the filter is classified as local filter or non-local filter and again in linear filters and non-linear filters.
Linear filters aim to remove noise in the spatial domain, but fail to preserve the texture of the original image. Average filtering [10] aims in the reduction of Gaussian noise. However, in the case of images with high noise, it can lead to excessively uniform images [11]. To deal with this drawback, Wiener filtering [12, 13] is used. By using non-linear filters, such as median filtering [10, 14] and weighted median filtering [14], noise is significantly reduced. Among nonlinear filters, bilateral filtering [16] is widely used for image denoising because it preserves edges and reduces noise. The intensity value of each pixel is replaced with a weighted average of the intensity values of the adjacent pixels. However, this filter has a drawback regarding its efficiency. In fact, the execution requires a time of the order of $O(Nr^2)$, which is quite onerous when the kernel radius $r$ is large.
Spatial filters generally manage to eliminate noise to a reasonable extent, but this comes at the expense of possible blurring of the image which, in some cases, blurs the edges.
The underlying principle of an image denoising algorithm is that the noise is uncorrelated between pixels while the pixel intensities of the real signal are correlated with each other [7]-[9].

### Local filters

The filters, that belong to this category, foresee to eliminate the noise from one or more neighboring pixels for a portion of the image, according to a limited spatial distance. However, when the filter is applied over the whole range of pixels in an image, it is called non-local filtering. Among the best known local filters, there are the Gaussian filter, Least Mean Square filters, Bilateral filter, Weiner filter, SUSAN filter, Anisotropic Diffusion filter, Rank filter, Steering Kernel Regression (SKR), Metric Steering Kernel Regression and Trained filters [34].
Among the Linear Translational Invariant filters, the simplest is one based on the calculation of the average between the neighboring pixels in a delimited portion of the image. Considering the image matrix and the filter mask, the calculation generates an output value equal to the average one obtained from the pixels contained within the area in consideration. This type of spatial filtering is the simplest type of noise removal. However, it often results in smoothing of edges,

image degradation and loss of detail [7, 8, 34], see the scheme in Fig. 1.2 for a short review. The Gaussian filter [35] and the Weiner filter [13], [12] also belong to this

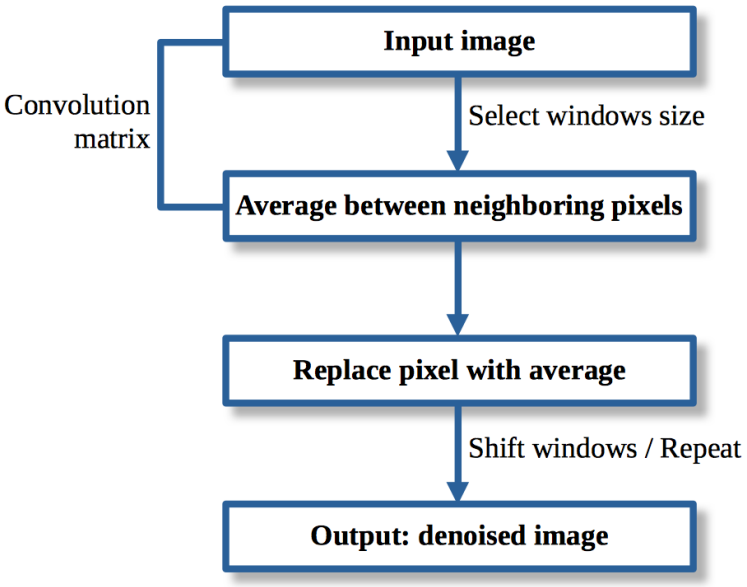


Figure 1.2: Spatial filter based on averaging.

category, but they do not use the technique of calculating the average between neighboring pixels. Wiener filters are a class of optimal linear filters which provide the estimation of a sequence of signals starting from another correlated sequence. Gaussian filters, on the other hand, belong to the category of local filters and are isotropic and linear, and they are often applied in the image denoising. Gaussian filtering is considered important in the literature as its mathematical features are easily specified and this has allowed the birth of many local denoising filters in order to improve their quality and reduce the possible blurring at the edges. A peculiarity of the Gaussian filter is that the weight of the filter decreases when the distance from the center increases. This produces blurred edges [34]. While these filters are a simple and time-efficient solution, they often tend to remove important structural information and edge details for the image analysis. For this reason, new solutions and innovative ideas are born in the field of non-linear filters. Valid examples in the literature are median filtering [8, 14], weighted median filter [15] and Rank filter [36].

Thanks to Perona and Malik [21], anisotropic diffusion filtering (ADF) are proposed with the aim of solving the shortcomings in the previous methods, such as the reduction of the Gaussian blur, preserving the edges, the details of the image and the geometry of the image. This filter is based on a nonlinear diffusion process,

and in particular on solving the anisotropic heat equation which is a second order partial differential equation. It applies an inhomogeneous process to lessen the diffusivity at locations of edges and carries out a diffusion process in homogenous regions or regions with slight intensity variations. The ADF is effective especially in medical diagnosis, where the presence of incorrect and extraneous information usually masks the interpretation of the image [37].
Nowadays, there is a consistent documentation on PDE-based anisotropic models which suggest several modifications to obtain a steady state solution for the resolution of the staircase effects problem [23], [29], [38]-[43]. Qui et al. [44] propose a robust non-local derivative based ridge detector, as well as Catte et al. [23] who consider the beforehand pre-denoising. Scholars have proved that the higher order partial differential equations produce effective results in reducing staircase effects, and this is also due to fourth order partial differential equations (FPDE) that imply satisfactory denoising results [45]-[47]. From the study of the FPDE, Lu and Tan [48] proposed a denoising model that offers better results in terms of preservation of edges and features. Another noteworthy work is by You-Kaveh [49] who, based on FDPE, consider the use of a piecewise harmonic function in order to reduce the noise in an image. The FPDE sector is the object of study and the basis of many researches which have shown that the high frequency coefficients of the image decay much faster than the models based on the PDEs, sometimes producing noise attributable to small spots and over-smooth the step edges.
Another algorithm, based on PDEs and based on combination of local gradient, gray level variance and edge stopping function, is the one proposed by Chao and Tsai [50]. The model introduced by Gilboa et al. [51] aims to achieve edge enhancement by suppressing noisy pixels in smoother sections through the use of an adaptive diffusion process using forward and backward diffusion processes.
In the literature there is a large number of works that are based on the ones by Perona and Malik. They address non-linear filtering techniques in order to realize set levels of directions and gradients resulting in better edge preserving ability as compared to other regularization based filters.
The work by Rudin and Osher in 1992 propose a method to remove noise from homogeneous areas of the image but without interfering with the edges. This is due to the total variation minimization method in which the authors propose to recover original images as solutions of a constrained minimization of the total variation of the images [25]. The corrected image is obtained by minimizing the energy variation between the original and the corrected image. Other solutions foresee Total Variation (TV) based minimization problems. Such problems preserve information along straight edges but, at the same time, have some disadvantages: textural information is not preserved and staircase effect is introduced.
Most filters, that belong to the spatial domain typology, are derived through spatial

proximity, while the neighborhood filters take gray level similarities into consideration to define a neighborhood patch. Yaroslavsky proposes a filter that considers both the spatial distance and the similarities in the gray level for the purpose of averaging [52, 53]. Tomasi and Monaco introduce the Bilateral Filter (BF) as an alternative, starting from the modified neighborhood filter, which deals with the distance from the reference pixel assigned a weight, rather than proceeding according to fixed neighborhood [16].
Another spatial filtering approach, based on the neighborhood filter, is called SUSAN (Smallest Univalue Segment Assimilating Nucleus) [54]. The aim is to provide greater edge retention through the use of the average of all pixels equidistant from the main pixel.
In the process of noise removal by the BF, gray level similarity and spatial proximity are considered. The noise filtering takes place starting from the areas belonging to the reference pixels, thus proceeding with the calculation of the average of the pixels that are spatially close and have similar intensity. This technique preserves the boundaries and edge shapes of the image. Starting from the results obtained from this filter, other variants are considered, such as the Weighted Bilateral filter, Robust Bilateral filter, Fast Bilateral filter, Multi-Resolutional Bilateral Filter [55].
Elad in [56] shows that bilateral filtering is traced back to Jacobi iteration of a weighted least squares minimization. Bilateral filtering turns out to be a brute force implementation, where the computational complexity increases exponentially as a function of the increasing proximity radius. Other studies on BF done in 2011 by Chaudhary et al. propose a safer and faster approach for BF due to the trigonometric range kernels rather than proceeding with the calculation of the Euclidean spatial distance [57]. In 2013 another approach, [58], proposes a more performing BF. Various other improved bilateral filtering variants are in [59]-[61].
Frabman and Durand argue that BF create gradient reversal artefacts in high dynamic range detail decomposition and compression of images [59, 62]. In [63] it is reported that BF does not work correctly when there are images that are affected by low levels of noise. Although bilateral filtering preserves edges, it tends to provide a poorly restored image [16] when the standard deviation of the noise exceeds the edge contrast.
Another variant of the BF is introduced by Jin et al. [64] in which a weighting function is used for the selection of the center pixel or vector median. Again for the BF, there is a model for the multi-resolution bilateral filter [55, 65]. In the work Peng et al. [66], an optimized approach for parameter selection using global information from two related images is provided [67]. Another filter, based on the ideal interpretation of the BF, is the guided filter [68]. Its implementation is faster than the conventional BF and its feature is to determine its edge-stopping func-

tion from a guide image. This filter has an automatic time implementation, which makes it independent in the choice of window radius $k$ as well as the possibility to freely choose the kernel size in real time.
Since the basic feature to implement local filters is the use of correlation between pixels, such filters tend not to work well when there are high noise levels, since the correlation between pixels is severely damaged.

### Non local filters

Buades et al. in [69], in addition to drawing up a ranking of the image denoising methods, introduce a filter that is based on the similarity between pixels, in a non-local manner or in the entire image, commonly known as Non-local mean (NLM) filter. The result of this work has established that the self-similarity amongst characteristics of an image in a non-local manner is the biggest potential basis in the field of image denoising. In the bilateral filtering method, the weighted average of the pixels in a given area is considered and the weights depend on both the geometric distances and the contextual similarity. In the NLM filter, however, the presence of similar characteristics or patterns in the image is used. The non-local filtering method is considered as a technique whose basic idea is to use all those pixels that satisfy the requirement of the Euclidean distance with respect to the selected reference pixel. The NLM algorithm represents a typical point-wise denoising approach that produces a noise-free pixel and the filter weights depend on the similarity between the areas of the reference pixels.
After the original version of the NLM filter proposed in [69], several refinement are born with the aim of speeding up the implementation of the filter and improving its results both in qualitative and quantitative terms. For instance, Zhang et al. assume that in a two-directional non-local variation model the reduction of noise from images can occur thanks to the idea that if similar portions are organized in the form of matrices, then rows and columns enhance the similarities [70]. With the aim of making NLM faster, [71] reports the contribution which involves the creation of a series of well-defined portions in which the average and the gradient are calculated to obtain a pre-selection of the contributing neighbourhoods. In 2012 Wang et al. present a non-local algorithm, called Gabor, that removes noise from textural images [72]. Goossens et al. in [73] provide an improved version of the NLM, the improved NLM (INLM), whose idea is to use the concept of symmetry in the weighting function and to calculate the Euclidean distance by symmetrical movement of recursive average filter (bi-square robust function). The iterative execution of the method leads to a better grouping of the areas, carried out during a pre-stage processing phase. The burdensome calculation due to the modified bi-square based robust weight calculation leads to a reduced loss of details. Although this filter allows the removal of extra noise, it tends to blur details

due to post-processing.
Xu et al. in [95] propose a method based on NLM, called NLM Patch-Grouping (NLMPG), to remove noise from images acquired in the remote sensing. This method is essentially based on the Block-wise NLM algorithm proposed by Coupe et al. [76] which operates on two fronts: it removes redundancy by selecting the most similar patches and also customizes constant filtering for center patches in accordance with the variance of image patches. The high performance achieved by this method, compared to some existing NLM-based methods, is remarkable.
Other variants, based on NLM, are presented in [80, 81]. However, although NLM is the first filter to use self-similarity across the entire pixel range, artifacts and performance tend to decrease when the image does not contain similar patches. The main idea for most denoising algorithms refers to the possibility of using the non-local characteristics of the image to preserve edges and details and, simultaneously, remove noise.
In the context of spatial domain image denoising, a lot of mathematical concepts are usually used. Among these topics, there is morphological filtering, an effective tool to level images and remove noise and extract features from the image.
Graham Treece considers a filter based on morphological filtering, which allows to remove the noise inside images. The bitonic filter is a non-local filter that is based on the concepts of bitonicity, i.e. it preserves the content of the signal that is locally bitonic (i.e. it only maintains a maximum or a minimum in a given range) and continuously removes noise pixels that do not fit in that range. This method is an adaptive denoising method. It preserves the edges by removing the noise without needing to know the amount of noise beforehand. Usage tests show promising results and better denoising performance compared to Gaussian and Median filters [96].
The main purpose of any denoising algorithm is to preserve details as much as possible while producing a good image from a visual representation. Most filters adopt the principle of suspending the noise reduction mechanism upon edge detection. Although spatial domain filters achieve high level performance, there is still an interest in preserving the original characteristics of the image, perhaps at the expense of the presence of noise. Although the noise is random, it has a higher frequency than the true signal which instead has a lower frequency and is repetitive in nature. Therefore, the higher frequency is removed in order to achieve noise reduction. However, the edges are not often repetitive and this characteristic determines their removal, thus generating corruption and blurring of the edges. Hence, the filters in spatial domain tend to remove high-frequency noise rather than high-frequency signal.
Furthermore, these filters are subject to gradient inversion and halo effects near the edges. Due to the size of the filter window and the convolution process, they

are slow from a performance point of view, and in some cases generate staircase and rare-patch effect causing high edge blurring. Hence, it is of common interest to create an approach that solves the problem of reducing noise from the image, as well as being able to preserve the edges, contours and in general the original information.

### Variational denoising methods

The methods, that belong to this category, minimize the energy function $E$, obtained from a noisy image $y$, in order to obtain the denoised image $\bar{x}$. The denoised image $\bar{x}$ is then obtained by minimizing $E$, that is:

$$\bar{x} \in arg \min_x E(x) \tag{1.2}$$

The aim is an estimate of a posterior probability. Using the Bayesian approach it is expressed as:

$$\bar{x} = arg \max_x logP(y|x) + logP(x) \tag{1.3}$$

where $P(y|x)$ is the likelihood function of $x$, whereas the term $P(x)$ is the prior image. If we consider the objective function in the context AWGN, the equation becomes:

$$\bar{x} = arg \min_x \frac{1}{2}||y - x||_2^2 + \lambda R(x) \tag{1.4}$$

where $||y - x||_2^2$ is the difference between the original and noisy images, whereas $\lambda$ and $R(x) = -logP(x)$ are the terms of regularization.

### Total variation regularization

The best known method in this category, and widely considered for a long time, is the Tikhonov regularization [17, 18], whose peculiarity is to minimize $R(x)$ with the $L^2$ norm, obtaining an over-smooths of the image details [19, 20]. To reduce the occurrence of this inconvenience as much as possible, diffusion-based methods [21, 22] are used in order to preserve the details of the image, although the edges are still blurred [23, 24].
Another method that is worth mentioning is the TV-based regularization [25], whose characteristic is a statistical factor which predicts that there are locally smooth areas in the images and that the pixel intensities vary gradually. The latter method is highly considered in image denoising as it calculates the optimal

solution, and also manages to keep the edges of the image sharp. But despite this, it also has disadvantages, which are summarized in the following points: textures run the risk of being over-smoothed, flat areas are replaced by approximated portions which lead to a stairway effect, the image itself may be lacking in intensity values that determine the contrast [26]-[29].
With the aim of improving the performance of the TV-based model, modifications are introduced for the partial differential equations [30]-[33]. To cite an example, consider Beck et al. [33] who consider a fast gradient-based method for constrained TV, in order to satisfy other types of non-smooth regularizers. Although it takes into account only the local characteristics of the image, it perfects the PSNR values.

### Non-local regularization

Although local denoising techniques have a low time complexity, these techniques show limitations in their performance when the noise level is high. This happens because the relationships between adjacent pixels are strongly compromised by the presence of intense noise. Recently, some approaches implement non-local self-similarity (NSS) [74]. This is because the images have similar large areas in different parts. Innovative work using NLM [75] adopt a weighted filtering of the NSS before proceeding with denoising process in the image, representing the most significant improvement in the context of noise reduction. The fundamental concept consists in building a pointwise estimate of the image, where each pixel is obtained as a weighted average of pixels belonging to regions similar to the one centered on the estimated pixel. For a given pixel $x_i$ in image $x$, NLM($x_i$) denotes the NLM-filtered value. Let $x_i$ and $x_j$ be image patches centered, respectively, at $x_i$ and $x_j$. We denote by $w_{i,j}$ the weight of $x_j$ with respect to $x_i$, calculated by:

$$w_{i,j} = \frac{1}{c_i} \exp\left(-\frac{||x_i - x_j||_2^2}{h}\right), \tag{1.5}$$

where $c_i$ represents a normalization coefficient and $h$ is a filter parameter. Unlike local denoising techniques, NLM take full advantage of the information in the images, which can be resistant to noise problem. For this reason, several improved versions are born. Some approaches focus on optimizing the algorithm [71, 73] [76]-[79], while others focus on increasing the performances of the algorithm [80]-[82].
In view of the initial phase of the NLM method [75] (the evaluation of similarity between pixels), regularization methods are introduced [83]. According to Eq. (1.4), the NSS prior is defined as [84]:

$$\mathrm{R_{NSS}}(x) = \sum_{x_i \in x} ||x_i - \mathrm{NLM}(x_i)||_2^2 = \sum_{x_i \in x} ||x_i - w_i^T k_i||_2^2 \,, \tag{1.6}$$

where $k_i$ and $w_i$ denote column vectors; the first contains the central pixels around $x_i$, while the second contains all the relative weights $w_{i,j}$.
Currently, most research on image denoising refer to non-local methods [85]-[90]. For example, in references [74, 91] there are extensions of non-local methods to TV regularization. Considering the advantages of TV and NLM methods, adaptive NLM regularization (R-NL) [91] is proposed to combine NLM with TV regularization. The results prove that combining these two methods allows success in noise reduction. However, such methods do not adequately preserve structural information, compromising the visual quality of the image. Furthermore, further important developments and improvements of NSS methods are based on learning the probability of image patches [92] and using the low-rank property through weighted nuclear norm minimization (WNNM) [93, 94].

**Sparse representation**

Sparse representation implies that each image fragment is described as a linear combination of various fragments from an extremely large dictionary [97, 98]. Techniques based on sparse representation treat an image using an extremely large dictionary $D$, with $L_1$-norm sparsity regularization on the coding vector, i.e.

$$\min_{\alpha} ||\alpha||_1 \; s.t. x = D\alpha \,,$$

and this leads to the following general model:

$$\hat{\alpha} = \arg \min_{\alpha} ||y - D\alpha||_2^2 + \lambda ||\alpha||_1 \,, \tag{1.7}$$

where $\alpha$ represents a matrix containing vectors of sparse coefficients. The equation (1.7) converts the estimate of $x$ in the equation (1.4) to $\alpha$.
In the sparse representation model, the dictionary learning method is obtained from a dataset, as well as derived from the same image using the $K$-singular value decomposition (K-SVD) algorithm [99, 100]. The basic principle behind the K-SVD denoising process is to train the dictionary $D$ by starting from a noisy image $y$ and solving the underlying joint optimization problem:

$$\arg \min_{x,D,\alpha} \lambda ||y - x||_2^2 + \sum_i ||R_i x - D\alpha_i||_2^2 + \sum_i \mu_i ||\alpha_i||_1 \,, \tag{1.8}$$

where $R_i$ represents the matrix extracting patch $x_i$ from image $x$ at position $i$.

The strength of the dictionaries describe the structures of the images [101], thus allowing a better representation in the context of sparse representation models compared to what is obtained from the use of designed dictionaries. In this regard it is worth mentioning the K-SVD dictionary [99], which reaches up to 1-2 dB more for bit rates lower than 1.5 bits per pixel (considered in the context in which the sparsity model applies) compared to all the others dictionaries. The methods of this category are all local, as they ignore the correlation between the non-local information in the image. If the presence of noise is high, the local information becomes seriously compromised and the denoising result is not eloquent.
The sparsity from self-similarity properties of natural images is widely used in the field of image denoising [102]-[104] and also in the previous NSS [74]. A representative example of this model is the non-local centralized sparse representation (NCSR) [104], namely:

$$\alpha_y \;=\; \arg\,\min_{\alpha} \,||y - D\alpha||_2^2 + \lambda \sum_{i=1}^{N} ||\alpha_i - \beta_I||_1 \,, \tag{1.9}$$

where $\beta_i$ represents a good estimate of $\alpha$. Therefore, for each area of the image $x_i$, the value of $\beta_i$ is calculated as a weighted average of $\alpha_{i,q}$ :

$$\beta_i \;=\; \sum_{q \in S_i} w_{i,q}\, \alpha_{i,q} \,, \tag{1.10}$$

where

$$w_{i,q} \;=\; \frac{1}{c_i}\, \exp\left( -\frac{||\hat{x}_i - \hat{x}_{i,q}||_2^2}{h} \right) .$$

Notice that $\hat{x}_i$ is the estimation of $x_i$ and $\hat{x}_{i,q}$ are the non-local similar patches to $\hat{x}_i$ in a search window $S_i$.
The NCSR model integrates NSS into the context of sparse representation and represents one of the currently widely discussed methods for image denoising. NCSR excels at effectively reconstructing both uniform and textured areas [104]. Although the results obtained from the fusion of the previous methodologies are encouraging, the iterative process of dictionary learning and the non-local estimation of sparse coefficients add to the computational complexity of this algorithm, thus significantly limiting its versatility in various contexts.

### Low-rank minimization

Unlike the sparse representation model, the models that belong to this category, have a low rank and represent similar areas by treating them in matrix form. Each column of this matrix is equivalent to a stretched patch vector. Since the matrix

has a low rank, this characteristic allows the noise in an image to be drastically reduced [105, 106].
The use of low-rank approaches in the reconstruction of data affected by noise is divided into two main categories such as: methods based on low rank matrix factorization [107]-[115] and those based on nuclear norm minimization (NNM) [93, 94, 116, 117].
The methods that belong to the first category generate a data matrix starting from the product of two fixed low-rank matrices. An application of such a technique is described in [107, 108], where it is applied in video denoising and the application of such denoising algorithm on images allows good results. Then, other variants are proposed, such as: a hybrid noise removal algorithm based on the recovery of low-rank matrices [110]; a low-rank method based on singular value decomposition (SVD) to model the sparse representation of non-locally portions of similar images, see Dong et al. [111]. A common feature of these methods is due to the constraint of having the rank as an input parameter, and this influences the performance of the result because it often generates loss of details or, on the contrary, maintains noise.
The low-rank minimization is a non-convex non-deterministic polynomial (NP) hard problem [101]. In order to avoid this problem, other methods consider the approximation of the lowest rank on a further observed matrix. Gu et al. [93, 94] propose a WNNM model, which adaptively removes weights to singular values of different sizes and denoise them using a soft threshold method. As described in [93], WNNM achieves good performance in denoising and is more performant than other techniques that are based on NNM. The low-rank theory is still widely used in different contexts, such as in artificial intelligence, image processing, pattern recognition, computer vision and so on [101]. Despite the good results recognized for this technique compared to previous denoising methods, and in particular the WNNM method, it involves a high computational cost.

### 1.2.2 Transform techniques in image denoising

Over time, image denoising techniques have grown from previous spatial domain methods to current transform domain methods. These techniques are based on the Fourier Transform (FT), but several other approaches exist such as, for example, the discrete cosine transform (DCT), wavelet domain methods [118]-[120], block-matching and 3D filtering (BM3D) [90]. A common feature of these methods is that the characteristics of image information and noise are different in the transformation domain.
In particular, techniques, based on the FT and on the DCT, are widely used in order to obtain noise reduction and lossless image compression. Restoring images by DCT is easier to use, but the reconstructed images contain artefacts and the

characteristics of the edges and details of the images are not preserved. The reason why wavelet domain-based methods are more popular than FT-based methods is that the former provide localization in both space and time, while FT is localized only in frequency. In the literature, there is a wide amount of contributions that show performances of using the wavelet transform compared to FT and DCT, both in terms of efficient image restoration and lossless compression [121].
In 1989, the use of the Mallat wavelet transform in the theory of multi-resolution signal decomposition introduced a revolution in the field of image processing and computer vision [122].
DWT (Discrete Wavelet Transform) is a mathematical tool that is obtained by discretization of continuous wavelet transform. Its main property [123, 124], foresee that most of the information in the image is encoded in a few high-value coefficients. DWT works by creating image approximation levels and for this reason it uses low-pass filters to generate coarse images and it uses banks of high-pass filters to obtain more detailed images. As the image changes to the next scale, each level of approximation is further broken down.
Wavelet-based denoising methods divide the image content into multiple subbands, corresponding to different resolutions and scales. Thus, low-frequency image information (level of approximation) is represented by the larger frequency coefficients, while noise and details exist in the high-frequency subbands. Acting on the threshold value of the smallest coefficients determines the possibility of removing the noise. By inversely transforming the coefficients in the spatial domain, the restored image is obtained.
The basic principle of noise removal is to act on the smaller wave coefficients in the high frequency band, and not to act on the high amplitude coefficients in the lower frequency band.

### Transform domain filtering method

The methods, that belong to this category, unlike spatial domain filtering methods, transform the noisy image into another domain and subsequently apply a denoising procedure on the transformed image based on the different characteristics of the image and on the noise. In this scenario, the details or edges of the image are expressed by the larger coefficients which denote the high frequency parts in the image, while the noise is associated to the smaller coefficients. Within this category, two further classes are identified according to the chosen basic transformation functions, as well as to the data, that can be of adaptative or non-adaptative type [125].

### Non-data adaptive transform

The methods, that belong to this category, are divided into two domains, namely the spatial frequency domain and the wavelet domain.
The former resort to the use of low-pass filtering, which in the frequency domain allows the passage of all lower frequencies and attenuates all higher frequencies with respect to a cut-off frequency [10, 12]. The low-pass filter is obtained, for example, by applying the FT and this allows the image information to spread mainly in the low frequency domain, while the noise spreads in the high frequency domain. Then it is possible to proceed with noise removal by selecting specific features of the transformation domain and transforming them back into the image domain [126]. The execution of these methods takes a long time and depends on the cut-off frequency and on the filter function behavior.
In [127]-[132] it is shown how wavelets can remove noise regardless of its frequency content, while maintaining image characteristics. Similarly as it happens for filtering techniques in the spatial domain, it is possible to apply a further subdivision based on the following criterion: linear and non-linear methods. Considering the good characteristics of the wavelet transform, such as sparseness and multi-scale, this determines a strong interest making this research area still active in the image denoising sector [133]. The wavelet transformation is highly dependent on the selection of wavelet base parameters. If the choice is inappropriate, the result does not allow a suitable representation in the wavelet domain, thus generating a poor denoising effect. Therefore, this method turns out to be non-adaptive.

### BM3D

The acronym BM3D stands for "Block Matching 3-D collaborative filtering"and the filter developed by Dabov et al falls into this category. This filter is particularly effective in the 3D transformation domain, and is designed to combine the sliding window process with block matching together. It has a multipoint approach and consists of three phases: in the first phase, the image with noise is processed smoothly, and similar block images are grouped together. The calculation of the similarity between blocks is done by the minimum Euclidean distance. The resulting blocks form a 3D matrix of redundant blocks. Subsequently, there is the second phase, that foresees the attenuation of the noise, performed by applying a rigid threshold or a Weiner filter. Clustering provides extremely reliable statistical data and Weiner filtering on 3D arrays is quite effective. As a result, following the local estimation of the matched blocks, constructed using the inverse 3D transformation, a meaningful improvement is obtained in terms of noise reduction and efficient detail preservation.
The BM3D approach considers the image contamination, attributable to AWGN

[90]. In particular BM3D drastically reduces its optimal performance at high noise levels. This happens when there is a standard deviation above 40, and such an effect implies that the correlation between blocks is strongly disturbed by noisy pixels. As an alternative to improve performances to the previous standard deviation, the wavelet is replaced with the DCT. This is described in [134], as it is possible to establish an improvement in performances by acting on an appropriate adjustment of some numerical parameters.

## 1.3 Other possible denoising methods

The variational denoising approaches, previously presented, are model-based optimization methods, as they lead to optimal results in the noise-free image reconstruction process. However, they usually require a large amount of processing time.
Other possible methods are described as follows. Convolutional Neural Network (CNN)-based denoised methods focus on the effort to learn a mapping function starting from a loss function on a training dataset characterized by pairs of images both with and without the presence of noise [135, 136].
In recent years, CNN-based studies and methods have aroused interest. They have been developed rapidly [137, 138]. The application of CNNs in denoising images dates back to the first decade of this century [139], and this network is composed of five layers. Recently, several noise reduction techniques based on this type of networks have been presented [135], [140]-[144].

Chen et al. [135] propose a deep feed-forward network, known as trainable non-linear reaction diffusion (TNRD), which shows a good performance in removing noise from images. In fact, the methods, that belong to this category, have numerous advantages including: a better interpretability, although this leads to an increase of processing costs; efficiency, to due the lower number of cycles.

### Deep learning-based denoising methods

The state-of-the-art DL denoising methods is traced back exclusively to CNNs and the noise removal methods associated with DL are described by the following formulation:

$$\min_{\Theta} loss(\hat{x}, x), s.t. \hat{x} = F(y, \sigma; \Theta)\,, \tag{1.11}$$

where $F(\cdot)$ indicates the CNN, $\Theta$ is the CNN parameter and $loss(\cdot)$ represents the loss function whose purpose is to estimate the distance between the starting image $x$ and the one subjected to the $\hat{x}$ noise removal procedure. Deep learning-based

denoising methods have attracted interest due to their exceptional denoising ability.
The concept of residual learning and batch standardization is introduced by Zhang et al. [142] in the context of removing noise from images, and also presents feed-forward denoising CNNs (DnCNNs). DnCNNs accomplish the goal of learning the function $\hat{x} = F(y; \Theta_\sigma)$, which generates a correspondence mapping between $y$ and $\hat{x}$. The values, represented from the parameters $\Theta_\sigma$, are trained for noisy images with respect to a fixed $\sigma$ variance value. DnCNNs have two main characteristics that make them so interesting. The first is the capacity of applying a residual learning formulation to learn a mapping function; the second is to refer to batch normalization in order to obtain a performance increment in the training procedure together with denoising results. The advantages, due to either residual learning or batch normalization, allow to improve the overall performances of the denoising system. Although a DnCNN manages compression and interpolation errors, the method is suitable only for certain $\sigma$ variances of noise.
The fast and flexible denoising convolutional neural network (FFDNet) [143] has the characteristic of making an adaptive trade-off between noise suppression and texture protection, when the noise level $\sigma$ is unknown. The FFDNet is expressed as $\hat{x} = F(y, M; \Theta)$, where $M$ represents a noise level map. While for FFDNet $M$ denotes an input parameter, for the parameter set $\Theta$ it is fixed. Furthermore, another feature of FFDNet is that it acts on down-sampled sub-images, thus contributing to improve the training and testing phase. In general, FFDNet is quite flexible with respect to different noises.
In conclusion, although this method is efficient and has a short execution time, the amount of time for the learning process is high and complex. CNN-based denoising techniques have led to improved learning by a hierarchical network.

### The state-of-the-art deep learning denoising

In the field of noise removal from magnetic resonance images, Manjón et al. in [184] in 2018 propose a technique that combines DL with classical noise reduction techniques. This technique consists of two phases. The first phase is essentially a patch-based CNN. The second phase uses a rotationally invariant non-local means filter. This technique achieves important goals compared to previous methods. During 2018 another contribution comes from Gondara et al., who in [185] show a new method to multiple imputation for handling missing data, a very sensitive problem which affects various fields. Their method consists of overcomplete deep denoising autoencoders, able of handling different types of data, patterns of missingness, proportions of missingness. The performed tests show that this method achieves better results than current methods in variable conditions, and it also improves end-of-the-line analytics. During 2019, Tassano et al. [186] propose a video

denoising algorithm that outperforms other patch-based methods. It is based on a CNN, which aims to be fast and efficient as it requires significantly lower execution times and low memory consumption, managing different noise levels with a single network model. Thanks to these characteristics, it is a practical solution for video denoising applications. The experimental tests confirm the effectiveness of this method as much as other methods, both in terms of visual quality and objective metrics. In 2019, Davy et al. [187] present a new CNN-based video denoising technique, which incorporates non-local self-similarity into the network via a non-trainable layer. This layer aims to find similar areas to the 3D spatio-temporal search region and gathers their central values into a feature vector assigned to each pixel. The CNN network is thus trained on the basis of this information so that it can be able to predict a clean image, thus obtaining excellent results. However, this technique appears to be the first application that successfully uses CNNs in the removal of video noise, thus surpassing previous methods based on non-local patches. In 2019, Liu et al. [188] propose a Genetic Algorithm-based network evolution approach to enable automatic optimization of network structures for medical image denoising. This technique reduces the evolutionary process by using experience-based greedy exploration strategy and transfer learning. This allows the birth of EvoNets, which goes beyond the previous methods in removing noise, even at different noise levels, from computed tomography perfusion (CTP) images.

## 1.4 Metrics of denoising performance

A common feature of the presented algorithms is the ability to remove the noise in the image and, at the same time, to preserve the information in the image itself as much as possible. To establish the effectiveness and computational efficiency of the different algorithm, a series of metrics are in Table 1.1: PSNR (Peak Signal-to-Noise Ratio), MSE (Mean Square Error), SSIM (structural similarity), VIF (Visual Image Fidelity), Entropy, AD (Average difference), MD (Maximum Difference), Normalized Absolute Error (NAE) and Normalized Correlation [145], [146]-[158].

| **Metric** | **Mathematical formula** | **Meaning** |
|---|---|---|
| MSE | $\frac{\sum M, N[I_1(m,n) - I_1(m,n)]^2}{M \times N}$ | Lower MSE depicts better image restoration. |

| **Metric** | **Mathematical formula** | **Meaning** |
|---|---|---|
| PSNR | $10 \log_{10} \left( \frac{R^2}{MSE} \right), \ R = 255$ | Higher PSNR means better quality of the denoised image; it represents the most used metric for image quality. |
| SSIM (x,y) | $\frac{(2\mu_x\mu_y + C_1)(2\sigma_{xy} + C_2)}{(\mu_x^2 + \mu_y^2 + C_1)(\sigma_x^2 + \sigma_y^2 + C_2)}$ <br> $C_1$ and $C_2$ are constants, $\mu_x$ and $\mu_y$ are the mean intensities, $\sigma$ is the standard deviation. | Metric correlated to human perception; high SSIM indicates more restoration of original information. |
| VIF | $\frac{\sum_{k \in subband\, s} I\left(D^{m,k}; T^{m,k}\right) s^{m,k}}{\sum_{k \in subband\, s} I\left(D^{m,k}; R^{m,k}\right) s^{m,k}}$ <br> where $D^{m,k}$ represents $m$ elements of the random field that describes the coefficients from subband $k$, $T^{m,k}$ and $R^{m,k}$ depicts the visual signal at the output of the HVS model for reference and test images. | Information fidelity criterion; it quantifies the Shannon information, which is shared between the distorted and the reference image, the fidelity aspect is correlated to the visual quality. |
| Entropy (EN) | $SE = \sum_i A_i^2 \log\left(A_i^2\right);$ <br> $EN = SE(A) - SE(B),$ <br> where $SE$ stands for Shannon entropy. | $EN$ is a statistical computation of randomness which conveys the amount of texture information. |
| AD | $\frac{\sum_{x=1}^{M} \sum_{y=1}^{N} (A(x,y) - B(x,y))}{M \times N}$ | It gives the average difference between the clean and the denoised image. |

| Metric | Mathematical formula | Meaning |
|---|---|---|
| MD | $MAX\|A(x,y) - B(x,y)\|$ | A lower value of MD means a better image quality. |
| NAE | $\frac{\sum_{x=1}^{M}\sum_{y=1}^{N}(A(x,y) - B(x,y))}{\sum_{x=1}^{M}\sum_{y=1}^{N}A(x,y)}$ | It gives the normalized rate of error; a lower NAE gives better denoised images. |
| NCC | $\frac{\sum_{x=1}^{M}\sum_{y=1}^{N}(A(x,y) \times B(x,y))}{\sum_{x=1}^{M}\sum_{y=1}^{N}A(x,y)^2}$ | It depicts the amount of correlation between the clean and the denoised image. |
| Assumption: $A$ and $B$ represent the clean and denoised images, respectively, and $M \times N$ is the size of the image. | | |

Table 1.1: Quantitative performance metrics.

The main function of the metrics is not to achieve the improvement of PSNR or any other metric. The main goal of image denoising is to generate noise-free images, preserving high visual quality so as to satisfy the Human Visual System (HVS). Studies in the literature show that the perfection of the human eye does not allow to perceive slight differences in the orientations, scales and structure of the images. Despite this, the HVS remains very sensitive in the recognition of sharp contours, deformed faces and artefacts inside homogeneous regions. These considerations among the different methods of reducing noise from images are important as visual analysis is always left to the end user, who is generally man and consequently visual analysis remains the most used measurement metric in the discussion of any type of noise reduction technique from images.
Presenting all the methods to remove noise from images is almost impossible. For this reason, some of these methods are examined and some are subsequently cited as a reference for the reader.
The methods are: SBF [16], RBF [159], WBF [159], NLM [69], bitonic filter [96], Diffusion filter assortments (DF(A-B)) [158], Gaussian filter [8], Median Filter [8, 14], Gaussian Field of Experts (GFOE) [160], Total variation minimisation [161], non-local version of general relative total variation (NLGRTV) [162]. The different transform domain methods include Vi-hard [163], Vi-soft

[164], SURELET [165], NSST [63, 166]. They are part of the [167] category of Markov Random Fields (MRF) statistical methods.
As for dictionary learning methods and different sparse representations, there are Nonlocally Centralized Sparse Representation (NCSR) [104], Locally Adaptive Kernel Regression (LARK) [168], and deep neural networks (NN) [169] in experimental analysis. Other representative methods also belong to this category, such as LPGPCA [103], BM3D-SH3D [170], BM3D [90], BM3D-SAPCA [171], PGPCA (Patch based Global PCA), PLPCA (Patch based local PCA), PHPCA (Patch Based Hierarchical PCA) [172].
In the category of methods based on the hybrid domain, there are: GBFMT [173] and NLFMT [174].

## 1.5 Applications of image denoising

The ever-increasing demand for information leads to the need for high-resolution images. Sometimes, however, images are affected by the presence of information that disturbs the image itself, a phenomenon known as noise, the reduction of which from the image is the subject of interest and in-depth studies by researchers. In fact, image noise reduction not only generates visually pleasing images but it is important for the subsequent analysis of the image itself. This denoising process involves various areas of interest, starting from medical imaging, biometrics, remote sensing, HVS, military surveillance and infrared image denoising. The principal areas of application for the denoising techniques are as follows:

- Medical image denoising.
- Underwater image denoising.
- Remote sensing-image denoising.
- SAR image denoising.
- Infrared image denoising.

### Medical image denoising

In this context, the removal of noise from images is applied to those images obtained from the outcome of magnetic resonance imaging (MRI), the objective of which is to highlight the soft tissues of various organs of the body. The disturbances that may appear in such images can derive from various noise factors such as interference due to the magnetic fields generated by the acquisition device itself, from electromechanical components and in general from surrounding interference.

Yang et al. in [175] propose an alternative to the removal of multi-scale MRI noise by using wavelets, in which the noise is considered as Gaussian Noise. The noise estimation deals with the Rician noise distribution and the result of the final image, free of noise, is obtained by the inverse Radon transform. The evaluation tests are done by a set of images from simulations and MR of the human brain.
Another technique, used to analyze the brain, is tomography, which is a radiodiagnostic technique that provides a series of layered images of the different tissues of the body. It is subject to image degradation due to the intrinsic noise of interference and disturbances deriving from the electromechanical components inside the devices. In this scenario, numerous methods are useful to erase noise from images, presented in [5]. Kumar et al. in [176] propose an approach able of eliminating noise from high frequency coefficients in order to obtain the preservation of edges, corners, textures and sharp edges by the Tetrolet transform. This technique shows good performances in terms of MSE and PSNR, as well as in the noise removal and in preserving general structural integrity.

### Underwater image denoising

Laser image acquisition technologies are often considered within the marine environment, in particular in underwater contexts where the presence of the disturbance is mainly due to the attenuation and propagation of laser waves in the water, thus resulting in a consequent poor quality of the captured image. Studies by Jian et al. in [177] analyze the use of denoising algorithms in underwater images by the software MATLAB.

### Remote sensing-image denoising

The images coming from satellite observations are generally affected by noise deriving mainly from the possible presence of atmospheric phenomena. Moreover, there is also the noise attributable to the acquisition itself and the subsequent transmission of the information. The main aim of noise removal is to make images more suitable for subsequent analysis, thus identifying the high frequency noisy components. Thanks to the intuition of directional correlation in spatial and transform domain, it is possible to reduce noise from images. Sharmila et al. in [178] propose a hybrid directional lifting scheme for denoising of satellite images. This method uses both pixel classification and orientation estimation.

### SAR image denoising

Images coming from radar acquisition are often affected by disturbances resulting from interference, thus determining one of the most relevant problems of research in the remote sensing sector. Liu et al. in [179] propose a new technique to

remove noise from images based on sparse representation in shearlet domain and continuous cycle spinning. The procedure consists of two phases. In the first one, the noisy image is decomposed using the shearlet transform. Then an optimal denoising model is built using cycle spinning theory in the sparse representational domain. Tests performed using this technique reveal improvements both in terms of visual results as well as PSNR.

#### Infrared image denoising

The human eye can only see a portion of the electromagnetic wavelength spectrum. Recent technologies allow us to see beyond the human visible, making infrared (IR) capable of penetrating various materials. Infrared radiation is used in night vision devices, when there is not enough visible light and therefore used as night vision technology also for military purposes. Infrared sensors convert the incoming radiation into an image: this can be monochromatic (for example, hotter objects will appear lighter), or a system of false colors can be used to represent different temperatures.
Infrared image acquisition technology is used to capture the thermal radiation that each object on Earth emits in a unique and different way from any other type of object. But even this family of images is not free from Poisson noise, mainly caused by low light conditions and atmospheric disturbances. Shen et al. in [180] propose to perform the Anscombe transform in order to generalize the Poisson distribution into Gaussian distribution and to denoise the infrared images. This method consists of total variation regularization based improvisation in the wavelet domain in order to remove heavy Poisson noise from low-light infrared images.

## 1.6 Variational models in image processing

Over the past twenty years, image processing has attracted the attention of many scholars. It turns out to be a valid tool to reconstruct the geometry, topology, models and dynamics of the three-dimensional (3D) world from that of two-dimensional (2D) images. Image processing finds wide sectors of use ranging from astronomy to aerospace exploration, to the medical and molecular fields, to computer graphics, to artificial vision, to telecommunications, to autonomous driving systems, to video surveillance systems, biometric identification through the recognition of fingerprints and facial identification useful for security purposes. More recent approaches suggest image processing techniques that are based on the variational PDE (partial differential equation) method.
When dealing with an image subjected to variational processing, it can be considered as a function whose sampling corresponds to the discrete matrix form. There-

fore it is possible to compare variational image processing with high-resolution image processing. This sector is born from works by Perona-Malik [21], Rudin-Osher-Fatemi (ROF) [25] and Mumfomrd-Shah [189], thus bringing the variational processing of images to a sudden development.
To manage and process images efficiently, images need to be defined from a mathematical point of view and they have to be represented. In the case of Random Fields Modeling, an image is modeled as the sampling of a random field. In statistical mechanics, the Ising spin approach can model binary images. The images are modeled by some Gibbs/Markovian random fields [181]. The statistical properties of fields are generally established through a filtering technique and learning theory. The random field modeling is the ideal approach to describe images of natural environments, such as trees and mountains. In the case of Wavelet Representation, the images come from acquisitions provided by a set of micro sensors. Over the last twenty years, it has been concluded that such acquisitions are well approximated by wavelets. This new technique to represent images and their multiscale structures [122] has attracted much interest. The two examples of applications, that have generated particular appreciation, are the JPEG2000 protocol for image coding and the successful compression of the FBI fingerprint database. In the case of Regularity Spaces, an image is considered in Sobolev space as this model works well for homogeneous regions but it is not efficient in managing edges because it tends to introduce noise. To overcome this problem, two well-known models are introduced. The first is called the "object-edge"model of Mumford and Shah [182], and the second is the BV image model of ROF [25]. The first model foresees that an image consists of patches of disjoint homogeneous objects and that it has regular boundaries (characterized by the one-dimensional Hausdorff measure). The second BV model, instead, assumes that an image has a limited total variation. Models based on image regularity may be applicable to images with low texture patterns and without rapidly oscillatory components.
In variational or "energy"based models, Euler-Lagrange equations are derived or the gradient descent method is used in order to identify local or global minima by non-linear PDEs. For some PDEs, the study uses the viscosity solution approach [183], while for many others further theoretical investigations remain open. Compared to other approaches, the variational PDE method has meaningful advantages both in terms of the theoretical aspect and in the calculation. It directly manages and processes visually important geometric features, such as gradients, curvatures and level sets. It is also able to simulate several visually processes, such as linear and nonlinear diffusions and the information transport mechanism. Finally, as for the numerical analysis and PDEs, there is also a high amount of works in literature, that are useful to construct numerical schemes.

# Chapter 2

# Variational PDE models in image processing

## 2.1 Problem statement

An image subjected to a variational processing process is depicted through a matrix representation. Thanks to the most recent studies and those conducted with resourcefulness in this context by Perona-Malik [21], ROF [25] and Mumfomrd-Shah [189], the topic of variational image processing has obtained wide consensus and approval.
To present the topic of variational denoising, it is advisable to consider the Euler-Lagrange (EL) equations, just as to be able to talk about variational image processing implies recalling the concepts of regulator based on TV and one based on the mean curvature.
Define an image in domain $\Omega$ by $z = z(x, y)$ in which the presence of the noise is represented by the zero mean Gaussian noise $\eta$, such that

$$z = u + \eta\,.$$

The denoising function for image restoration is defined as $u = u(x, y)$ (see [25]). Restoring $u$ from $z$ is classified as an inverse problem, in which Tikhonov regularization can be applied in order to guarantee its uniqueness:

$$\min_u J(u) = \frac{1}{2}\int_\Omega (u - z)^2 \, dx\, dy + \alpha\mathcal{R}(u) \tag{2.1}$$

where $\alpha > 0$ and $\mathcal{R}(u)$ represent the regulators of $u$.

In the derivation of the EL equation for the ROF model [25], taking into account that $|\nabla u| = \sqrt{u_x^2 + u_y^2}$, the following semi-norm TV was proposed

$$\min_u J(u) = \frac{1}{2}\int_\Omega (u-z)^2 \, dx\, dy + \alpha \int_\Omega |\nabla u| \, dx\, dy\,, \tag{2.2}$$

in which the EL partial differential equation (PDE) for the ROF model is the following TV equation

$$-\alpha \nabla \cdot \frac{\nabla u}{|\nabla u|} + (u-z) = 0\,,$$

which is discussed in [25].
In the derivation of the EL equation for the curvature model, the ROF model above (2.2) identifies and protects edges in $u$, but when the image $u$ as a whole complex has a constant behavior at times, for uniform images you get a restored quality that is not good. However, many alternatives have been proposed, one of which is the mean curvature model of [190, 191] defined as follows

$$\min_u F(u) = \frac{\alpha}{2}\int_\Omega k(u)^2 \, d\,\Omega + \frac{1}{2}\int_\Omega (u-z)^2 \, d\,\Omega \tag{2.3}$$

and has the characteristic of being an effective method, as reported in [192] by Brito and Chen, in which the average curvature is expressed as $k(u) = \nabla \cdot \nabla u \,/\, |\nabla u|\,.$
Assuming the following values for the following parameters $k = 0$, $\nabla u \cdot n = 0$, we have

$$\alpha \nabla \cdot \frac{\nabla k}{|\nabla u|} - \nabla \cdot \frac{\nabla k \cdot \nabla u}{|\nabla u|^3} \nabla u + (u-z) = 0\,.$$

This scenario arouses a lot of interest in the scientific community, which has produced a considerable quantity of papers published in this regard. Some of the most representative ones are described below.
Thus there is the paper by Bonettini, Landi, Loli Piccolomini and Zanni which frames the topic of image deblurring [193], which proposes a comparison to solve a specific problem of deblurring astronomical images corrupted by Poisson noise. The aim is to present a computational study on scaling techniques in gradient

projection-type (GP-type) methods. Specifically, the imaging problem is formulated as a minimization problem, where the study focuses on solving the deblurring problem from Poisson data involving the unconstrained minimization of the Kullback-Leibler (KL) divergence and the Tikhonov regularization, which is well suited for the reconstruction of the smooth, due to the presence of diffusive objects often encountered in image acquisition using satellite devices. The GP-type methods, that are considered, are formulated using a common iteration formula, where the scaling matrix and the step length parameter characterize the different algorithms. Within this formulation, both first-order and Newton-type methods are analyzed. Numerical experiments show that suitable scaling strategies can enable GP methods to rapidly approximate accurate reconstructions and thus are useful for designing effective image deblurring algorithms. In this context, a stopping criterion is proposed to avoid unnecessary computations while preserving the reconstruction accuracy.

Yan, in [194], achieves the aim of providing an overview of the different consolidated techniques for image reconstruction, and in particular performs a convergence analysis for Simultaneous Algebraic Reconstruction Technique (SART) methods. Several methods for the derivation of SART and the connections between SART and other methods are presented. Using these connections, the convergence of SART is demonstrated in several ways. Schemes are thus reported, and they can be traced back to the SART method, such as Landweber-type schemes, linearized Bregman iteration for the primal, gradient descent for the dual and expectation maximization. The main contribution is a convergence proof for Landweber iterations. Several numerical experiments for computed tomography reconstruction are provided to demonstrate the convergence results in practice.

In the field of image deblurring and denoising of multiplicative noise, Wang and Ng present [195] a fast and efficient minimization method for image restoration affected by multiplicative noise that makes them blurry. This type of problem has attracted a lot of attention in recent years. The proposed algorithm uses the logarithm to transform blurring and multiplicative noise problems into additive image degradation problems, then uses the $L_1$-norm to obtain a measure of the data-fitting term and of the total variation in order to measure the regularization term. To solve the constrained minimization problem, the Alternating Direction Method of Multipliers (ADMM) is used. The set of constraints is first approximated and subsequently replaced by a corresponding convex set in order to guarantee the convergence of the proposed method. Numerous numerical tests are presented in support, including also different types of blur kernels, to illustrate the excellent performance that the proposed algorithm offers, unlike other existing methods in terms of speed and PSNR.

As for image segmentation, Häuser and Steidl carried out a study inside paper

[196]. It is well known that segmentation is the basis of many image pre-processing processes, thus occupying an important role. In this regard, there are some works, in which convex relaxation methods for image multi-labelling have been proposed. Generally these models use the TV semi-norm as regularizing term, although it is well known that the TV function is not optimal for the segmentation of textured regions. The objective is to demonstrate that, for the best manage of segmentation of curved structures, it is sufficient to apply the Shearlet transform. Neither the Shearlet transform nor the Curvelet transform are used as a regularizer in a segmentation model. Through numerical examples, it is shown that the Shearlet-regularized model can improve segment curved textures compared to the TV-regularized one. This approach is promising for image segmentation.
In the image reconstruction sector, Barendt and Modersitzki refer to [197], in which the study conducted on Single Photon Emission Computed Tomography (SPECT) allows to reconstruct the density of a radioactive marker within a patient from projections, relating an integral equation the unknown density of the radioactive tracer with the observed signal (photon counting). The authors present an algorithm to estimate both the tracer density and the attenuation coefficient. Regarding tracer density estimation, the authors use an existing non-negatively constrained iterative method while, for as the attenuation coefficient, it is treated as a deformation of a "prototype" attenuation and use image registration to obtain the estimate. The most current reconstruction models are addressed, in order to be able to address the SPECT reconstruction process through a so-called attenuation prototype. A new variational model for SPECT reconstruction addressing the multimodal matching problem is also presented.
On the topic of image surface restoration, Brito-Loeza and Chen dedicate their study on [198], in which three recent models are described. In the context of the most suitable variational models for the processing of planar images, the TV model and the mean curvature model stand out. It is intuitive to understand that in order to solve the 3D data minimization formulation, a considerable amount of numerical calculations is required and how this measure can grow dramatically. Although there is an ever-increasing demand to get computationally fast and efficient algorithms, able of processing large quantities of high-resolution data, in this area there is still room to conduct in-depth studies. Recently Tasdizen, Whitaker, Burchard and Osher in [199] introduce a two-pass algorithm that allows obtaining fast solutions for the total curvature model. Through a process of generalization and appropriate modifications, the mean curvature model of Droske and Rumpf [200] and the Gaussian curvature model of Elsey and Esedoḡlu [201] are analyzed in order to obtain solutions similar to the aforementioned models. Finally, the results of the tests and numerical experiments are reported so as to show the good performance of the algorithms.

Bredies, Dong and Hintermüller present [202] the topic of image denoising with Total Generalized Variation (TGV) and, more precisely, the choice of parameters to adopt to address the problem of image restoration, which can be solved by finding the minimum of a cost function. This function is generally composed of the data fitting and a regularization term. In the context of the TV regularized model, authors have recently considered how to choose spatially adapted regularization parameter, rather than choosing a fixed parameter, in order to obtain better restoration results. It is well known that images, restored by the TV models, have the staircasing effect and the TGV model was proposed in order to reduce such effect. Furthermore, the case of how to select the spatially adapted regularization parameter when TGV was used as the regularization term is also addressed. Ultimately, the main contribution that the authors offer is to be able to extend the parameter selection method from the TV model to the TGV model.
In the field of image segmentation, the study by Zhu, Kang and Biros refer to [191], in which a new Geodesic-Active-Contour-based (GAC-based) variational model is proposed to segment the right and left ventricles and the epicardium in short-axis magnetic resonance (MR) images. This is the case of an application of real interest, which represents a practical challenge in image segmentation. It is a difficult task because the contrast of such data sets, in addition to not being of great quality, is also easily affected by noise, also because in the right ventricle, the myocardial wall is generally very thin and difficult to identify using the resolution of current scanners MR. Level sets are proposed to be used to identify both the endocardial wall and edge detection, and for the latter the detection functions have strict restrictions on the position of the initial edges. The aim of the author is to create a new edge detection function that loose these restrictions. Numerical examples are provided to illustrate the method and experimental results are presented to validate the effectiveness of the proposed model.
As for image denoising of combined additive and multiplicative noise, we have the work [203] by Chumchob, Chen and Brito-Loeza. They present an overview of some results for the progress made in the removal of additive or multiplicative noise, even if in the literature there are not often restoration models for the removal of both additive and multiplicative noise. Then, some new algorithms to remove the mixture of additive and multiplicative noise are covered. Taking into account the works previously proposed by Rudin, Osher and Fatemi [25], and that of Jin and Yang [204], a new model is born. It is a variational model for which special non-linear multigrid schemes are provided and details are given on how to implement this algorithm for the removal of additive or multiplicative noise from digital images. The results of experimental tests using both realistic and synthetic images are also considered.
Thanks to the sudden developments in hardware and software technologies involv-

ing the imaging sector, these have increasingly attracted the attention and broad consensus of many mathematicians and other researchers in the study of variational models in order to address emerging challenges over the last two decades. For this reason, efficient models are developed for the correct automatic recognition, identification and reconstruction of the characteristics of images affected by noise, so that they are used in the field of data analysis and in applications.

## 2.2 A variational model for restoration of satellite optical images using synthetic aperture radar

The images acquired through multispectral satellite systems have the characteristic of possessing a high resolution and this allows the images themselves to contain ever more defined details. Nowadays, thanks to the constant development of hardware and software technology, it is possible that such acquisitions also take place through the use of low-cost optical devices. However, these images are not free from disturbances, which can derive not only from the acquisition system itself but are often damaged also due to unfavorable weather conditions, such as rain, clouds, fog and dust. Furthermore, situations often occur in which the measurement of the degradation of the images acquired with optical systems is such that it is not possible to count even on the availability of a single brightness value within the regions subject to disturbance. The result of this fact is that it leads some subdomains of such images to become absolutely invisible. Although there are many approaches in the literature on the reconstruction of images affected by noise, such as in the case in which color information is not available everywhere (see for example [205]-[209]), the approaches methods for exact restoration of damaged optical images are no longer applicable in this case and it remains a challenging and open task. Radar images, unlike observations made with the aid of optical devices, do not depend on reflected sunlight and can be used at night even in unfavorable weather conditions. In the specific case, where the attention is focused on the vegetation, a radar system, instead of returning information on the biophysical processes of the plant, contain information on the structure and moisture content of the vegetation and the underlying soil. The union of the information obtained through SAR (Synthetic Aperture Radar) and optical images appear to be a valid aid in the classification of the [210] land cover and in the estimation of soil moisture, in order to remove the effects of the cover vegetable from the backscatter coefficient of the [211]-[213] radar. Also, due to the different nature of SAR images and optical images, there is a huge radiometric difference between optical and synthetic aperture of radar images. Each object in nature

is encoded with different wavelengths, and similarly different wavelengths encode different properties of objects. For the same object, therefore, there are significant differences in intensity between the SAR images and the optical satellite images. The consequence induces to think that it is to possible recover with a high level of precision those damaged regions within the optical images contaminated by the clouds starting from the corresponding intensity regions of the SAR images. Optical and SAR images of the same place, as in the case of more or less extensive agricultural areas and of various shapes, have a lot of characteristics in common (see, for example, [214]). Strongly inspired by this observation, a new variational model for the correct restoration of the damaged multispectral optical satellite images is proposed, through the use of the results obtained from SAR images of the same regions. Let $\Omega \subset \mathbb{R}^2$ be a bounded image domain with Lipschitz boundary $\partial\Omega$ and let $D \subset \Omega$ be a Borel set with non empty interior and sufficiently regular boundary and such that $|\Omega \setminus D| > 0$. Let $D$ the damage region of a given multi-band image $\vec{u}_0 = [u_{1,0}, u_{2,0}, \ldots, u_{M,0}]^t \in L^2(\Omega \setminus D; \mathbb{R}^M)$ where the optical image $\vec{u}_0$ is corrupted by clouds. As previously said, the interest is directed to the case in which there is no information on the original image $\vec{u}_0$ inside $D$. For simplicity, a SAR image $u_{SAR} : \Omega \to \mathbb{R}$ of the same region is given, and this image is well co-registered with $\vec{u}_0$ in $\Omega \setminus D$. The main objective is summarized in trying to solve the problem of to reconstructing the intensities $u_{i,0}(x)$, $i = 1, \ldots, M$, of the original multi-band image $\vec{u}_0$ through a variational model starting from the knowledge of SAR image on the subset $D$ (the damaged region) together with the exact information of $\vec{u}_0$ on $\Omega \setminus D$ (the undamaged region). Strongly motivated by recent studies in this area [215] (see also [216]-[220] for comparison), a new strategy is proposed to address the optical image restoration challenge contaminated by disturbance. It is possible to proceed with the fusion between the zone contaminated by noise of the optical image and the same corresponding area in the SAR images. The variational approach is inspired by the recent article [215], in which the authors consider the minimization of the following energy functional

$$u \mapsto \frac{1}{2} \| (-\Delta)^{\frac{s}{2}} u \|^2_{L^2(\Omega)} + \frac{\alpha}{2} \| (-\Delta)^{-\frac{\beta}{2}} (u - g) \|^2_{L^2(\Omega)}, \tag{2.4}$$

with $0 < s < 1$ and $\beta \in [0, 1]$, where $(-\Delta)^s$ denotes the fractional power of the Laplacian with zero Neumann boundary conditions. Then the first necessary and sufficient optimality condition determines the unique minimizer $u$ via

$$\begin{gathered} (-\Delta)^s u + \alpha (-\Delta)^{-\beta} (u - g) = 0 \quad \text{in } \Omega, \\ \partial_\nu u = 0 \quad \text{on } \partial\Omega, \end{gathered}$$

which can be reduced to an linear elliptic partial differential equation that can be efficiently solved using, for instance, the Fourier spectral method [221] or the

Stinga-Torrea extension [222]. However, from the reconstruction point of view, it is desirable that the regularity of the solution to (2.4) is high in places where $u$ is smooth or contains homogeneous features and that is low in places in $\Omega$ where edges or discontinuities are in $u$. It is interesting to consider (2.4), where $s : \Omega \to [0, 1]$ is not a constant. This entails that the choice of parameter $s$ has a direct influence on the global regularity of the solution to problem (2.4). However, the definition of the fractional Laplacian in terms of the Caffarelli–Silvestre [223] or the Stinga–Torrea [224] extension is well-known only for a constant $s \in (0, 1)$, whereas such a result remains open when $s(x) \in (0, 1)$ for $x \in \Omega$. Consequently, there is no obvious way on how to define the operator correctly $(-\Delta)^{s(x)}$ and it looks an open question. For further details refer to [215]. As opposed to the standard approach of restoring damaged color images where the starting point is either the knowledge of the gray level of the original color image $\vec{u}_0$ on a given open subset $D$ of $\Omega$ (the damaged region) together with the exact information of $\vec{u}_0$ on $\Omega \setminus D$ (the undamaged region) or the grey level information in the damage region $D \subset \Omega$ is modeled as a nonlinear distortion of the colors, the technique described deals with the case where there is no information about $\vec{u}_0$ inside $D$ but it is assumed instead that a SAR image is provided $u_{SAR} : \Omega \to \mathbb{R}$ of the same region. The illustrated technique has the aim of the reconstruction by the proposed variational model. Although the proposed minimization problems turn out to be well posed and possess good approximation properties, their practical implementation for satellite image restoration is not trivial and remains a complicated issue due to non-convexity and the corresponding strict optimality conditions. The aim of what is described here is to present "an approximation approach"which is based on the principle of relaxation of extreme problems and their variational convergence. It is proposed to proceed towards some relaxation of the original problem using a special iterative algorithm. Thus, it is shown that, at each step of the iteration procedure, a strictly convex optimization problem with a unique solution is obtained. It is established that the sequence of approximations thus defined turns out to be precompact in some Hausdorff topologies and that every convergent subsequence leads to a weak solution of the original problem. The experimental activities carried out in this study (see Section 2.2) confirm the effectiveness of the proposed method and have also highlighted that there are appreciable visual performances and a satisfactory quantitative precision in the field of agricultural images.

### Numerical Experiments

This section reports the results of the numerical experiments, in the form of images, relating to the proposed algorithm for the restoration of satellite multi-spectral optical images affected by disturbance due to the presence of clouds. A series of optical images and a radar image provided by two twin satellites, Sentinel-

2A and Sentinel-2B, were used as input data. Each optical image is corrupted by the presence of clouds with a different level of degradation (see Fig. 2.1, 2.3, 2.5, 2.7). The corresponding SAR image is shown in Fig. 2.9. The results of restoration after 5 iterations of the proposed algorithm are shown in Fig. 2.2,

Figure 2.1: Optical image from 2021/040.

Figure 2.2: Result of its restoration.

Figure 2.3: Optical image from 2021/032.

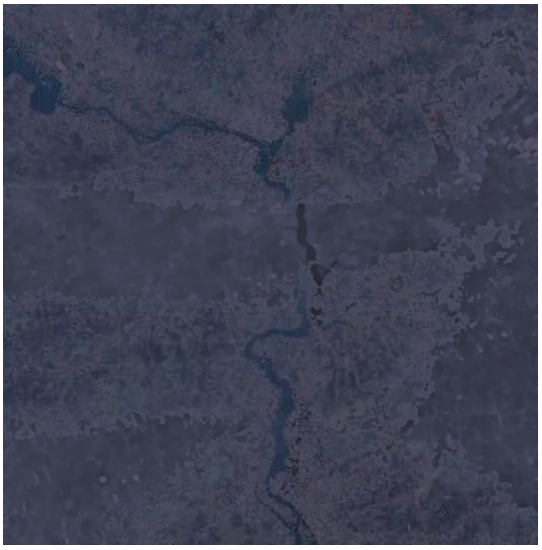

Figure 2.4: Result of its restoration.

Figure 2.5: Optical image from 2021/041.

Figure 2.6: Result of its restoration.

Figure 2.7: Optical image from 2021/0406.

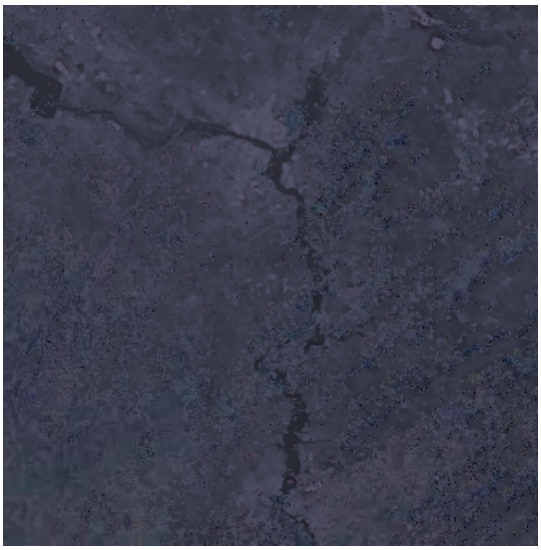

Figure 2.8: Result of its restoration.

2.4, 2.6, 2.8 for $\eta = 0.8$, $\mu = 10$, and $\lambda = 20$. As for the exponent $\alpha$, it is define by $\delta = a^2 \left[a^2 + \|G_\sigma\|^2_{C^1(\overline{\Omega-\Omega})} 255^2 |\Omega|^2\right]^{-1}$ and $a = 0.01$. As can be seen from the comparisons between the images affected by noise, due to the presence of clouds, and the corresponding restored images obtained as a result of the technique

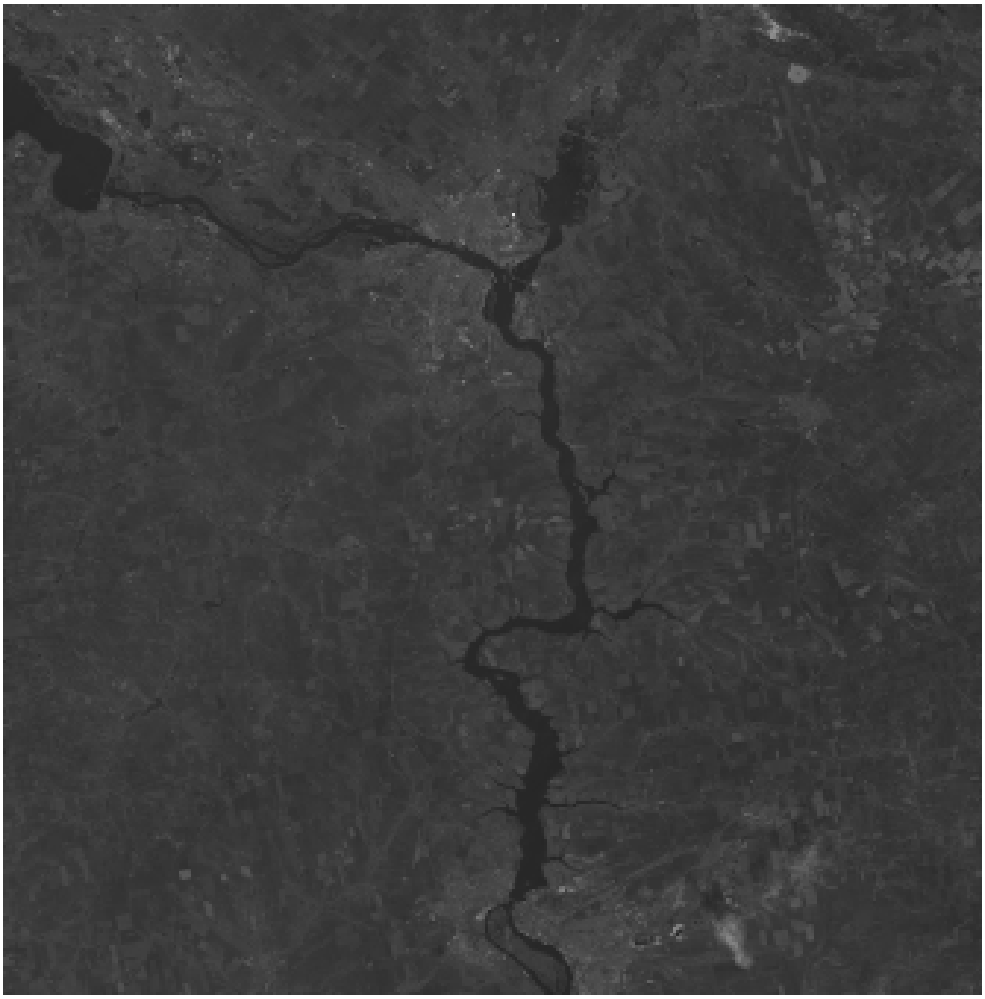

Figure 2.9: The SAR image of the same territory.

presented, it is possible to note that the texture of the latter appears to be well preserved. However, some details in the damaged areas are blurry.

## 2.3 A variational model for denoising and deblurring of non-smooth hyperspectral satellite images

Thanks to increasingly in-depth knowledge in the remote sensing sector, these have found wide application in many sectors, thus contributing, as in the case of the agricultural sector, to the possibility of being able to carry out constant

monitoring. This has led to systematic worldwide observations of the so-called optical vegetation indices. Some indices, including NDVI (Normalized Difference Vegetation Index) and IPVI (Infrared Percentage Vegetation Index) and others, are indicators that provide information and allow the state of health of vegetation and crops to be established. For example, thanks to timely monitoring, they are able to establish whether crops need water or nutrients. From a physical point of view, the sensors of the optical devices used in the remote sensing sector record the so-called electromagnetic fingerprint that each object on Earth emits in response to an electromagnetic radiation signal. The reflectance from each object occurs in different wavelengths and these values are then processed to create a separate image for each wavelength. In the images obtained from satellite, there are reflectance values stored for different wavelengths in different layers, also called spectral channels. Specifically, Santinel-2 satellites provide 13 spectral channels with a pixel size ranging from 10 to 60 meters. Therefore, a hyperspectral image defines in a completely simple way the number of wavelength channels of which it is composed. So you can have images with as little as one channel to at least three, corresponding to the three RGB channels, which are recorded by the sensor to create a composite satellite image. By carrying out monitoring with regular frequency in a pre-established period, it is possible to recover the complete time series in the different wavelengths, which allows to obtain information with respect to a vegetation index, useful to establish the state of the crops, in order to plan any interventions especially during those periods when conditions on agricultural land change dramatically (for example, during essential growth stages, the need to irrigate the soil, the ripening period and others). However, despite the fact that optical images have a high resolution and are easily acquired using low-cost devices, satellite images, that represent the real world, can often suffer from different types of noise, among which blurring and other artifacts mainly prevail atmospheric factors that influence the radiation recovered by the sensors in different spectral channels and in different ways. Due to this, such satellite images lose their effectiveness in managing the monitoring of cultivated agricultural fields, and their use can lead to erroneous results and conclusions. In a context like the one just described, the problem, that has been examined, can be briefly described as follows. There is a hyperspectral image $\vec{u}_0 = [u_{1,0}, u_{2,0}, \dots, u_{M,0}]^T \in L^1(\Omega; \mathbb{R}^M)$ which is affected by noise or blur and this makes the image itself devoid of important features. Here, $\Omega \subset \mathbb{R}^2$ is a bounded open domain with sufficiently smooth boundary $\partial\Omega$. Therefore, the challenge is to recover the original image $\vec{u} = [u_1, u_2, \dots, u_M]^T$. In fact, the hidden image portion occurs starting from the observed data $\vec{u}_0$. In mathematical terms, this means that, for each spectral channel $i = 1, \dots, M$, an inverse problem must be solved, expressed in the following form

$$T_i u_i + w = u_{i,0}\,,$$

where $T_i$ represents the linear blur operator that models the process by which the $i$-th spectral channel of $\vec{u}$ is passed before observation, and $w$ is the unknown disturbance which influences the measurements. Due to the presence of the noise and the fact that the blur operator $T_i$ is often ill-conditioned or even non-invertible, and that the value represented by $w$ expresses the unknown noise that affects the measurements, the recovery of starting from the measurements of $\vec{u}$, $\vec{u}_0$ turns out to be an ill-posed problem [225, 314]. Dealing with these kinds of ill-posed problems, this implies that there are several ways to obtain an approximate solution. It is reasonably possible to formulate the image blur problem taking into account the process of image formation and acquisition, as well as any other previously available possible information regarding the properties of the image to be restored. The most used approach to represent the denoising problem on a multispectral image is to treat it independently for each spectral channel, and express it in the form of a variational problem as

$$u \in \operatorname*{Argmin}_{v \in B_2} \left\{ \mathcal{J}(v) = R(v) + \frac{1}{2\lambda} \|Tv - u_0\|_{B_1}^2 \right\}, \tag{2.5}$$

where $B_1, B_2$ are two Banach spaces on $\Omega$, $u_0 \in B_1$ is the given image, $\lambda > 0$ outlines the optimization parameter, $T \in \mathcal{L}(B_1, B_1)$ is a bounded linear operator and $R : B_2 \to \mathbb{R}$ is the regularizing parameter that smooths the image $u$ and represents a sort of a priori information on the minimizer $u$. Here, the term $\|Tu - u_0\|_{B_1}^2$ describes the so-called fidelity term of the approach which forces the minimizer $u$ to stay close to the given image $u_0$ (how close depends on the value which assumes $\lambda$). As for the choice of the $T$ operator, it is generally set with $T = Id$ (i.e. the identity in $B_1$) for image denoising problems, and $T$ is a symmetric kernel with a smaller support than the image $u$ for the deblurring problems. Determining the most appropriate values for the different parameters is not trivial because they affect the quality of the desired image and also the consistency with the data provided. These parameters concern the choice for an adequate regularization $R(v)$ of the Banach spaces $B_1, B_2$ and a convenient fidelity term $\|Tv - u_0\|_{B_1}^2$. In the literature, there is a wide choice for the choice of the regularization term, so as to be able to guarantee that deals with a well-posed denoising problem (2.5). This term can generally be represented as follows

$$R(v) = \int_\Omega |Dv|^p \, dx \quad \text{with} \quad 1 \leq p \leq 2\,, \tag{2.6}$$

where $Dv$ stands for the generalized gradient. From this it follows that it is possible to take advantages of isotropic diffusion (when $p = 2$) arising from the minimization problem (2.5), from diffusion based on the total variation ($p = 1$) and, more in general, by anisotropic diffusion ($1 < p < 2$).

**Numerical Experiments**

In support of the algorithm presented for the denoising of hyperspectral satellite images, this section reports the results of some numerical experiments taking into account the choice of the parameters $T_i = Id$ for the three channels $i = R, G, B$. Some Sentinel-2 images over the geographical area of Dnipro, Ukraine (see Fig. 2.10) are used as input data, as then represent typical agricultural areas with medium-sized fields of various shapes. To proceed with the numerical simulations, the bilateral constraints $1 \leq \gamma_{0,i} \leq v(x) \leq \gamma_{1,i}$ are eliminated from the sets $\mathcal{B}_{i,p(\cdot)}$, ensuring that this condition is satisfied at each time step of the numerical approximations. The approach used to reach the solution is based on a parabolic equation in which time is passed as an evolution parameter, or equivalently, the gradient descent method. Consequently, an iterative algorithm is chosen, so that at the $k$-th step of the iterative process, it is possible to solve the following Cauchy-Neumann problem

$$\frac{\partial u^k}{\partial t} = \operatorname{div}\left(|\nabla u^k|^{p_k(x)-2}\nabla u^k\right) - \mu \frac{T_i^* u^k}{|T_i\left(u^k\right) - u_{0,i}|},\ (t,x) \in (0,\infty)\times\Omega\,, \tag{2.7}$$

$$u^k(0,x) = u_{0,i} \quad \forall\, x \in \Omega\,, \tag{2.8}$$

$$\frac{\partial u^k(t,\cdot)}{\partial n} = 0 \quad \text{on} \ \ \partial\Omega\,. \tag{2.9}$$

As $t$ increases, a noise-free image tends to be achieved upon reaching the $k$-th iteration. The numerical scheme in two spatial dimensions is presented below.

$$\begin{aligned} x_l &= lh,\ y_j = jh, \quad l,j = 0,1,\ldots,N \quad \text{with } Nh = 1,\\ t_n &= n\Delta t, \quad n = 0,1,\ldots, \quad u_{lj}^n = u^k(t_n, x_l, y_j), \quad u_{lj}^0 = u_{0,i}(lh, jh). \end{aligned}$$

Then, the numerical approximation to the problem (2.7)–(2.9), takes the form

$$\begin{aligned} u_{lj}^{n+1} &= u_{lj}^n + \frac{\Delta t}{h}\Delta_-^x\left(\frac{\Delta_+^x u_{lj}^n}{\sqrt{\left(\Delta_+^x u_{lj}^n\right)^2 + \left(m\left(\Delta_+^y u_{lj}^n, \Delta_-^y u_{lj}^n\right)\right)^2 + \varepsilon}}\right)\\ &+ \frac{\Delta t}{h}\Delta_-^x\left(\frac{\Delta_+^y u_{lj}^n}{\sqrt{\left(\Delta_+^y u_{lj}^n\right)^2 + \left(m\left(\Delta_+^x u_{lj}^n, \Delta_-^x u_{lj}^n\right)\right)^2 + \varepsilon}}\right)\\ &- \Delta t\mu\frac{T_i^* u_{lj}^n}{|T_i u_{lj}^n - u_{lj}^0 + \varepsilon|}, \quad \forall\, l,j = 1,\ldots,N\,, \end{aligned} \tag{2.10}$$

with boundary conditions

$$u^n_{0j} = u^n_{1j}, \quad u^n_{Nj} = u^n_{N-1,j}, \quad u^n_{l0} = u^n_{l1}, \quad u^n_{lN} = u^n_{l,N-1}.$$

Here, $\Delta^x_{\pm} u_{lj} = \pm\left(u_{l\pm1,j} - u_{lj}\right)$, $\Delta^y_{\pm} u_{lj} = \pm\left(u_{l,j\pm1} - u_{lj}\right)$, and

$$m(a,b) = \operatorname{minmod}(a,b) = \frac{\operatorname{sgn} a + \operatorname{sgn} b}{2} \min\left(|a|, |b|\right).$$

A step size restriction is imposed for stability by condition: $\Delta/h^2 \leq C$. The values for the simulations, we have $\varepsilon = 0.01$, $\sigma = 0.5$, $a = 5$, $\beta = 2$, $\gamma_{0,i} = 1$, $\gamma_{1,i} = 255$, $T_i = Id$, $i = 1, 2, 3$. For the three-channel RGB satellite image, represented in the left panel in Fig. 2.10, $k = 5$ iterations are conducted with a time step $\Delta t = 0.01$ for each iteration, and the result of which is shown on the right panel of Fig. 2.10. Useful for comparison, in the central panel of Fig. 2.10, the result of noise removal using the ROF model is shown.

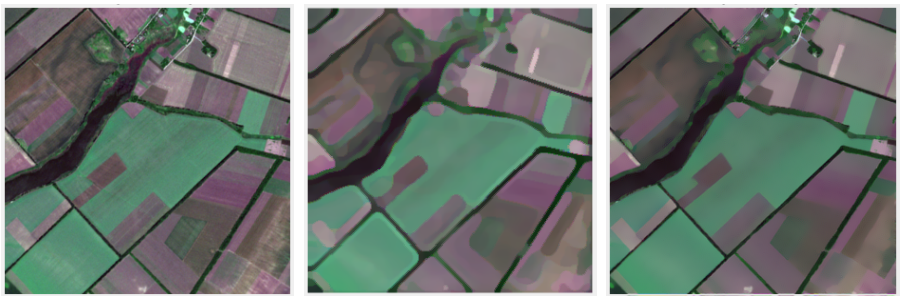

Figure 2.10: Example. Left panel: noisy satellite image. Middle panel: reconstruction using Total Variation (TV) approach. Right panel: reconstruction using the described approach.

## 2.4 A two-level variational model to predict daily surface reflectance at Landsat high spatial resolution and Modis temporal frequency

The advent of satellites built for remote sensing, mapping and systematic observation of the earth's surface (e.g. Landsat, QuickBird, Envisat, IKONOS or RapidEye, CryoSat satellites) have found various areas of use. Over the last 40 years, the Landsat satellite has found application in the study of the environment and the natural and artificial changes that have occurred on the earth's surface. Landsat is widely used in many applications, such as mapping land cover changes,

in the agricultural sector for monitoring crop conditions, estimating crop yield and for many other purposes. The feature that makes Landsat ideal for vegetation mapping is that it has medium resolution sensors. However, its use is limited due to the period, equal to 16 days, i.e. the amount of time necessary for the subsequent observation of the same area, which makes it limited in its use for the study of global biophysical processes, as the processes linked crop development evolves faster than the period required for a new Landsat pass, and above all even more rapidly during the growing season. In addition, there is also the real possibility that the images contain noise due to the presence of clouds, where in some cases the researchers estimated that they could obtain 2-3 cloud-free Landsat scenes over the course of a year. This is obviously insufficient for many applications that require denser temporal information, such as crop condition monitoring and phenology studies [226, 227]. A possible alternative to satisfy practical applications is to use MODIS (Moderate Resolution Imaging Spectroradiometer) data, albeit at a coarse resolution but with a higher frequency, in order to have a greater quantity of information. The characteristic of MODIS data is that it can be provided with a daily repetition period and 500-m surface reflectance, and the repeat cycle of Landsat is 16 days with Enhanced Thematic Mapper Plus (ETM+) 30-m surface reflectance. The intuition is to be able to jointly use Landsat and MODIS data to generate synthetic "daily"surface reflectance products with spatial resolution ETM+ [228]-[230]. The STARFM model (Spatial and Temporal Adaptive Reflectance Fusion Model) is just one of these models which is based on the intuition just described (see, for example, [226, 227], [231]-[233]). This model (as well as many other generalizations) allows to produce images with daily surface reflectance starting from the Landsat spatial resolution and the MODIS temporal frequency, drawing inspiration from a deterministic weighting function calculated from the spectral similarity. As far as performance is concerned, they essentially depend on the characteristic patch size of the landscape and get slightly worse if used on extremely heterogeneous fine-grained landscapes [226]. This approach has the fundamental characteristic that provides the possibility of being able to generate MODIS synthetic images, with a "daily"frequency and with an ETM+ spatial resolution composed of two phases. The first phase considers solving the temporal interpolation problem to predict total spectral energy of a presumably non-existent Landsat image for a given day. Subsequently, starting from the geometric information contained in the total spectral energy of this image, it is proposed the reconstruction of the "daily"MODIS product having ETM+ spatial resolution and constraining the geometry of all its high resolution spectral channels to the geometry of the panchromatic image. The panchromatic image appears in different shades of gray and is more suitable for identifying the shapes and contours of topographical details. The variational approach can be summarized through the

scheme shown in Fig. 2.11.

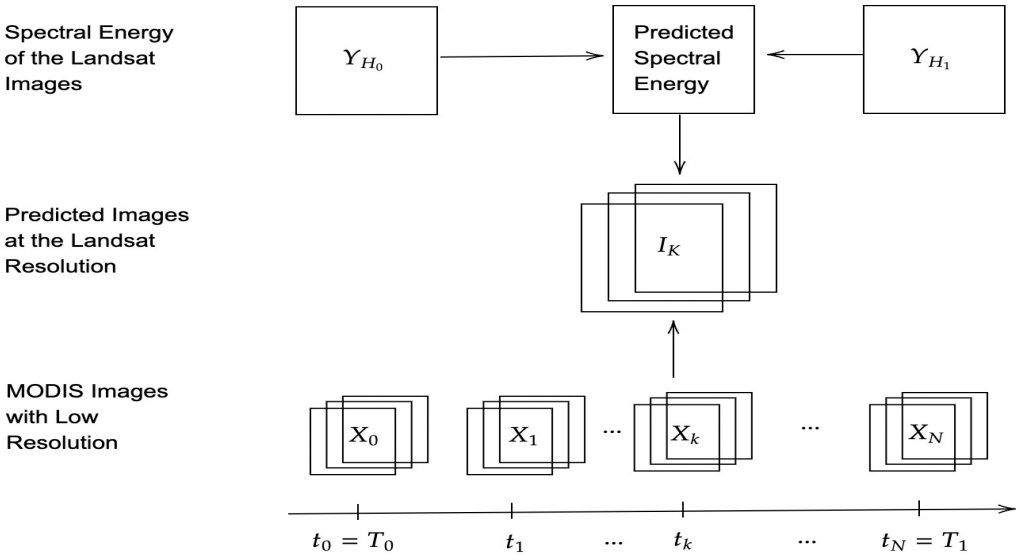


Figure 2.11: The scheme of spatiotemporal interpolation of the MODIS-like images.

Here, the scalar functions $Y_{H_0}$ and $Y_{H_1}$ stand for the total spectral energies of the Landsat-like cloud-free images $\{H_0, H_1 : \Omega \to \mathbb{R}^m\}$ with high resolution sample grid $S_H$ on a given rectangle domain $\Omega \subset \mathbb{R}^2$, and $\{X_0, X_1, \ldots, X_N : \Omega \to \mathbb{R}^n\}$ are the MODIS images with low resolution that are taken at time instances $\{t_0, t_1, \ldots, t_N\}$, respectively. The problem examined is summarized as follows: for every $k = 0, \ldots, N$, using only the data $H_0 : S_H \to \mathbb{R}^m$, $H_1 : S_H \to \mathbb{R}^m$, and $X_k : S_L \to \mathbb{R}^n$, one must increase the resolution of the $n$ band image $X_k : S_L \to \mathbb{R}^n$ at ETM+ spatial resolution. Most image interpolation techniques are mainly based on data and the corresponding acquisition devices (see [218]). It is often assumed that the high spatial resolution image can be obtained as a result of a linear combination of the spectral channels with known weights [234]. Furthermore, the resolution loss is generally modeled as a linear operator consisting of a subsampled convolution with known kernel (point spread function). In a practical context, both hypotheses would entail a difficulty whereby it may not be easy to obtain a measurement or estimate the weights and the convolution kernel, contrary to how they can be justified in some applications. As an alternative to this, a space-time interpolation of images similar to MODIS is formulated, as a two-level optimization problem, and having two further sub-problems of which: temporal and spatial interpolation.
In the first level, there is the temporal interpolation problem for the total spectral

energy of Landsat images, which can be presented as a state constrained optimal control problem for anisotropic convection-diffusion equation. The model for the total spectral energy interpolation discussed here is significantly different from the approach proposed by Horn & Schunck in [235], which is based on the optical flow constraint, or from that proposed by Hinterberger & Scherzer in [236], and by Chen & Lorenz in [237]. The [238] models proposed by Borzi et al. relating to the problem of interpolation of image sequences is treated in terms of optimal control governed by the transport equation. The model discussed here considers the drift-diffusion equation with the edge-weighted anisotropic diffusion operator, with homogeneous Neumann boundary conditions, and two further types of controls, the first relating to the optical flow field $b$ and the second concerns the source of the image intensity $v$. It is illustrated that, although there are rather weak regularity hypotheses on the control variables, this optimal control problem is coherent and admits at least one solution. In this context, when it is possible to talk about consistency it is just like in this case where the problem of optimal control has a non-empty set of feasible solutions and the objective functional turns out to be well defined on this set (see [239] for further details). The solution described above can be considered as a suitable background for daily prediction of the total spectral energy of Landsat images. In the second level, the problem of spatial interpolation is considered in order to increase the resolution of multispectral images acquired according to the MODIS mode, and their fusion with the total spectral energy expected from high-resolution Landsat images. According to what has just been said, it is possible to formulate a special constrained minimization problem, in which the functional costs have a non-standard growth. Edge information regarding the restoration of MODIS images to the resolution provided by Landsat is accumulated in both the variable exponent of the nonlinearity and the directional gradients of the image, and it is derived from the solution of the optimal control problem reported above. The proposed approach is based on the variational model in the Sobolev-Orlicz space, with non-standard growth condition of the objective functional and also on the assumption that, to a large extent, the topology of the image in each spectral channel is contained in the topographic map of its spectral energy. It is important to remember that this model is significantly different from the variational model for P+XS image fusion, proposed in [240]. The above approach is discussed in order to establish the completeness and consistency of the corresponding variational problem, showing that this problem admits a single solution. Consequently, some optimality conditions are also treated and for this approach the results of numerical simulations with real satellite images are reported.

The aim of the above is to study the accuracy of the space-time interpolation problem, following the proposed two-level variational model and to provide a rigorous

mathematical explanation for it.

### Numerical Experiments

This section reports the results obtained through numerical experiments relating to the proposed algorithm for the problem of space-time interpolation of MODIS multi-spectral images through their fusion with higher resolution Landsat images. To carry out these tests, the data source provided as input is a collection of MODIS images with resolution $500m/pixel$ (see Fig. 2.12) received from the Terra satellite in the period from 13 July to 10 August 2021. The region of interest represents a typical agricultural area of Australia, with fields having medium-sized sides and various shapes. There are two images including the same geographical area with

July 13, 2021 July 13, 2021 July 13, 2021 July 13, 2021 July 13, 2021

$X_1$ $X_2$ $X_3$ $X_4$ $X_5$

Figure 2.12: The collection of MODIS images with resolution $500m/pixel$. The real size of each image is $39 \times 39$ pixels.

resolution $30m/pixel$, obtained from acquisition via Landsat satellite at the times $T_1 =' July, 08'$ and $T_2 =' August, 25'$. Each of these frames has dimensions equal to $1000 \times 1000$ pixels. The corresponding total energies of these images are depicted in Fig. 2.13.
With the aim of proposing a solution to the optimal control problem, it is possible to set $\gamma = 1$, $\lambda = 10$, and define the function $Y^*(t, x)$ in $Q$. Therefore, the optimal control algorithm leads us to the following optimal triplet $(\boldsymbol{b}^0, v^0, Y^0)$, where $\boldsymbol{b}^0 = 0$ and the peak of the ratio signal-to-noise between images $Y^0(T_1, x)$ and $Y_{H_1}(x)$ is equal to 36.41. In Fig. 2.14 the $Y^0(t_3, \cdot)$ and $Y^0(t_4, \cdot)$ screens of the optimal state are shown. It is believed that the optimal control solution $Y^0 \in C([0, T]; L^2(\Omega))$ can be considered as an acceptable approximation of the evolution of the total Landsat spectral energy in the interval of time $[T_0, T_1]$.
The next step is to find the solutions to the constrained minimization problem for the values $k = 3$ and $k = 4$. Taking into account the following parameters $\mu = 5.0$, $\lambda = 1.0$, $\eta = 0.95$ and using the bicubic interpolation of MODIS images $X_3$ and $X_4$ (see Fig. 2.15) as initial condition for the optimality system, after 35 iterations with the step $\Delta t = 0.05$, the following prediction of the daily MODIS

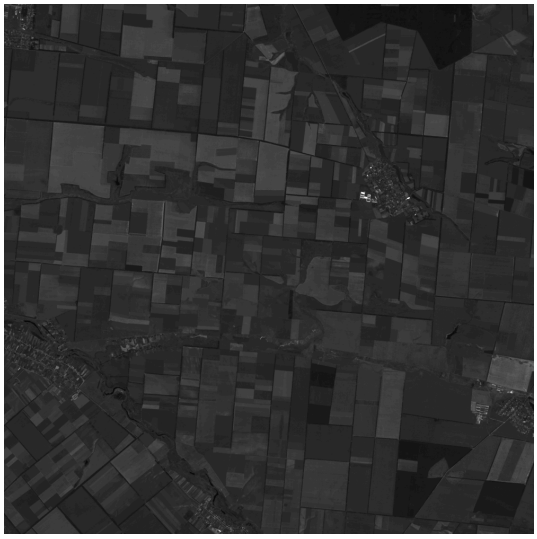

$Y_{H_1}$

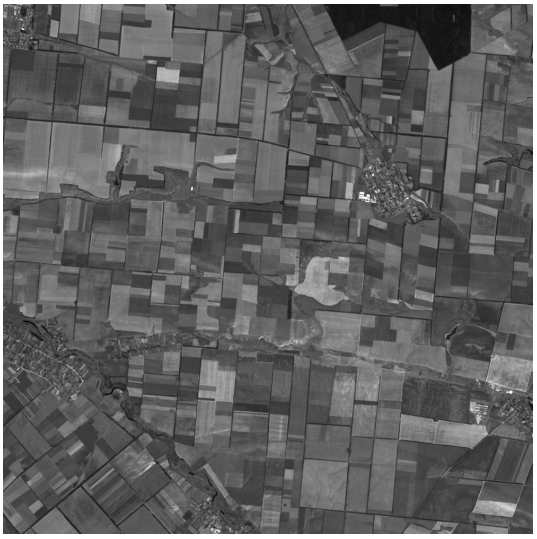

$Y_{H_2}$

Figure 2.13: The spectral energies of the Landsat images $H_0$ and $H_1$ with resolution $30m/pixel$. The real size of each image is $1000 \times 1000$ pixels.

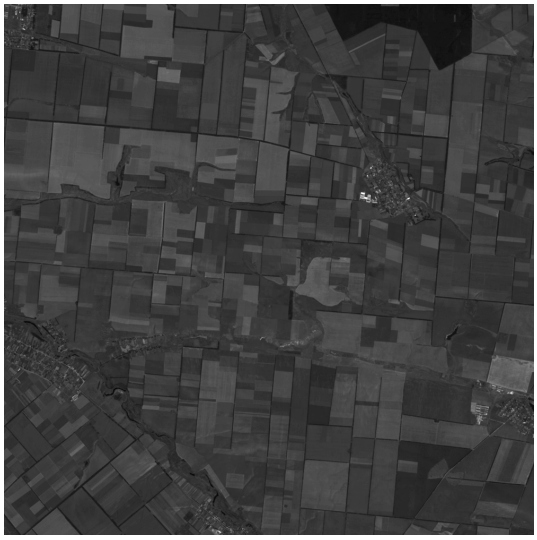

$Y^0(t_3, \cdot)$

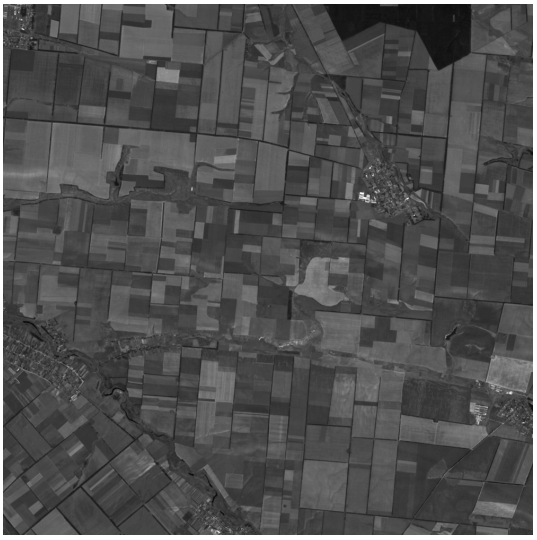

$Y^0(t_4, \cdot)$

Figure 2.14: The screenshots of the optimal solution taken at the time instances $t_3$ and $t_4$, respectively.

surface reflectance at Landsat resolution is obtained (see screenshots of $I_3$ and $I_4$ represented in Fig. 2.16).
Below there are some images in order to make a comparison of how close the

Interpolated $X_3$

Interpolated $X_4$

Figure 2.15: The screenshots of the bicubic interpolation of MODIS images $X_3$ and $X_4$ taken at the time instances $t_3$ and $t_4$, respectively.

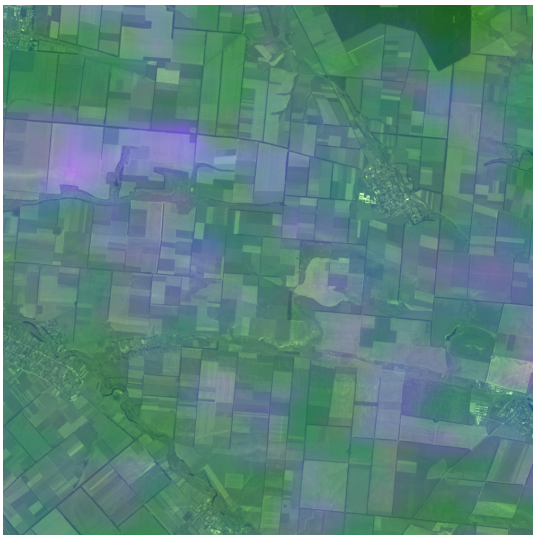

Spatiotemporal interpolation of $X_3$

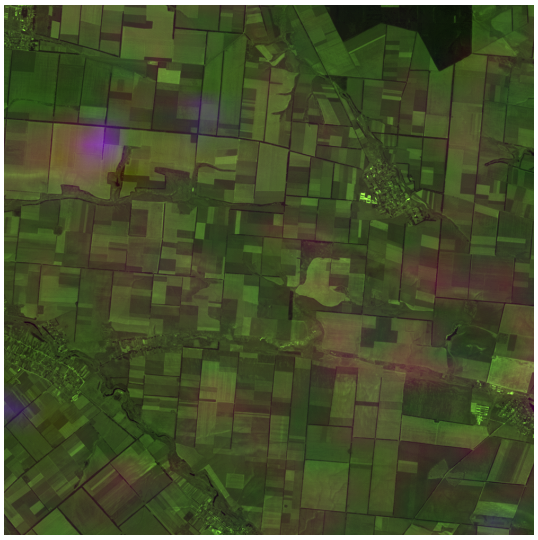

Spatiotemporal interpolation of $X_4$

Figure 2.16: Result of spatiotemporal interpolation of the MODIS images $X_3$ and $X_4$ following the proposed approach.

radiometric results are between the original image and the interpolated one. In particular, Fig. 2.17 shows a graph of the ratios using the data represented in

Fig. 2.16 and Fig. 2.15. The proposed approach allows capturing significant portions of information from MODIS images to produce them with Landsat level of accuracy.

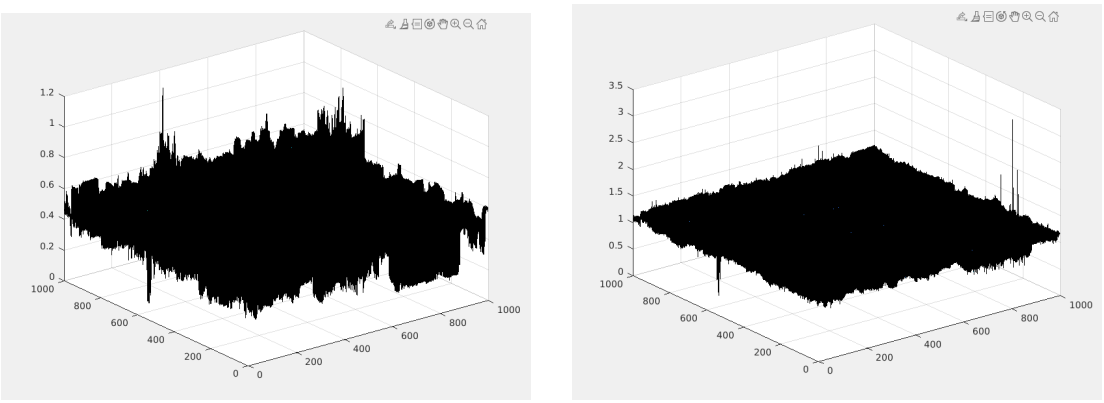


$Y_{I_3}(x)/Y(t_3,x)$ $Y_{I_4}(x)/Y^0(t_4,x)$

$$x \in \Omega = [0,1000] \times [0,1000]$$

Figure 2.17: Ratio of the spectral energies of the predicted MODIS images $I_3$ and $I_4$ at the Landsat level of resolution to the approximated total energies $Y^0(t_3,\cdot)$ and $Y^0(t_4,\cdot)$, respectively.

## 2.5 Contrast enhancement of color images

In the field of image processing by optical devices, it is possible to have problems due to the presence of poor lighting, thus generating under-lighted images, or, on the contrary, problems due to the presence of too much lighting which leads the image to be over-lighted. This situation represents a difficulty that has already been well known for a long time, and in the past this obstacle was managed through manual processes, acting directly on the negative of the photographic film within an environment called darkroom. Nowadays, this same technique occurs through digital processes, which however require manual intervention by the user, which can sometimes be tedious when this treatment is to be applied to many images.
Recently, several contrast enhancement techniques for digital images have been presented. Some of these techniques resort to the use of multiple views or sensors and are able to improve the contrast of the image in low light conditions [274, 275], acting in an attempt to modify the gray level of objects not only in proximity of the contours. Then, there are other techniques called sharpening, which remove the blur and are based on Gaussian convolution [40] in order to obtain an enforcement of the strong contours.

Existing methods to address the problem of contrast enhancement of natural images, captured with digital devices, can be grouped into the following three groups:

- spectral methods;
- histogram methods;
- spatial methods.

**Spectral methods.** This group includes those methods that are based on wavelets or homomorphic filtering. The method proposed by Laine et al. [241], involves the use of the wavelet transform which is applied in the wavelet domain with a non-linear operator applied to the wavelet coefficients, thus obtaining both noise reduction and improvement. As for noise reduction, it is achieved by applying soft and/or hard thresholding of high frequency bands. In [10] however, the homomorphic filtering is preceded by a logarithmic transformation, and is nothing more than a high-pass filter that improves the sharpness of the image, even if it is possible that there are some artefacts similar to those of Gibbs or an increase of the noise.

**Histogram methods.** Various methods belong to this group and are presented below. These methods have been the subject of in-depth studies and there is a wide presence in the literature. The Histogram Specification (HS), to which many of the following methods refer, takes a grayscale image as input and applies a transformation to it in order to obtain an output image according to a previously specified histogram. A special case of HS is Histogram Equalization, in which the specified histogram is the uniform one. In [242] Mignotte proposes to perform HS based on the first-order derivative distribution with the aim of strengthening the edges. Sim et al. in [243] present a PDE to modify the histogram. This approach has the dual advantage of improving both image contrast and at the same time reducing noise. Sole et al. [244] propose to preserve shapes in the original image based on HS and first and second-order derivatives. Wang et al. [245] present an approach that uses an a priori value on the histogram, so as to maximize the entropy of the output image produced. Arici et al. [246] propose a variational approach that makes a trade-off between the input image histogram and the uniform one. In cases of discontinuity in the histogram, the addition of a smoothing term is envisaged.
In some approaches, such as those to follow, a division the histogram specification into sub-histogram specifications is applied. This is the case of Kim [247] where the values of the original image are divided in order to equalize the two sub-histograms. Chen et al. [248] propose to perform this division through the

use of a recursive procedure. Sim et al. [249] adopt an algorithm whose division is based on the median. Wadud et al. [250] prefer to divide the histogram into several sub-histograms in order to obtain separate equalizations of the complete histogram, so as to protect even the smallest characteristics of the input image. Inspired by this same principle, Celik et al. [251] model the histogram as a set of Gaussians. Other methods are adaptive, as the improvement occurs locally, and in this regard, please refer to what is described in [252]-[255]. As regards the division techniques, for further details it is advisable to refer to the contents in [256].
A common difficulty to all techniques that can be traced back to histograms is that relating to the rigorous and meaningful ordering of pixel values. When this difficulty disappears, HS can be performed in a simple way, as for example described in [257]. Therefore, various methods have been implemented in order to obtain meaningful orderings such as the local average ordering [258], the wavelet-based ordering [259], the variational approach based on the minimization of a fully smoothed $\ell_1$-TV functional [257, 260] and its corresponding fast version discussed in [261]. It is worth mentioning that HS can also be used on the color histogram, such as on a color image with the desired contrast, using the variational framework, as described in [262]. Nikolova et al. in [263, 264] propose a two-phase algorithm, composed of an initial phase of a HS of the intensity image and subsequently followed by a hue and range preserving color adjustment. For further tools in this regard, please refer to [265].

**Spatial methods.** These methods are employed in the context of histogram approaches that modify pixel values without considering spatial constraints. The method proposed by Boccignone [266] resorts to the use of the anisotropic diffusion equation of Perona and Malik [21] in a multi-scale framework. Many of the spatial methods take into account the assumptions of the Human Visual System (HVS). In this sector the Retinex model proposed by Land et al. in [267] found widespread approval. Taking into account that two pixels, distant from each other but both having the same intensity value, are perceived by a human being as two pixels with different intensities, it is possible to clarify what has just been stated through the example shown in the Fig. 2.18, which reports the experiments of the Checker shadow illusion of Adelson [268]. Although the two squares A and B have the same intensity value, their gray levels are perceived as different by the HVS. The proposed method is based on this impediment, the objective of which is to obtain an improvement in the contrast of the image by modifying the values, the darker ones for the darker square A and the lighter ones for the darker square B become lighter. The final result aims to achieve the objective of improving contrasts even if the perceived intensity would be the same.
A method based on a perceptual hypothesis is the one proposed by Rizzi et al.

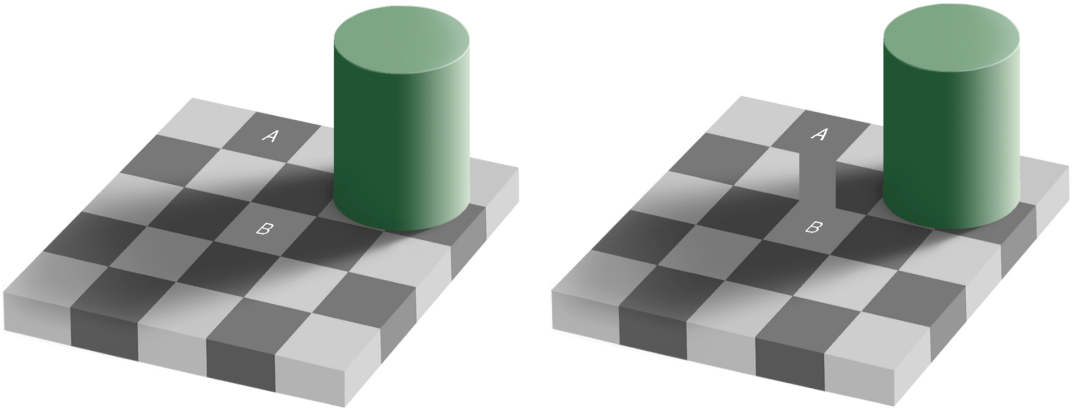


(a) Checker shadow illusion of Adelson (b) Proof of illusion

Figure 2.18: Checker shadow illusion by Adelson.

[269], called Automatic Color Equalization (ACE). This approach is extended and integrated with a variational model by Bertalmio et al. [284]. The method is subsequently generalized for a larger class of functionals thanks to Palma-Amestoy et al. [270] and implemented in [271]. The contribution of Provenzi et al. [272] aims to reduce the computation time, proposing to work in the wavelet domain. Some connections between these works and the Retinex model have been studied and illustrated in [273].

**Variational contrast enhancement of gray-scale and RGB images.** In this context, the method proposed by Pierre et al. [276] provides an enhancement of the gray values in an image, as well as the following benefits:

- intuitive contrast level control,
  which is obtained through the intuitive setting of a parameter;
- choice of spatial contrast scale,
  which consists in the possibility of being able to choose a spatial scale defined by the user based on its application, in order to obtain a reliable improvement;
- slight histogram change,
  as the proposed method does not strongly modify the histogram of the original image, thus allowing the global illumination conditions to be safeguarded;

- the tone of the original image is almost maintained,
  the tone of the output image must be as close as possible to that of the input image, and in fact the tone does not change with changes in lighting.

**Numerical Experiments**

This section reports the results obtained through numerical experiments relating to the algorithm, which are conducted with the aid of MATLAB. These tests are carried out on a sample of color images and compared with current methods.
The values chosen to carry out these tests are: $\lambda = 100$, $\mu = 1$, $\alpha = 100$, $\beta = 500$, $\sigma = 5.10^{-5}$, $\tau = 5.10^{-9}$ and a number of iterations equal to $10^3$. As for the polynomial approximation, Bernstein polynomials of degree 9 are used. The size of the Gaussian kernel used for C depends on the size of the image. During the experiments phase the chosen value is equal to $min(M, N)/20$. This dimension manages the scale of the contrast enhancement.
By illustrating various images shown below in Fig. 2.19, it is possible to make a visual comparison based on various equalization implementation methods: Gimp, the algorithm of Nikolova et al. [261, 264] with implementation [265], the method of Bertalmio et al. [284] and the one of Ferradans et al. [271], of Pierre et al. [276] which produces good results in all these cases.
From each single image shown in the Fig. 2.19, it is possible to note that, for the image *Jupiter* the Gimp, [284] and [271] methods modify the histogram thus generating a peak corresponding to the background of the image and therefore these methods are not effective for this type of images. [276] does not make any changes to the histogram and therefore also leaves the background of the image itself unchanged.
As for the second image where there is a *Chandelier*, the Gimp, [284] and [271] methods modify the color of the ceiling due to the lack of preservation of the shade. Instead, the [264] and [276] methods return an image with a hue that is almost faithful to the original one.
In the third image showing the *Sunrise*, the results proposed by the various methods produce over-contrasted results, in particular near the sun. However, by applying [276] more satisfactory results are obtained as it is even possible to clearly see the building in the center of the image.
The next image, the *Iris*, when treated with the Gimp methods, [271, 284] produce an image with a purple background due to the hue modification, while [264] respects the key. Instead, the [276] algorithm manages to maintain the contrast level and hue, and it is also able to highlight the visibility of the leaf veins.
Finally, analyzing the image relating to the *Cathedral*, it is possible to notice that each method produces different but still improving results. It should be noted that current methods focus on improving the details in the foreground, while [276] aims

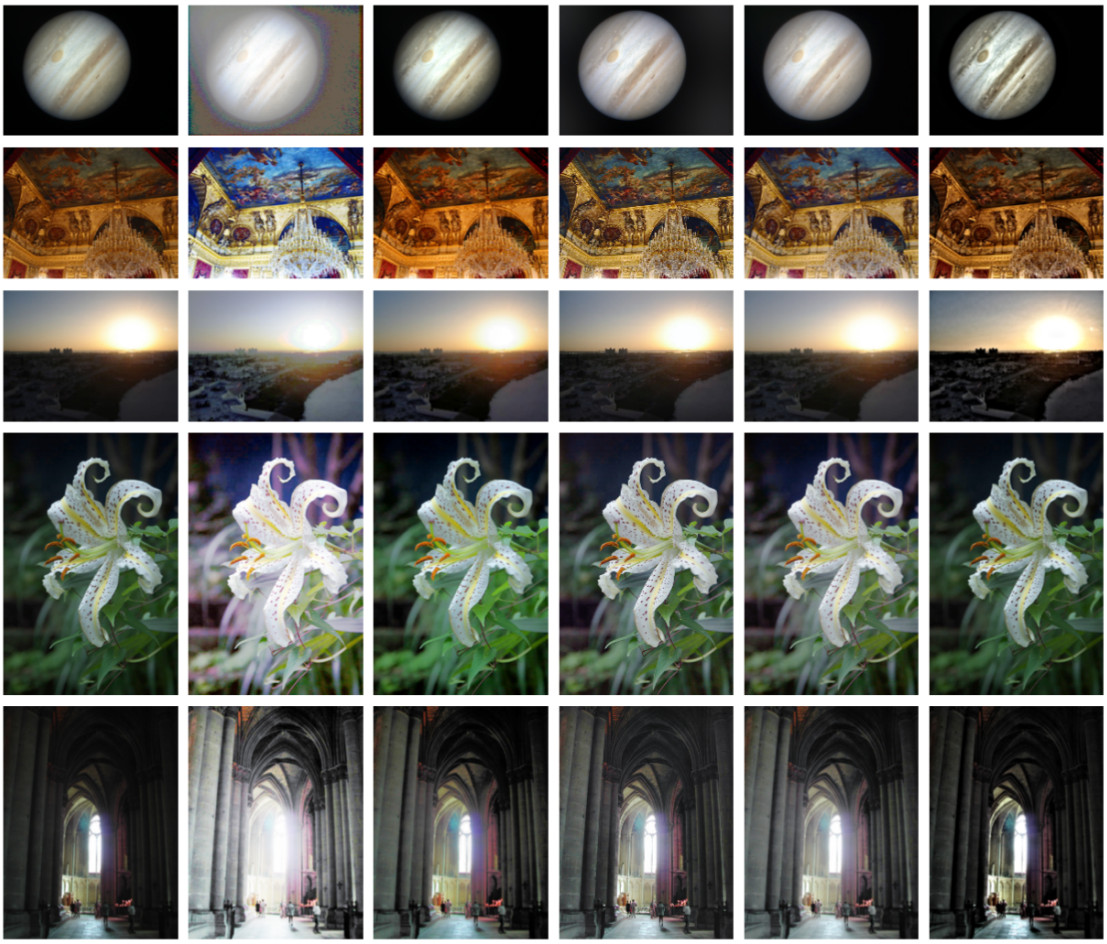


Figure 2.19: Comparison of enhancement results with those obtained by the algorithms of the Gimp histogram equalization, of Nikolova et al., of Bertalmio et al., of Ferradans et al. and Pierre et al. which produces good results in all these cases.

to strengthen the quality of the background. Likewise, the perception of lighting is also different in different approaches. In fact, in all approaches you have the sensation that the light source comes from behind the photographer, while [276] preserves the sensation of light and shadows in the scene, thanks to the contrast enhancement scale which allows you to recover various details.

# Chapter 3

# Variational model with nonstandard growth condition in image restoration and contrast enhancement

## 3.1 Introduction

A very promising approach to image quality enhancement is to reduce the influence of noise and improve the perceptibility of objects in the scene by increasing the brightness difference between objects and their background. In recent years, many contrast enhancement techniques have been proposed for digital images. Some approaches allow to improve image contrast just in low light conditions [274, 275]. Other methods, called sharpening, focus on enforcing strong contours to remove the obtained blur, e.g., by Gaussian convolution [40]. However, this kind of enhancement concerns only strong image contours while the contrast enhancement attempts to modify the grey level of objects not only in the contours neighbourhood. In recent years, many different techniques have been proposed for the reconstruction of noise-affected digital images and their contrast enhancement. In [276], the authors focus on the problem of contrast enhancement of natural images captured with a digital camera, and give a sufficiently complete overview of the existing methods with detailed analysis of all pros and cons.

In this chapter [277], we mainly focus on the development of a variational approach for simultaneous contrast enhancement of color images and their denoising. With that in mind, it is proposes a new variational model in Sobolev-Orlicz spaces with non-standard growth conditions of the objective functional and there is a discussion of its applications to the simultaneous fusion and denoising of each

spectral channel for input color images. In contrast to [278], it is not provided the color image restoration using saturation-value Total Variation, but instead, the RGB representation of color images is considered. However, as follows from the results of numerical simulations, the proposed approach does not strongly modify the histogram of the original image. This enables the model to preserve the global lighting sensation and to show that the hue of the main objects does not drastically change with the illumination. One of the most important advantages of this approach is the fact that the proposed model allows to synthesize at a high level of accuracy noise- and blur-free color images, that were captured in extremely low light conditions. This situation is typical for most remote sensing problems. Indeed, real-life satellite images frequently suffer from different types of noise, blur, and other atmosphere artefacts that can affect the radiation recovered by the sensors. As a result, such images lose their efficiency for the crop field monitoring problems and their utilization can lead to erroneous results and inferences.

The characteristic feature of the proposed model is that there is a constrained minimization problem with a special objective functional that lives in variable Sobolev-Orlicz spaces. This functional contains a spatially variable exponent characterizing the growth conditions and it can be seen as a replacement for the 1-norm in TV regularization. Moreover, the variable exponent, which is associated with non-standard growth, is unknown a priori and it depends on a particular function that belongs to the domain of objective functional.

The idea of using a spatially varying exponent in a TV-like regularization method for image denoising dates back as early as 1997 [217] and it was put into practice in 2006 [220]. Both papers as well as some subsequent articles try to tackle variants of the problem

$$J(u) = \mathcal{D}(u) + \lambda \int_{\Omega} |\nabla u(x)|^{p(\nabla u(x))}\, dx \longrightarrow \inf, \tag{3.1}$$

where the exponent depends directly on the image $u$, e.g.,

$$p(\nabla u) = 1 + \frac{a^2}{a^2 + |\nabla G_\sigma * u|^2}. \tag{3.2}$$

Here, $(G_\sigma * v)(x)$ determines the convolution of function $v$ with the 2-dimensional Gaussian filter kernel $G_\sigma$.

It has been demonstrated that this model possesses some favourable properties, particularly when edge preservation and effective noise suppression are primary goals in image reconstruction. Furthermore, this model has been introduced specifically to address the issue of staircasing [279], which refers to the regularizer's inclination towards piecewise constant functions. The appearance of the staircase effect is a notable drawback of the classical TV model. However, the non-convex

model (3.1) did not gain significant attention for a long period due to its high numerical complexity and the absence of a rigorous mathematical substantiation of its consistency. Only particular solutions to this problem have been derived for a smoothed version of the integrand, using a weak notion of solution (see, for instance, [280]).

A recently developed alternative variant is the TV-like method [281] (see also [282, 283]), which computes the variable exponent $p$ in an offline step and keeps it as a fixed parameter in the final optimization problem This approach allows the exponent to vary based on spatial location, enabling users to locally select whether to preserve edges or smooth intensity variations. However, there are only two natural types of imaging problems where this approach can be applied:

- single-channel imaging where first the exponent is computed from the given data and then is applied as prior in the subsequent minimization problem;
- dual-channel imaging where the secondary channel provides the exponent map that is used for regularization of the primary channel.

Thus, this circumstance imposes significant limitations from a practical point of view, especially in the case of multi-spectral satellite noisy images, where different channels can differ drastically.

The main purpose of this chapter is to describe a robust approach for the simultaneous contrast enhancement and denoising of non-smooth multispectral images using an energy functional with nonstandard growth, in particular a special form of anisotropic diffusion tensor for the regularization term and a term which is inspired by the variational model of Bertalmio et al. [284]. Following this approach, the aim is to increase the perceptibility of objects in the scene and the noise robustness of the proposed model albeit it makes such variational problems completely non-smooth, non-convex, and, hence, significantly more difficult from a minimization point of view.

It is proposed a variational problem for the energy functional with nonstandard growth $p(x)$, where the principle edge information for the contrast enhancement is mainly accumulated. Namely, for the simultaneous denoising and contrast enhancement of color images, the aim is to solve the following constrained minimization problems

$$J_i(f_i^0) = \inf_{v \in \Xi_i} J_i(v), \quad i = 1, 2, 3\,, \tag{3.3}$$

for each spectral channel of an input image separately, where the objective functional is non-convex and takes the form

$$J_i(v) = \int_\Omega |R_\eta \nabla v(x)|^{p(|\nabla v|)}\, dx + Q_i(v). \tag{3.4}$$

Here, $Q_i(v)$ stands for the fidelity term and its specific form is described in detail in Section 3.3 together with the operator $R_\eta$. The principle point that should be emphasized is the fact that the exponent $p(x)$ is not predefined a priori using for that the original image, but instead, it si taken as

$$p(\nabla u) = 1 + \frac{a^2}{a^2 + |\nabla u|^2}. \tag{3.5}$$

So, in contrast to the well-known approach, coming from the pioneering papers [285, 23], the principle difference of the models (3.5) and (3.2) is that in (3.5) there is not any spatial regularization of gradient $\nabla u$. Because of this, the model (3.3)–(3.4) becomes an ill-posed problem from the mathematical point of view and can produce many unexpected phenomena. In particular, to the best knowledge, there are no results of the existence and consistency of the optimization problem (3.3)–(3.4). To overcome this problem, some regularization of the variable exponent $p(x)$ in the form like (3.2) is applied.

However, it is well-known that optimization problem (3.3)–(3.4) with the spatially regularized gradient has several serious practical and theoretical difficulties. The first one is that the spatial regularization of the gradient in the form (3.2) leads to the loss of accuracy in the case when the signal is noisy, with white noise (see, for instance, [23]). Then the noise introduces very large, in theory unbounded, oscillations of the gradient $\nabla u$. As a result, the conditional smoothing introduced by the model does not help, since all these noise edges are kept.

The second drawback of the model with the regularized gradient is the fact that the space-invariant Gaussian smoothing inside the divergent term tends to push the edges in $u$ away from their original locations. We refer to [286] where this issue is studied in detail. This effect, known as edge dislocation, can be detrimental, especially in the context of the boundary detection problem and its application to remote sensing and monitoring.

In view of this, the main interest is to study the optimization problem (3.3)–(3.4) without the space-invariant Gaussian smoothing of the variable exponent $p(x)$. In summary, the main contributions of the research activity are enumerated as follows:

- The variational statement for the simultaneous contrast enhancement and denoising of multispectral images in the form of minimization problem in Sobolev-Orlicz spaces with non-standard growth conditions of the objective functional.

- Rigorous substantiation of the well-posedness of the variational problem with non-standard growth functional.

- The proof of existence results to the approximation variational problems.

- The iterative algorithm for numerical implementations.
- Derivation of the first order necessary conditions for the original problem and their substantiation.
- Numerical experiments to study the performance of the new approach.

The remainder of the chapter is organized as follows: In Section 3.2 there are preliminaries and some auxiliaries results. In Section 3.3 a novel variational problem for the denoising and contrast enhancement of non-smooth RGB images, which can be viewed as an improved version of the variational model that has been recently proposed in [287], is presented. Section 3.4 is devoted to the derivation of optimality conditions to the original problem and their substantiation. In Section 3.5, there is the discussion of the possible ways for the relaxation of the minimization problem and its approximation. Specifically, it is introduced a family of special minimization problems and it is show that each of these problems is solvable and their solutions are compact in an appropriate topology. Their approximating properties are discussed and convergence criterion of such sequence to an optimal solution of the original problem is provided. Finally, for illustration, some results of numerical experiments are in Section 3.6.

## 3.2 Preliminaries

Let us recall some useful notations. For vectors $\xi \in \mathbb{R}^2$ and $\eta \in \mathbb{R}^2$, $(\xi, \eta) = \xi^t \eta$ denotes the standard vector inner product in $\mathbb{R}^2$, where $^t$ stands for the transpose operator. The norm $|\xi|$ is the Euclidean norm given by $|\xi| = \sqrt{(\xi, \xi)}$. Let $\Omega \subset \mathbb{R}^2$ be a bounded open set with a Lipschitz boundary $\partial\Omega$ and nonzero Lebesgue measure. For any subset $E \subset \Omega$ we denote by $|E|$ its 2-dimensional Lebesgue measure $\mathcal{L}^2(E)$. Let $\overline{E}$ denote the closure of $E$, and $\partial E$ stands for its boundary. Let $\Omega \subset \mathbb{R}^2$ be a bounded connected open set with a sufficiently smooth boundary $\partial\Omega$.

### 3.2.1 Functional spaces

For the convenience of the reader, we collect here the basic facts on functional spaces that will be used in the sequel. Let $X$ denote a real Banach space with norm $\|\cdot\|_X$, and let $X'$ be its dual. Let $\langle \cdot, \cdot \rangle_{X';X}$ be the duality form on $X' \times X$. By $\rightharpoonup$ and $\overset{*}{\rightharpoonup}$ we denote the weak and weak$^*$ convergence in normed spaces, respectively. For given $1 \leq p \leq +\infty$, the space $L^p(\Omega; \mathbb{R}^2)$ is defined by

$$L^p(\Omega; \mathbb{R}^2) = \left\{ f : \Omega \to \mathbb{R}^2 \ : \ \|f\|_{L^p(\Omega;\mathbb{R}^2)} < +\infty \right\},$$

where $\|f\|_{L^p(\Omega;\mathbb{R}^2)} = \left(\int_\Omega |f(x)|^p\,dx\right)^{1/p}$ for $1 \le p < +\infty$. The inner product of two functions $f$ and $g$ in $L^p(\Omega;\mathbb{R}^2)$ with $p \in [1,\infty)$ is given by

$$(f,g)_{L^p(\Omega;\mathbb{R}^2)} = \int_\Omega (f(x),g(x))\;dx = \int_\Omega \sum_{k=1}^{2} f_k(x)g_k(x)\,dx.$$

We denote by $C_c^\infty(\mathbb{R}^2)$ a locally convex space of all infinitely differentiable functions with compact support in $\mathbb{R}^2$. We recall here some functional spaces that will be used. We define the Banach space $H^1(\Omega)$ as the closure of $C_c^\infty(\mathbb{R}^2)$ with respect to the norm

$$\|y\|_{H^1(\Omega)} = \left(\int_\Omega \left(y^2 + |\nabla y|^2\right)\;dx\right)^{1/2}.$$

We denote by $(H^1(\Omega))'$ the dual space of $H^1(\Omega)$. Hereinafter, $W^{1,1}(\Omega)$ stands for the Banach space of all functions $u \in L^1(\Omega)$ with respect to the norm

$$\|u\|_{W^{1,1}(\Omega)} = \|u\|_{L^1(\Omega)} + \|\nabla u\|_{L^1(\Omega)^2}.$$

Given a real Banach space $X$, we will denote by $C([0,T];X)$ the space of all continuous functions from $[0,T]$ into $X$. We recall that a function $u : [0,T] \to X$ is said to be Lebesgue measurable if there exists a sequence $\{u_k\}_{k\in\mathbb{N}}$ of step functions (i.e., $u_k = \sum_{j=1}^{n_k} a_j^k \chi_{A_j^k}$ for a finite number $n_k$ of Borel subsets $A_j^k \subset [0,T]$ and with $a_j^k \in X$) converging to $u$ almost everywhere with respect to the Lebesgue measure in $[0,T]$.

Then for $1 \le p < \infty$, $L^p(0,T;X)$ is the space of all measurable functions $u : [0,T] \to X$ such that

$$\|u\|_{L^p(0,T;X)} = \left(\int_0^T \|u(t)\|_X^p\,dt\right)^{\frac{1}{p}} < \infty,$$

while $L^\infty(0,T;X)$ is the space of measurable functions such that

$$\|u\|_{L^\infty(0,T;X)} = \sup_{t\in[0,T]} \|u(t)\|_X < \infty.$$

A full presentation of this topic can be found in [288].

Let us recall that, for $1 \le p \le \infty$, $L^p(0,T;X)$ is a Banach space. Moreover, if $X$ is separable and $1 \le p < \infty$, then the dual space of $L^p(0,T;X)$ can be identified with $L^{p'}(0,T;X')$.

### 3.2.2 Basic facts on the Lebesgue and Sobolev spaces with variable exponents

Let $p : \Omega \to [p^-, p^+] \subset (1, +\infty)$, with $p^\pm = \text{const}$, be a given measurable function. Denote by $L^{p(\cdot)}(\Omega)$ the set of all measurable functions $f(x)$ on $\Omega$ such that $\int_\Omega |f(x)|^{p(x)}\,dx < \infty$. Then $L^{p(\cdot)}(\Omega)$ is a reflexive separable Banach space with respect to the Luxemburg norm

$$\|f\|_{L^{p(\cdot)}(\Omega)} = \inf\left\{\lambda > 0 \ : \ \int_\Omega \left|\frac{f(x)}{\lambda}\right|^{p(x)} dx \le 1\right\}.$$

Moreover, in this case the set $C_0^\infty(\Omega)$ is dense in $L^{p(\cdot)}(\Omega)$. The relation between the modular $\int_\Omega |f(x)|^{p(x)}\,dx$ and the norm follows from the definition

$$\min\left\{\|f\|^{p^-}_{L^{p(\cdot)}(\Omega)}, \|f\|^{p^+}_{L^{p(\cdot)}(\Omega)}\right\} \le \int_\Omega |f(x)|^{p(x)}\,dx \le \max\left\{\|f\|^{p^-}_{L^{p(\cdot)}(\Omega)}, \|f\|^{p^+}_{L^{p(\cdot)}(\Omega)}\right\}. \tag{3.6}$$

If $p(\cdot) = \text{const} > 1$ then these inequalities transform into equalities. The following estimates are also well-known (see, for instance, [289, 290]): if $f \in L^{p(\cdot)}(\Omega)$ then

$$\|f\|_{L^{p^-}(\Omega)} \le (1 + |\Omega|)^{1/p^-}\,\|f\|_{L^{p(\cdot)}(\Omega)}, \tag{3.7}$$

$$\|f\|_{L^{p(\cdot)}(\Omega)} \le (1 + |\Omega|)^{1/(p^+)'}\,\|f\|_{L^{p^+}(\Omega)}, \quad (p^+)' = \frac{p^+}{p^+ - 1}, \quad \forall\, f \in L^{p^+}(\Omega), \tag{3.8}$$

$$\|f\|^{p^-}_{L^{p(\cdot)}(\Omega)} - 1 \le \int_\Omega |f(x)|^{p(x)}\,dx \le \|f\|^{p^+}_{L^{p(\cdot)}(\Omega)} + 1, \quad \forall\, f \in L^{p(\cdot)}(\Omega). \tag{3.9}$$

The next result can be viewed as an analogous of the Hölder inequality in Lebesgue spaces with variable exponents: If $f \in L^{p(\cdot)}(\Omega)$ and $g \in L^{p'(\cdot)}(\Omega)$ with

$$p(x) \in [p^-, p^+] \subset (1, +\infty), \quad p'(x) = \frac{p(x)}{p(x) - 1},$$

then $(f, g) \in L^1(\Omega)$ and

$$\int_\Omega (f, g)\,dx \le \left(\frac{1}{p^-} + \frac{1}{(p')^-}\right)\|f\|_{L^{p(\cdot)}(\Omega)}\|g\|_{L^{p'(\cdot)}(\Omega)} \le 2\|f\|_{L^{p(\cdot)}(\Omega)}\|g\|_{L^{p'(\cdot)}(\Omega)}. \tag{3.10}$$

Let $p_1(\cdot)$ and $p_2(\cdot)$ be measurable on $\Omega$ functions such that $p_i(x) \in [p_i^-, p_i^+] \subset (1, +\infty)$ a.e. in $\Omega$. In case $p_1(x) \ge p_2(x)$ a.e. in $\Omega$, the inclusion $L^{p_1(\cdot)}(\Omega) \subset L^{p_2(\cdot)}(\Omega)$ is continuous and

$$\|u\|_{L^{p_2(\cdot)}(\Omega)} \le C\|u\|_{L^{p_1(\cdot)}(\Omega)}, \quad \forall\, u \in L^{p_1(\cdot)}(\Omega) \tag{3.11}$$

with a constant $C = C(|\Omega|, p_1^{\pm}, p_2^{\pm})$.

The variable Sobolev space $W^{1,p(\cdot)}(\Omega)$ is defined as the set of functions

$$W^{1,p(\cdot)}(\Omega) := \left\{ u \in W^{1,1}(\Omega) \cap L^{p(\cdot)}(\Omega) \ : \ |\nabla u(x)|^{p(x)} \in L^1(\Omega) \right\}$$

equipped with the norm

$$\|u\|_{W^{1,p(\cdot)}(\Omega)} = \|u\|_{L^{p(\cdot)}(\Omega)} + \|\nabla u\|_{L^{p(\cdot)}(\Omega;\mathbb{R}^N)}. \tag{3.12}$$

Unlike classical Sobolev spaces, smooth functions are not necessarily dense in $W^{1,p(\cdot)}(\Omega)$. Therefore, we define $H^{1,p(\cdot)}(\Omega)$ as the closure of the set $C^{\infty}(\overline{\Omega})$ in $W^{1,p(\cdot)}(\Omega)$-norm.

Let $C^{log}(\overline{\Omega})$ be the set of functions continuous on $\overline{\Omega}$ with the logarithmic modulus of continuity, i.e.

$$|p(x_1) - p(x_2)| \leq \omega(|x_1 - x_2|), \tag{3.13}$$

where $\omega \geq 0$ satisfies the condition: $\limsup_{\tau \to 0^+} \omega(\tau) \log \dfrac{1}{\tau} = C < +\infty$, $C = \text{const}$. It is well-known that for $p \in C^{log}(\overline{\Omega})$ the set $C^{\infty}(\overline{\Omega})$ is dense in $W^{1,p(\cdot)}(\Omega)$ and the space $W^{1,p(\cdot)}(\Omega)$ coincides with the closure of $C^{\infty}(\overline{\Omega})$ with respect to the norm (3.12), i.e. in this case $W^{1,p(\cdot)}(\Omega) = H^{1,p(\cdot)}(\Omega)$. In particular, if there exists $\delta \in (0,1]$ such that $p \in C^{0,\delta}(\overline{\Omega})$, then the set $C^{\infty}(\overline{\Omega})$ is dense in $W^{1,p(\cdot)}(\Omega)$. Indeed, since

$$\lim_{t \to 0} |t|^{\delta} \log(\frac{1}{|t|}) = 0 \quad \textit{with } \delta \in (0,1],$$

it follows from the Hölder continuity of $p(\cdot)$ that

$$\begin{aligned} |p(x) - p(y)| \leq C|x-y|^{\delta} &\leq \omega(|x-y|) \sup_{x,y \in \Omega} \left[ |x-y|^{\delta} \log(|x-y|^{-1}) \right] \\ &\leq C' \omega(|x-y|), \quad \forall\, x, y \in \Omega, \end{aligned}$$

with $\omega(t) = C/\log(|t|^{-1})$.

Let $p(\cdot), q(\cdot) \in C(\overline{\Omega})$ be such that $p(x) \in [p^-, p^+] \subset (1,2]$ and $q(x) < \frac{2p(x)}{2-p(x)}$ in $\overline{\Omega}$. Then the embedding $W^{1,p(\cdot)}(\Omega) \subset L^{q(\cdot)}(\Omega)$ is continuous and compact. Moreover, according to (3.11), we have a continuous embedding $W^{1,p(\cdot)}(\Omega) \subset W^{1,p^-}(\Omega)$.

For a more detailed presentation of the theory of these spaces, we refer to the monograph [289].

### 3.2.3 On the dual Sobolev space $H^{-1}(\Omega)$

Let $H_0^1(\Omega)$ be the standard Sobolev space, i.e. $H_0^1(\Omega)$ is the closure of $C_0^1(\Omega)$ with respect to the norm

$$\|u\|_{H_0^1(\Omega)} = \left( \int_{\Omega} |\nabla u(x)|^2 \, dx \right)^{\frac{1}{2}}.$$

It is well-known that for any $u^* \in H^{-1}(\Omega)$ there can be found a vector-function $g = [g_1, g_2]$ in $L^2(\Omega; \mathbb{R}^2)$ such that

$$\langle u^*, u \rangle_{H^{-1}(\Omega); H_0^1(\Omega)} = \int_\Omega (g, \nabla u)_{\mathbb{R}^2} \, dx = \int_\Omega \left[ g_1 \frac{\partial u}{\partial x_1} + g_2 \frac{\partial u}{\partial x_2} \right] dx.$$

Therefore, it is clear now that

$$\|u^*\|_{H^{-1}(\Omega)} \le \sqrt{\int_\Omega (g_1^2(x) + g_2^2(x)) \, dx}. \tag{3.14}$$

On the other hand, due to the Lax-Milgram Theorem, the Dirichlet boundary value problem

$$-\Delta y = u^* \ \text{ in } \ \Omega, \qquad y = 0 \ \text{ on } \ \partial\Omega, \tag{3.15}$$

has a unique solution $y = (-\Delta)^{-1} u^* \in H_0^1(\Omega)$ for each $u^* \in H^{-1}(\Omega)$. Moreover, in view of the energy equality

$$\int_\Omega (\nabla y, \nabla y)_{\mathbb{R}^2} \, dx = \|\nabla y\|^2_{L^2(\Omega;\mathbb{R}^2)} = \|y\|^2_{H_0^1(\Omega)} = \langle u^*, y \rangle_{H^{-1}(\Omega); H_0^1(\Omega)}, \tag{3.16}$$

which holds for the weak solution of Dirichlet problems (3.15), we can deduce the following a priori estimate for the weak solution of Dirichlet problem (3.15)

$$\|y\|_{H_0^1(\Omega)} \equiv \|(-\Delta)^{-1} u^*\|_{H_0^1(\Omega)} \equiv \|\nabla(-\Delta)^{-1} u^*\|_{L^2(\Omega;\mathbb{R}^2)} \le \|u^*\|_{H^{-1}(\Omega)}.$$

Combining this result with (3.14), we get

$$\begin{aligned} \|\nabla(-\Delta)^{-1} u^*\|_{L^2(\Omega;\mathbb{R}^2)} \le \|u^*\|_{H^{-1}(\Omega)} \le \sqrt{\int_\Omega (g_1^2(x) + g_2^2(x)) \, dx} \\ \overset{\text{by (3.16)}}{=} \sqrt{\int_\Omega |\nabla y|^2_{\mathbb{R}^2} \, dx} = \|\nabla y\|_{L^2(\Omega;\mathbb{R}^2)} = \|y\|_{H_0^1(\Omega)} = \|\nabla(-\Delta)^{-1} u^*\|_{L^2(\Omega;\mathbb{R}^2)}. \end{aligned} \tag{3.17}$$

Hence, the norm in $H^{-1}(\Omega)$ can be defined as follows

$$\|u^*\|_{H^{-1}(\Omega)} = \|\nabla(-\Delta)^{-1} u^*\|_{L^2(\Omega;\mathbb{R}^2)}. \tag{3.18}$$

### 3.2.4 Level sets, directional gradients, and texture indexes

Let $u : \Omega \to \overline{\mathbb{R}}$ be a given function. Then for each $\lambda \in \mathbb{R}$ we can define the upper level set of $u$ as follows

$$Z_\lambda(u) = \{u \ge \lambda\} := \{x \in \Omega \ : \ u(x) \ge \lambda\}.$$

To describe this set, we assume that $u \in W^{1,1}(\Omega)$. It was proven in [291] that if $u \in W^{1,1}(\Omega)$ then its upper level sets $Z_\lambda(u)$ are sets of finite perimeter. So, the boundaries of level sets can be described by a countable family of Jordan curves with finite length, i.e., by continuous maps from the circle into the plane $\mathbb{R}^2$ without crossing points. As a result, at almost all points of almost all level sets of $u \in W^{1,1}(\Omega)$ we may define a unit normal vector $\theta(x)$. This vector field formally satisfies the following relations

$$(\theta, \nabla u) = |\nabla u| \quad \text{and} \quad |\theta| \leq 1 \text{ a.e. in } \Omega.$$

In the sequel, we will refer to $\theta$ as the vector field of unit normals to the topographic map of a function $u$.

If $\theta \in L^\infty(\Omega, \mathbb{R}^2)$ is a vector field of unit normals to the topographic map of some function $u(\cdot)$, then for any function $v \in W^{1,1}(\Omega)$ we can define the so-called directional gradient of $v$ following the rule (see [218, 219])

$$R_\eta \nabla v := \nabla v - \eta^2 \, (\theta, \nabla v) \, \theta, \tag{3.19}$$

where $\eta \in (0, 1)$ is a given threshold. Since, for each function $v \in W^{1,1}(\Omega)$, the expression $R_\eta \nabla v$ can be reduced to $(1 - \eta^2)\nabla v$ in those places of $\Omega$ where $\nabla v$ is collinear to the unit normal $\theta$, and to $\nabla v$ if $\nabla v$ is orthogonal to $\theta$, we have the following estimate

$$(1 - \eta^2)|\nabla v| \leq |R_\eta \nabla v| \leq |\nabla v| \quad \text{in } \Omega. \tag{3.20}$$

In what follows, with each function $u \in W^{1,1}(\Omega)$, we associate the so-called texture index $p(|\nabla u|)$ using the rule (see [292, 293, 294] for comparison)

$$p(s) = 1 + \delta + \frac{a^2(1 - \delta)}{a^2 + s^2}, \quad \forall \, s \in [0, +\infty), \tag{3.21}$$

where $0 < \delta \ll 1$ is a given threshold. It is clear now that

$$p(|\nabla u|) \in [p^-, p^+] \subset (1, 2] \text{ almost everywhere in } \Omega \text{ with } p^- = 1 + \delta \text{ and } p^+ = 2 \tag{3.22}$$

for each $u \in W^{1,1}(\Omega)$.

## 3.3 Statement of the problem

In this section, we present a novel variational problem for the denoising and contrast enhancement of non-smooth RGB images which can be viewed as an improved version of the variational model recently proposed in [287].

Let $f = [f_1, f_2, f_3]^t \in L^2(\Omega; \mathbb{R}^3)$ be an original color image. Let $\theta = \theta(f_i) = \begin{bmatrix} \theta_1 \\ \theta_2 \end{bmatrix} \in L^\infty(\Omega, \mathbb{R}^2)$ be a vector field of unit normals to the topographic map of the spectral channel $f_i$,

$$|\theta(x)| \leq 1 \quad \text{and} \quad (\theta(x), \nabla f_i(x)) = |\nabla f_i(x)| \quad \text{a.e. in } \Omega. \tag{3.23}$$

This vector field can be defined by the rule $\theta(x) = \frac{\nabla U(t,x)}{|\nabla U(t,x)|}$ with $t > 0$ small enough, where $U(t, x)$ is a solution of the following initial-boundary value problem

$$\frac{\partial U}{\partial t} = \operatorname{div}\left(\frac{\nabla U}{|\nabla U| + \kappa}\right), \quad t \in (0, +\infty),\ x \in \Omega, \tag{3.24}$$

$$U(0, x) = f_i(x), \quad x \in \Omega, \tag{3.25}$$

$$\frac{\partial U(t,x)}{\partial \nu} = 0, \quad t \in (0, +\infty),\ x \in \partial\Omega \tag{3.26}$$

with a relaxed version of the $1D$-Laplace operator in the principle part of (3.24). Here, $\kappa > 0$ is a sufficiently small positive value.

Let $\eta \in (0, 1)$ be a given threshold. Taking into account the definition of the Directional Total Variation (see [218]), we define the linear operator $R_\eta : \mathbb{R}^2 \to \mathbb{R}^2$ as follows

$$R_\eta \nabla v := \nabla v - \eta^2 (\theta, \nabla v)\, \theta, \quad \forall\, v \in W^{1,1}(\Omega). \tag{3.27}$$

Since $R_\eta \nabla v$ reduces to $(1 - \eta^2)\nabla v$ in those regions where the gradient $\nabla v$ is co-linear to $\theta$, and to $\nabla v$, where $\nabla v$ is orthogonal to $\theta$, this operator does not enforce gradients in the direction $\theta$.

**Remark 3.3.1.** *In the sequel, to reduce the number of parameters in the proposed model, we will set $\delta = \kappa$ in* (3.24) *and* (3.21)*, and $\eta = 1 - \kappa$ in* (3.19)*.*

We also introduce the following set

$$\Xi_i = \left\{ I \in H^{1,p(|\nabla I|)}(\Omega) \cap L^\infty(\Omega) \;\middle|\; \begin{array}{c} \gamma_{i,0} \leq I(x) \leq \gamma_{i,1} \quad \text{a.e. in } \Omega, \\ \gamma_{i,0} = \inf_{x\in\Omega} f_i(x), \\ \gamma_{i,1} = \sup_{x\in\Omega} f_i(x), \end{array} \right\} \tag{3.28}$$

where $p(\cdot)$ is given by (3.21), and $H^{1,p(|\nabla I|)}(\Omega)$ is the variable Sobolev space that can be defined as follows

$$H^{1,p(|\nabla I|)}(\Omega) := \mathrm{cl}_{\|\cdot\|_{W^{1,p(|\nabla I|)}(\Omega)}} C_0^\infty(\mathbb{R}^2). \tag{3.29}$$

Further, for a given gray-scale image $I \in L^2(\Omega)$, we define its average local contrast measure $D(I)$ as follows (for comparison, we refer to [276])

$$D(I) = \int_\Omega \int_\Omega W(x, y) \sqrt{\kappa^2 + |I(x) - I(y)|^2}\, dxdy, \tag{3.30}$$

where $\kappa > 0$ is the same parameter as in (3.24), and $W \in L^2(\Omega \times \Omega)$ is a symmetric non-negative kernel such that

$$\int_\Omega W(x,y)\,dx = 1, \quad \forall\, y \in \Omega.$$

A typical example of this function is the Gaussian kernel,

$$W(x,y) = \frac{1}{\sqrt{2\pi}\sigma} \exp\left(-\frac{|x-y|^2}{2\sigma^2}\right), \quad \sigma > 0.$$

As a result, the proposed variational approach for the contrast enhancement and denoising of color images can be stated as follows:

> For each spectral channel $f_i$, $(i = 1,2,3)$, of a given image $f = [f_1, f_2, f_3]^t \in L^2(\Omega;\mathbb{R}^3)$, we generate a new one $f_i^0 \in L^2(\Omega)$ as a solution of the following constrained minimization problem
>
> $$J_i(f_i^0) = \inf_{v \in \Xi_i} J_i(v), \tag{3.31}$$
>
> where
>
> $$J_i(v) = \int_\Omega |R_\eta \nabla v(x)|^{p(|\nabla v|)}\,dx + \frac{\mu}{2}\,\|v - f_i\|^2_{H^{-1}(\Omega)} + \frac{\lambda}{4}\left[D(v) - cD(f_i)\right]^2. \tag{3.32}$$
>
> Here, $\lambda > 0$ and $\mu \in (0,1)$ are tuning parameters. The parameter $\lambda$ manages the trade-off between the fidelity term $\frac{\mu}{2}\,\|v - f_i\|^2_{H^{-1}(\Omega)}$ and the contrast term $\frac{\lambda}{4}\left[D(v) - cD(f_i)\right]^2$. As for the multiplier $c > 0$, we always suppose that $c > 1$ and it provides a control of the contrast level expected for the result.

Before proceeding further, we provide some qualitative analysis of the variational problem (3.31)-(3.32). To begin with, we notice that, for each feasible solution $v \in \Xi$, the following two-sides estimate

$$p^+ = 2 \geq p(|\nabla v|) > 1 + \delta =: p^-, \quad \text{for a.a. } x \in \Omega \tag{3.33}$$

holds with $0 < \delta \ll 1$. Moreover, since $\eta \in (0,1)$ and $\eta \gg 0$, we see that

$$(1-\eta^2)|\nabla v| \leq |R_\eta \nabla v| \leq |\nabla v| \quad \text{in } \Omega, \tag{3.34}$$

$$\begin{aligned}\int_\Omega |R_\eta \nabla v(x)|^{p(|\nabla v|)}\,dx &\geq \int_\Omega (1-\eta^2)^{p(|\nabla v|)} |\nabla v(x)|^{p(|\nabla v|)}\,dx \\ &\geq (1-\eta^2)^2 \int_\Omega |\nabla v(x)|^{p(|\nabla v|)}\,dx, \quad \forall\, v \in W^{1,p(|\nabla v|)}(\Omega).\end{aligned} \tag{3.35}$$

As a result, $\forall\, v \in \Xi_i$, we have

$$\begin{aligned}
\|v\|^{p^-}_{W^{1,p(|\nabla v|)}(\Omega)} &= \left(\|v\|_{L^{p(|\nabla v|)}(\Omega)} + \|\nabla v\|_{L^{p(|\nabla v|)}(\Omega;\mathbb{R}^2)}\right)^{p^-} \\
&\le C\left(\|v\|^{p^-}_{L^{p(|\nabla v|)}(\Omega)} + \|\nabla v\|^{p^-}_{L^{p(|\nabla v|)}(\Omega;\mathbb{R}^2)}\right) \\
&\overset{\text{by (3.9)}}{\le} C\left(\int_\Omega |v(x)|^{p(|\nabla v|)}\,dx + \int_\Omega |\nabla v(x)|^{p(|\nabla v|)}\,dx + 2\right) \\
&\le C\left(|\Omega|\gamma_{i,1}^2 + \int_\Omega |\nabla v(x)|^{p(|\nabla v|)}\,dx + 2\right) \\
&\overset{\text{by (3.35)}}{\le} C\left(|\Omega|\gamma_{i,1}^2 + 2 + \frac{1}{(1-\eta^2)^2}\int_\Omega |R_\eta \nabla v(x)|^{p(|\nabla v|)}\,dx\right) \\
&\le C\left(|\Omega|\gamma_{i,1}^2 + 2 + \frac{1}{(1-\eta^2)^2} J_i(v)\right). \qquad (3.36)
\end{aligned}$$

Thus, the first term in the cost functional (3.32) can be considered as a regularizing term. As for the second term in (3.32), we make use of the following observation.

**Remark 3.3.2.** *The model* (3.32) *is aimed not only at the contrast enhancement, but also to remove the additive noise in the so-called structured images, i.e. in images where the portion of high oscillatory edges is rather significant. In most cases, the satellite images with crop fields typically contain many high oscillatory edges (boundaries of the crop locations). Moreover, the portion of noise in such images can be different from channel to channel. Because of this, an important question is to separate pure noise from high oscillatory edges in each spectral channel. To handle this problem, Y. Meyer [295] suggested to replace the standard $L^2$-fidelity term $\frac{\mu}{2}\|v - f_i\|^2_{L^2(\Omega)}$, which is a typical component in the standard denoising models, by a weaker norm. As a plausible option of such weakening, Lieu and Vese [296] (see also Schönlieb [297]) have proposed to involve $H^{-1}(\Omega)$-norm instead of $\|\cdot\|_{L^2(\Omega)}$. Thus, from this point of view, it is plausible to interpret the second term in* (3.32) *as the fidelity term.*

Before we move on to the existence issues, we make use of the following result concerning the lower semicontinuity property of the modular $\int_\Omega |f(x)|^{p(x)}\,dx$ with respect to the weak convergence in $L^{p_k(\cdot)}(\Omega)$. The proof of this assertion has been mainly inspired by the elegant proof of Lemma 1 in [298] (see also [299, Lemma 13.3] for comparison).

**Proposition 3.3.1.** *Let $\{p_k\}_{k\in\mathbb{N}} \subset [p^-, p^+]$ be a given sequence such that*

$$p_k(x) \to p(x) \quad \text{almost everywhere in } \Omega \text{ as } k \to \infty. \qquad (3.37)$$

*Let* $\left\{v_k \in W^{1,p_k(\cdot)}(\Omega)\right\}_{k\in\mathbb{N}}$ *be a sequence such that*

$$\nabla v_k \rightharpoonup \nabla v \quad \text{weakly in } L^1(\Omega;\mathbb{R}^2), \tag{3.38}$$

$$\left\||\nabla v_k(\cdot)|^{p_k(\cdot)}\right\|_{L^1(\Omega)} \le C \quad \text{for some positive constant } C \text{ not depending on } k, \tag{3.39}$$

*and let* $R_\eta : \mathbb{R}^2 \to \mathbb{R}^2$ *be the operator defined in* (3.27) *with some* $\theta \in L^\infty(\Omega,\mathbb{R}^2)$. *Then* $\nabla v \in L^{p(\cdot)}(\Omega;;\mathbb{R}^2)$ *and*

$$\liminf_{k\to\infty} \int_\Omega |R_\eta \nabla v_k(x)|^{p_k(x)}\,dx \ge \int_\Omega |R_\eta \nabla v(x)|^{p(x)}\,dx. \tag{3.40}$$

*Proof.* By Young's inequality we have for $\xi,\zeta \in \mathbb{R}^2$ and $1 < p < \infty$,

$$(\xi,\zeta) \le |\xi||\zeta| \le |\xi|^p + \frac{|\zeta|^{p'}}{p' p^{p'/p}}, \quad \frac{1}{p} + \frac{1}{p'} = 1. \tag{3.41}$$

If now $\zeta$ is a function in $L^\infty(\Omega;\mathbb{R}^2)$ and we make $p = p_k$ in (3.41) and use the assumption $p^- \le p_k(x) \le p^+$ for all $k \in \mathbb{N}$, then we derive

$$\int_\Omega \left( (R_\eta \nabla v_k, \zeta) - \frac{|\zeta|^{p_k'(x)}}{p_k'(x) p_k(x)^{p_k'(x)/p_k(x)}} \right) dx \le \int_\Omega |R_\eta \nabla v_k|^{p_k(x)}\,dx. \tag{3.42}$$

Using (3.27) and assumptions (3.37) and (3.38), we can pass to the limit in (3.42) as $k \to \infty$. As a result, we have

$$\int_\Omega \left( (R_\eta \nabla v, \zeta) - \frac{|\zeta|^{p'(x)}}{p'(x) p(x)^{p'(x)/p(x)}} \right) dx \le \liminf_{k\to\infty} \int_\Omega |R_\eta \nabla v_k|^{p_k(x)}\,dx := L. \tag{3.43}$$

Then we consider the following function:

$$\zeta := \frac{R_\eta \nabla v}{|R_\eta \nabla v|} p(x) |R_\eta \nabla v|_n^{\frac{1}{p'(x)-1}}, \quad \text{with } |R_\eta \nabla v|_n := \max\left\{|R_\eta \nabla v|, n\right\}, \quad n > 0.$$

Inserting this function $\zeta$ into (3.43), we get

$$\int_\Omega \left( |R_\eta \nabla v| p(x) |R_\eta \nabla v|_n^{\frac{1}{p'(x)-1}} - |R_\eta \nabla v|_n^{\frac{p'(x)}{p'(x)-1}} \frac{p(x)}{p'(x)} \right) dx \le L.$$

This implies

$$\int_\Omega |R_\eta \nabla v|_n^{\frac{1}{p'(x)-1}+1}\,dx \le L.$$

Since $\frac{1}{p'(x)-1}+1=p(x)$, it follows that

$$\int_\Omega |R_\eta \nabla v|_n^{p(x)}\,dx \le L. \tag{3.44}$$

To conclude the proof, it remains to notice that the announced inequality (3.40) follows by letting $n\to\infty$ in (3.44). As for the inclusion $\nabla v\in L^{p(\cdot)}(\Omega;\mathbb{R}^2)$ it is a direct consequence of assumption (3.39) and estimate (3.34). □

Before proceeding to the existence issues, we provide, in the next section, a formal analysis of the optimality system for the problem (3.31)–(3.32).

## 3.4 Optimality conditions

Let $f_i^0\in\Xi_i$, with $i=1,2,3$, be a point of local minimum in the problem (3.31)–(3.32), i.e., there exists a positive value $\tau>0$ such that

$$J_i(f_i^0)-J_i(v)\le 0,\quad \forall\, v\in\Xi \ \text{ s.t. } \ \|v-f_i^0\|_{W^{1,p^-}(\Omega)}<\tau. \tag{3.45}$$

For simplicity, we assume that the two-side inequality

$$\gamma_{i,1}<f_i^0(x)<\gamma_{i,2}$$

holds almost everywhere in $\Omega$. Then condition (3.45) can be rewritten as follows: for any smooth function $\varphi\in C^\infty(\overline{\Omega})$, the inequality

$$J_i(f_i^0)-J_i(f_i^0+\sigma\varphi)\le 0 \quad \text{for } \sigma \text{ small enough} \tag{3.46}$$

holds. Hence, the scalar function

$$\begin{aligned}\psi(\sigma):=J_i(f_i^0+\sigma\varphi)=&\int_\Omega |R_\eta\left(\nabla f_i^0(x)+\sigma\nabla\varphi(x)\right)|^{p(|\nabla f_i^0+\sigma\nabla\varphi|)}\,dx\\ &+\frac{\mu}{2}\left\|f_i^0+\sigma\varphi-f_i\right\|^2_{H^{-1}(\Omega)}+\frac{\lambda}{4}\left[D(f_i^0+\sigma\varphi)-cD(f_i)\right]^2\end{aligned}$$

has a minimum at $\sigma=0$.

Thus, to characterize the given feasible solution $f_i^0\in\Xi_i$ to optimization problem (3.31)–(3.32), we make use of the Ferma's Theorem. To do so, we show that the objective functional $J_i(v)$ is Gâteaux differentiable at $v=f_i^0$, that is, there exists a linear bounded functional $D_GJ_i(f_i^0)\in\left[H^{1,p[\nabla f_i^0]}(\Omega)\right]'=\mathcal{L}\left(H^{1,p[\nabla f_i^0]}(\Omega),\mathbb{R}\right)$ such that

$$J_i\left(f_i^0+\sigma h\right)=J_i\left(f_i^0\right)+\sigma D_GJ_i(f_i^0)[h]+r_i(h,\sigma),\quad \forall\, h\in H^{1,p[\nabla f_i^0]}(\Omega), \tag{3.47}$$

where $|r_i(h,\sigma)| = o(|\sigma|)$ as $\sigma \to 0$. Then the condition $0 \in \operatorname{Argmin} \psi(\sigma)$ can be interpreted as

$$D_G J_i(f_i^0)[\varphi] = 0, \quad \forall\, \varphi \in C^\infty(\overline{\Omega}). \tag{3.48}$$

Keeping in mind the fact that the set of feasible solutions $\Xi_i$ to the problem (3.31)–(3.32) has an empty topological interior, we begin with the following auxiliary results, where $F'(u)[h]$ stands for the directional derivative of a functional $F : X \to \mathbb{R}$ at the point $u \in X$ along a vector $h \in X$, i.e.,

$$F'(u)[h] = \lim_{\sigma \to 0} \frac{F(u+\sigma h) - F(u)}{\sigma}.$$

**Proposition 3.4.1.** *Let $f \in L^2(\Omega)$ be a given distribution and let*

$$F_1(u) = \frac{1}{2}\|u - f\|^2_{H^{-1}(\Omega)}, \quad \forall\, u \in L^2(\Omega).$$

*Then*

$$F_1'(u)[h] = \left((-\Delta)^{-1}(u-f), h\right)_{L^2(\Omega)}, \quad \forall\, h \in L^2(\Omega). \tag{3.49}$$

*Proof.* The announced result immediately follows from the definition of the directional derivative and the following chain of transformations

$$\begin{aligned}
F_1(u+\sigma h) - F_1(u) &\overset{\text{by (3.18)}}{=} \frac{1}{2}\|\nabla(-\Delta)^{-1}(u+\sigma h - f)\|_{L^2(\Omega;\mathbb{R}^2)} \\
&\quad - \frac{1}{2}\|\nabla(-\Delta)^{-1}(u-f)\|_{L^2(\Omega;\mathbb{R}^2)} \\
&= \sigma\left(\nabla(-\Delta)^{-1}(u-f), \nabla(-\Delta)^{-1}h\right)_{L^2(\Omega;\mathbb{R}^2)} + \sigma^2\frac{1}{2}\|\nabla(-\Delta)^{-1}h\|^2_{L^2(\Omega;\mathbb{R}^2)} \\
&= -\sigma\int_\Omega \operatorname{div}\left[\nabla(-\Delta)^{-1}(u-f)\right](-\Delta)^{-1}h\,dx + \sigma^2\frac{1}{2}\|h\|^2_{H^{-1}(\Omega)} \\
&= \sigma\int_\Omega (-\Delta)(-\Delta)^{-1}(u-f)(-\Delta)^{-1}h\,dx + \sigma^2\frac{1}{2}\|h\|^2_{H^{-1}(\Omega)} \\
&= \sigma\left((-\Delta)^{-1}(u-f), h\right)_{L^2(\Omega)} + o(\sigma), \quad \forall\, u \in L^2(\Omega).
\end{aligned}$$

□

**Proposition 3.4.2.** *Let $p : \Omega \to [p^-, p^+] \subset (1,2]$, with $p^\pm = \text{const}$, be a given exponent and let*

$$\widetilde{F}_2(u) = \int_\Omega |\nabla u(x)|^{p(x)}\,dx, \quad \forall\, u \in W^{1,p(\cdot)}(\Omega).$$

*Then, for each $u \in W^{1,p(\cdot)}(\Omega)$, we have*

$$\widetilde{F}_2'(u)[h] = \int_\Omega p(x)\left(|\nabla u(x)|^{p(x)-2}\nabla u(x), \nabla v(x)\right)\,dx, \quad \forall\, h \in W^{1,p(\cdot)}(\Omega). \tag{3.50}$$

*Proof.* Let $u, h \in W^{1,p(\cdot)}(\Omega)$ be given functions. We notice that

$$\frac{|\nabla u + \sigma \nabla h|^p - |\nabla u|^p}{\sigma} \to p\left(|\nabla u|^{p-2}\nabla u, \nabla h\right)$$

as $\sigma \to 0$ almost everywhere in $\Omega$. Furthermore, by convexity,

$$|\xi|^p - |\eta|^p \le 2p\left(|\xi|^{p-1} + |\eta|^{p-1}\right)|\xi - \eta|,$$

we have

$$\begin{aligned}\Big|\frac{1}{\sigma}\Big(|\nabla u(x) + \sigma\nabla h(x)|^{p(x)} - |\nabla u(x)|^{p(x)}\Big)\Big| \\ &\le 2p(x)\left(|\nabla u(x) + \sigma\nabla h(x)|^{p(x)-1} + |\nabla u(x)|^{p(x)-1}\right)|\nabla h(x)| \\ &\le \text{const}\,\left(|\nabla u(x)|^{p(x)-1} + |\nabla h(x)|^{p(x)-1}\right)|\nabla h(x)|. \qquad (3.51)\end{aligned}$$

Taking into account that

$$\begin{aligned}\int_\Omega |\nabla u(x)|^{p(x)-1}|\nabla v(x)|\,dx &\le 2\||\nabla u(x)|^{p(x)-1}\|_{L^{p'(\cdot)}(\Omega)}\||\nabla h(x)|\|_{L^{p(\cdot)}(\Omega)} \\ &\le 2\||\nabla u(x)|^{p(x)-1}\|_{L^{p'(\cdot)}(\Omega}\|\nabla h(x)\|_{L^{p(\cdot)}(\Omega,\mathbb{R}^2)},\end{aligned}$$

and

$$\int_\Omega |\nabla h(x)|^{p(x)}\,dx \overset{by\ (3.9)}{\le} \|\nabla h\|^2_{L^{p(\cdot)}(\Omega,\mathbb{R}^2)} + 1,$$

we see that the right hand side of inequality (3.51) is an $L^1(\Omega)$-function. Therefore,

$$\begin{aligned}\lim_{\sigma\to 0}\frac{\widetilde{F}_2(u+\sigma h) - \widetilde{F}_2(u)}{\sigma} &= \lim_{\sigma\to 0}\int_\Omega \frac{|\nabla u(x) + \sigma\nabla h(x)|^p - |\nabla u(x)|^p}{\sigma}\,dx \\ &= \int_\Omega p(x)\left(|\nabla u(x)|^{p(x)-2}\nabla u(x), \nabla h(x)\right)\,dx\end{aligned}$$

by the Lebesgue-dominated convergence theorem. From this, the representation (3.50) follows. □

**Proposition 3.4.3.** *Let $p : \Omega \to [p^-, p^+] \subset (1, 2]$, with $p^\pm = \text{const}$, be a given exponent and let*

$$F_2(u) = \int_\Omega |R_\eta \nabla u(x)|^{p(x)}\,dx, \quad \forall\, u \in W^{1,p(\cdot)}(\Omega),$$

*where the linear operator $R_\eta : \mathbb{R}^2 \to \mathbb{R}^2$ is defined by the rule* (3.27)*. Then, for each $u \in W^{1,p(\cdot)}(\Omega)$, we have*

$$\begin{aligned}F_2'(u)[h] &= \int_\Omega p(x)\left(|R_\eta\nabla u(x)|^{p(x)-2}R_\eta\nabla u(x), \nabla h(x)\right)\,dx \\ -\eta^2\int_\Omega p(x)&\left(|R_\eta\nabla u(x)|^{p(x)-2}R_\eta\nabla u(x), \theta(x)\right)(\theta(x), \nabla h(x))\,dx, \quad \forall\, h \in W^{1,p(\cdot)}(\Omega).\end{aligned} \qquad (3.52)$$

*Proof.* The representation (3.52) immediately follows from the definition of the directional derivative and Proposition 3.4.2. □

**Proposition 3.4.4.** *Let $u \in \Xi_i$ be a given feasible solution, let*

$$p[\nabla u] := 1 + \delta + \frac{a^2(1-\delta)}{a^2 + |\nabla u|^2},$$

*and let the functional $F_3 : W^{1,1+\delta}(\Omega) \to \mathbb{R}$ be defined as follows,*

$$F_3(u) = \int_\Omega |R_\eta \nabla v(x)|^{p[\nabla u]}\, dx, \quad \forall\, u \in W^{1,1+\delta}(\Omega),$$

*where $v \in W^{1,p[\nabla u]}(\Omega)$ is a given function. Then, for each $v \in W^{1,p[\nabla u]}(\Omega)$ and for all $h \in W^{1,1+\delta}(\Omega)$, we have*

$$F_3'(u)[h] = -\int_\Omega |R_\eta \nabla v(x)|^{p[\nabla u]} \frac{2a^2(1-\delta)\log\left(|R_\eta \nabla v(x)|\right)}{\left(a^2 + |\nabla u|^2\right)^2} \left(\nabla u, \nabla h\right)\, dx. \quad (3.53)$$

*Proof.* The representation (3.53) immediately follows from the definition of the directional derivative. □

**Proposition 3.4.5.** *Let $u \in \Xi$ be a feasible solution, and let*

$$F_4(u) = \frac{\lambda}{4}\left[D(u) - cD(f_i)\right]^2,$$

*where $f_i \in L^2(\Omega)$ is a given spectral channel, $c = \text{const} > 1$, and*

$$D(u) = \int_\Omega \int_\Omega W(x,y) \sqrt{\kappa^2 + |u(x) - u(y)|^2}\, dxdy.$$

*Then the directional derivative of $F_4 : L^2(\Omega) \to \mathbb{R}$ at the given point $u$ along a vector $h \in L^2(\Omega)$ takes the form*

$$F_4'(u)[h] = \lambda\left(D(u) - cD(I_f)\right) \int_\Omega \left( \int_\Omega W(x,y) \frac{u(x) - u(y)}{\sqrt{\kappa^2 + |u(x) - u(y)|^2}}\, dy \right) h(x)\, dx. \quad (3.54)$$

*Proof.* The representation (3.54) immediately follows from definition of the directional derivative and the following chain of transformations

$$
\begin{aligned}
&D(u+\sigma h)-D(u)\\
&=\int_\Omega\int_\Omega W(x,y)\left(\sqrt{\kappa^2+|u(x)-u(y)+\sigma(h(x)-h(y))|^2}-\sqrt{\kappa^2+|u(x)-u(y)|^2}\right)\,dxdy\\
&=\int_\Omega\int_\Omega W(x,y)\frac{|u(x)-u(y)+\sigma(h(x)-h(y))|^2-|u(x)-u(y)|^2}{\sqrt{\kappa^2+|u(x)-u(y)+\sigma(h(x)-h(y))|^2}+\sqrt{\kappa^2+|u(x)-u(y)|^2}}\,dxdy\\
&\quad=\sigma\int_\Omega\left(\int_\Omega\left[W(x,y)+W(y,x)\right]\frac{u(x)-u(y)}{\sqrt{\kappa^2+|u(x)-u(y)|^2}}\,dy\right)h(x)\,dy+o(\sigma^2).
\end{aligned}
$$

□

We are now able to show that the objective functional $J_i(v)$ is Gâteaux differentiable at $v=f_i^0$. With that in mind, we utilize the representation (3.32). As a result, we see that

$$
\begin{aligned}
J_i'(f_i^0)[\varphi]=&\int_\Omega p(|\nabla f_i^0|)\left(|R_\eta\nabla f_i^0(x)|^{p(|\nabla f_i^0|)-2}R_\eta\nabla f_i^0(x),\nabla\varphi(x)\right)\,dx\\
&-\eta^2\int_\Omega p(|\nabla f_i^0|)\left(|R_\eta\nabla f_i^0(x)|^{p(|\nabla f_i^0|)-2}R_\eta\nabla f_i^0(x),\theta(x)\right)(\theta(x),\nabla\varphi(x))\,dx\\
&-\int_\Omega|R_\eta\nabla f_i^0(x)|^{p(|\nabla f_i^0|)}\frac{2a^2(1-\delta)\log\left(|R_\eta\nabla f_i^0(x)|\right)}{\left(a^2+|\nabla f_i^0(x))|^2\right)^2}\left(\nabla f_i^0,\nabla\varphi\right)\,dx\\
&+\lambda\left(D(f_i^0)-cD(f_i)\right)\int_\Omega\left(\int_\Omega W(x,y)\frac{f_i^0(x)-f_i^0(y)}{\sqrt{\kappa^2+|f_i^0(x)-f_i^0(y)|^2}}\,dy\right)\varphi(x)\,dx\\
&+\int_\Omega\Big[(-\Delta)^{-1}(f_i^0-f_i)\Big]\varphi(x)\,dx=0,\quad\forall\,\varphi\in C^\infty(\overline{\Omega}).
\end{aligned}
\tag{3.55}
$$

Thus, $J_i'(f_i^0):C^\infty(\overline{\Omega})\to\mathbb{R}$ is a linear functional.

Let us show that each term in (3.55) can be extended by continuity to the entire Sobolev space $H^{1,p(|\nabla f_i^0|)}(\Omega)$. To this end, it is enough to establish the existence of a constant $M>0$ such that

$$
\left|J_i'(f_i^0)[\varphi]\right|\le M\|\varphi\|_{W^{1,p(|\nabla f_i^0|)}(\Omega)},\quad\forall\,\varphi\in C^\infty(\overline{\Omega}).
\tag{3.56}
$$

Indeed, rewriting (3.55) in the form

$$
J_i'(f_i^0)[\varphi]=S_1+S_2+S_3+S_4+S_5,
$$

where the one-to-one correspondence to (3.55) is preserved, we see that

$$\begin{aligned}|S_1| &\le \|p\|_{L^\infty(\Omega)} \int_\Omega \left(|R_\eta \nabla f_i^0|^{p(|\nabla f_i^0|)-2} R_\eta \nabla f_i^0, \nabla\varphi\right) dx \\ &\overset{\text{by (3.10)}}{\le} 2p^+ \||R_\eta \nabla f_i^0|^{p(|\nabla f_i^0|)-2} R_\eta \nabla f_i^0\|_{L^{p'(|\nabla f_i^0|)}(\Omega;\mathbb{R}^2)} \|\nabla\varphi\|_{L^{p(|\nabla I^0|)}(\Omega;\mathbb{R}^2)} \\ &\overset{\text{by (3.9)}}{\le} 2p^+ \left(1 + \int_\Omega |R_\eta \nabla f_i^0|^{p(|\nabla f_i^0|)}\, dx\right)^{1/(p')^-} \|\varphi\|_{W^{1,p(|\nabla f_i^0|)}(\Omega)},\end{aligned}$$

where $p^+ = 2$, $(p')^- = p^+/(p^+ - 1) = 2$, and

$$\int_\Omega |R_\eta \nabla f_i^0|^{p(|\nabla f_i^0|)}\, dx \overset{\text{by (3.9)}}{\le} 1 + \|\nabla f_i^0\|^{p^+}_{L^{p(|\nabla f_i^0|)}(\Omega;\mathbb{R}^2)} \le 1 + \|f_i^0\|^2_{W^{1,p(|\nabla f_i^0|)}(\Omega)} < +\infty$$

by the assumption $f_i^0 \in \Xi_i$. Thus, there exists a constant $M_1 > 0$ such that

$$|S_1| \le M_1 \|\varphi\|_{W^{1,p(|\nabla f_i^0|)}(\Omega)}. \tag{3.57}$$

Arguing similarly, it can be shown that a constant $M_2 > 0$ exists such that

$$|S_2| \le M_2 \|\varphi\|_{W^{1,p(|\nabla f_i^0|)}(\Omega)}. \tag{3.58}$$

As for the third term in (3.55), we notice that

$$|\nabla f_i^0|^2 \frac{|\log(|\nabla f_i^0|)|}{(a^2 + |\nabla f_i^0|^2)^2} \le \frac{|\log(|\nabla f_i^0|)|}{a^2 + |\nabla f_i^0|^2} < +\infty \quad \text{as } |\nabla f_i^0| \to \infty$$

by the L'Hôpital's rule. Using similar arguments, we see that

$$|\nabla f_i^0|^2 \frac{|\log(|\nabla f_i^0|)|}{(a^2 + |\nabla f_i^0|^2)^2} \le \frac{1}{a^4} |\nabla f_i^0|^2 |\log\left(|\nabla f_i^0|\right)| < +\infty \quad \text{as } |\nabla f_i^0| \to 0.$$

Thus, we can deduce the existence of a constant $M_2 > 0$ such that

$$\begin{aligned}|S_2| &\le 2a^2(1-\delta) \left\| |R_\eta \nabla f_i^0|^2 \frac{|\log(|R_\eta \nabla f_i^0|)|}{(a^2 + |\nabla f_i^0|^2)^2} \right\|_{L^\infty(\Omega)} \\ &\quad \times \int_\Omega \left(|R_\eta \nabla f_i^0|^{p(|\nabla f_i^0|)-2} R_\eta \nabla f_i^0, \nabla\varphi\right) dx \le M_3 \|\varphi\|_{W^{1,p(|\nabla f_i^0|)}(\Omega)}.\end{aligned} \tag{3.59}$$

It remains to notice that in view of the obvious inclusions

$$\int_\Omega W(\cdot, y) \frac{f_i^0(\cdot) - f_i^0(y)}{\sqrt{\kappa^2 + |f_i^0(\cdot) - f_i^0(y)|^2}}\, dy \in L^2(\Omega),$$
$$\left[(-\Delta)^{-1}(f_i^0 - f_i)\right] \in L^2(\Omega),$$

the existence of constants $M_3$ and $M_4$ such that

$$|S_j| \le M_j \|\varphi\|_{L^2(\Omega)} \le M_j \|\varphi\|_{W^{1,p(|\nabla f_i^0|)}(\Omega)}, \quad j = 4, 5, \tag{3.60}$$

immediately follows from (3.55) and the Cauchy inequality.

Utilizing the estimates (3.57), (3.59), and (3.60), we finally arrive at the inequality (3.56) with $M = \max\{M_1, M_2, M_3, M_4, M_5\}$. Thus, the mapping $\varphi \mapsto J_i'(f_i^0)[\varphi]$ can be defined for all $\varphi \in H^{1,p(|\nabla f_i^0|)}(\Omega)$ using the density of $C^\infty(\overline{\Omega})$ in $H^{1,p(|\nabla f_i^0|)}(\Omega)$ (see (3.29)) and the standard rule

$$D_G J_i(f_i^0)[\varphi] = \lim_{k\to\infty} D_G J_i(f_i^0)[\varphi_k],$$

where $\{\varphi_k\}_{k\in\mathbb{N}} \subset C_c^\infty(\mathbb{R}^2)$ and $\varphi_k \to \varphi$ strongly in $H^{1,p(|\nabla f_i^0|)}(\Omega)$. Hence, the objective functional $J_i(v)$ is Gâteaux differentiable at $v = f_i^0$, and

$$D_G J_i(f_i^0)[h] = J'(f_i^0)[h], \quad \forall\, h \in H^{1,p(|\nabla f_i^0|)}(\Omega).$$

To get the final relations for optimality conditions, it remains to observe that identity (3.55) implies the following equalities in the sense of distributions

$$\begin{aligned}
&-\operatorname{div}\left[p(x)|R_\eta \nabla f_i^0|^{p(|\nabla f_i^0|)-2} R_\eta \nabla f_i^0\right] \\
&+\eta^2 \operatorname{div}\left[p(x)\left(|R_\eta \nabla f_i^0|^{p(|\nabla f_i^0|)-2} R_\eta \nabla f_i^0, \theta\right)\theta\right] \\
&+2a^2(1-\delta)\operatorname{div}\left[|R_\eta \nabla f_i^0|^{p(|\nabla f_i^0|)} \frac{\log\left(|R_\eta \nabla f_i^0|\right)}{\left(a^2 + |\nabla f_i^0|^2\right)^2} \nabla f_i^0\right] \\
&+\lambda\left(D(f_i^0) - cD(f_i)\right)\int_\Omega W(x,y)\frac{f_i^0(x) - f_i^0(y)}{\sqrt{\kappa^2 + |f_i^0(x) - f_i^0(y)|^2}}\, dy \\
&+\mu(-\Delta)^{-1}(f_i^0 - f_i) = 0, \quad \text{in } \Omega
\end{aligned} \tag{3.61}$$

$$\left(|\nabla f_i^0|^{p(|\nabla f_i^0|)-2}\nabla f_i^0, \nu\right) = 0 \quad \text{on } \partial\Omega, \tag{3.62}$$

where $\nu$ denotes the unit outward normal to the boundary $\partial\Omega$.

## 3.5 Existence issues and regularization of the original optimization problem

The main question we are going to discuss in this section is to find out whether the problem (3.31)–(3.32) admits at least one solution. With that in mind, we make use of the so-called indirect approach [300, 301]. The main idea of this approach

is to show that the original minimization problem (3.31)–(3.32) can be efficiently approximated by a special family of optimization problems of a similar structure but with the spatial regularization of the exponent $p(|\nabla u|)$ in the form

$$p_\varepsilon(|\nabla u|) = 1 + \delta + \frac{a^2(1-\delta)}{a^2 + |(\nabla K_\varepsilon * u)(x)|^2}, \tag{3.63}$$

where $(\nabla K_\varepsilon * u)$ stands for the Steklov smoothing operator.

Let $K : \mathbb{R}^2 \to \mathbb{R}$ be a positive compactly supported function such that

$$K \in C_0^\infty(\mathbb{R}^2), \quad \int_{\mathbb{R}^2} K(x)\,dx = 1, \quad \text{and } K(x) = K(-x),\ \forall\, x \in \mathbb{R}^2.$$

For any $\varepsilon > 0$, we set $K_\varepsilon(x) = \varepsilon^{-2} K\left(\frac{x}{\varepsilon}\right)$. Then the following properties of the convolution

$$u_\varepsilon(x) := (K_\varepsilon * u)(x) = \int_\Omega K_\varepsilon(x-y)u(y)\,dy, \quad \forall\, u \in L^1(\Omega),$$

are well-known [302]:

(i) $u_\varepsilon \in C^\infty(\Omega)$ for all $\varepsilon > 0$;

(ii) $u_\varepsilon(x) \to u(x)$ almost everywhere in $\Omega$;

(iii) If $u \in L^p(\Omega)$ with $1 \le p < \infty$, then $u_\varepsilon \to u$ in $L^p(\Omega)$.

We introduce the following family of approximating problems to the problem (3.31)–(3.32):

$$J_{i,\varepsilon}(f_{i,\varepsilon}^0) = \inf_{v \in \Xi_{i,\varepsilon}} J_{i,\varepsilon}(v), \quad i = 1,2,3, \tag{3.64}$$

where $\varepsilon$ is a small parameter which varies within a strictly decreasing sequence of positive numbers converging to 0,

$$J_{i,\varepsilon}(v) = \int_\Omega |R_\eta \nabla v(x)|^{p_\varepsilon(|\nabla v|)}\,dx + \frac{\mu}{2}\,\|v - f_i\|^2_{H^{-1}(\Omega)} + \frac{\lambda}{4}\left[D(v) - cD(f_i)\right]^2, \tag{3.65}$$

$$\Xi_{i,\varepsilon} = \left\{ I \in H^{1,p_\varepsilon(|\nabla I|)}(\Omega) \cap L^\infty(\Omega) \;\middle|\; \begin{array}{c} \gamma_{i,0} \le I(x) \le \gamma_{i,1} \quad \text{a.e. in } \Omega, \\ \gamma_{i,0} = \inf_{x\in\Omega} f_i(x), \\ \gamma_{i,1} = \sup_{x\in\Omega} f_i(x), \end{array} \right\} \tag{3.66}$$

and $p_\varepsilon(|\nabla v|)$ is defined in (3.63).

Before proceeding further, we make use of a few technical results.

**Lemma 3.5.1.** *[287, Lemma 1] Let $\{v_k\}_{k\in\mathbb{N}} \subset L^\infty(\Omega)$ be a sequence of measurable functions such that $v_k(x) \to v(x)$ weakly-$*$ in $L^\infty(\Omega)$ for some $v \in L^\infty(\Omega)$. Let*

$$\left\{ p_k = 1 + \delta + \frac{a^2(1-\delta)}{a^2 + |(\nabla K_\varepsilon * v_k)(x)|^2} \right\}_{k\in\mathbb{N}}$$

*be the corresponding sequence of exponents. Then*

$$\begin{gathered} p_{k,\varepsilon} \to p_\varepsilon = 1 + \delta + \frac{a^2(1-\delta)}{a^2 + |(\nabla K_\varepsilon * u)|^2} \quad uniformly\ in\ \overline{\Omega}\ as\ k \to \infty, \\ 1 + \delta + \frac{a^2(1-\delta)}{a^2 + \|K_\varepsilon\|^2_{C^1(\overline{\Omega-\Omega})} \sup_{k\in\mathbb{N}} \|v_k\|^2_{L^1(\Omega)}} \le p_{k,\varepsilon}(x) \le 2, \quad \forall\, x \in \Omega,\ \forall\, k \in \mathbb{N}, \end{gathered} \tag{3.67}$$

*where*

$$\|K_\varepsilon\|_{C^1(\overline{\Omega-\Omega})} = \max_{\substack{z=x-y \\ x\in\overline{\Omega}, y\in\overline{\Omega}}} \Big[ |K_\varepsilon(z)| + |\nabla K_\varepsilon(z)| \Big].$$

**Lemma 3.5.2.** *[276, Proposition B.2] The mapping $v \mapsto \frac{\lambda}{4}\left[D(v) - cD(f_i)\right]^2$ is continuous from $L^2(\Omega)$ endowed with thee strong topology to $\mathbb{R}$ with pointwise convergence.*

**Proposition 3.5.1.** *[287] Let $\{p_{k,\varepsilon}\}_{k\in\mathbb{N}}$ be a sequence of exponents that satisfies all preconditions of Lemma 3.5.1. If a bounded sequence $\left\{f_k \in L^{p_{k,\varepsilon}(\cdot)}(\Omega)\right\}_{k\in\mathbb{N}}$ converges weakly in $L^{1+\delta}(\Omega)$ to $f$, then $f \in L^{p_\varepsilon(\cdot)}(\Omega)$, $f_k \rightharpoonup f$ in variable $L^{p_{k,\varepsilon}(\cdot)}(\Omega)$.*

We are now in a position to prove the existence of minimizers for the proposed approximating problem (3.64)–(3.66).

**Theorem 3.5.1.** *Let $\Omega$ be an open bounded and connected sub-domain of $\mathbb{R}^2$ with a Lipschitz boundary. Let $f_i \in L^2(\Omega)$ be a given spectral channel of an image arguably contaminated by additive Gaussian noise with zero mean. Then, for each $\varepsilon > 0$, the minimization problem (3.64)–(3.66) admits at least one solution $f^0_{i,\varepsilon}$ in $W^{1,p^-}(\Omega) \cap L^\infty(\Omega)$ such that $I^0_{i,\varepsilon} \in H^{1,p[\nabla f^0_{i,\varepsilon}]}(\Omega)$.*

*Proof.* To begin with, let us notice that, for each $\varepsilon > 0$, the indicated minimization problem is consistent, i.e. $J_{i,\varepsilon}(u) < +\infty$ for any $u \in \Xi_{i,\varepsilon}$. Since $\Xi_{i,\varepsilon} \neq \emptyset$ and $0 \le J_{i,\varepsilon}(v) < +\infty$ for all $v \in \Xi_{i,\varepsilon}$, it follows that there exists a non-negative value $\zeta \ge 0$ such that $\zeta_\varepsilon = \inf_{v\in\Xi_{i,\varepsilon}} J_{i,\varepsilon}(v)$. Let $\{v^\varepsilon_k\}_{k\in\mathbb{N}}$ be a minimizing sequence for (3.64)–(3.66), i.e.

$$\{v^\varepsilon_k\}_{k\in\mathbb{N}} \subset \Xi_{i,\varepsilon} \ \text{ and } \lim_{k\to\infty} J_{i,\varepsilon}\left(v^\varepsilon_k\right) = \zeta_\varepsilon.$$

Without lost of generality, we can suppose that $J_{i,\varepsilon}(v_k^\varepsilon) \le \zeta_\varepsilon + 1$ for all $k \in \mathbb{N}$. From this and estimate (3.36), we deduce

$$\|v_k^\varepsilon\|^{p^-}_{W^{1,p_\varepsilon(|\nabla v_k^\varepsilon|)}} \le C\left(|\Omega|\gamma_{i,1}^2 + 2 + \frac{\zeta_\varepsilon + 1}{(1-\eta^2)^2}\right), \quad \forall\, k \in \mathbb{N}, \tag{3.68}$$

$$\|v_k^\varepsilon\|_{L^\infty(\Omega)} \le \gamma_{i,1}, \quad \forall\, k \in \mathbb{N}. \tag{3.69}$$

Hence, in view of (3.7) and (3.33), the sequence $\{v_k^\varepsilon\}_{k\in\mathbb{N}}$ is bounded in $W^{1,p^-}(\Omega)$. Therefore, there exist a subsequence of $\{v_k^\varepsilon\}_{k\in\mathbb{N}}$, still denoted by the same index, and a vector function $f_{i,\varepsilon}^0 \in W^{1,p^-}(\Omega)$ such that

$$v_k^\varepsilon \to f_{i,\varepsilon}^0 \text{ strongly in } L^q(\Omega) \text{ for all } q \in [1,(p^-)^*) \text{ as } k \to \infty, \tag{3.70}$$

$$v_k^\varepsilon \overset{*}{\rightharpoonup} f_{i,\varepsilon}^0 \text{ weakly-}* \text{ in } L^\infty(\Omega) \text{ as } k \to \infty, \tag{3.71}$$

$$v_k^\varepsilon \rightharpoonup f_{i,\varepsilon}^0 \text{ weakly in } W^{1,p^-}(\Omega) \text{ as } k \to \infty, \tag{3.72}$$

where, by Sobolev embedding theorem, $(p^-)^* = \frac{2p^-}{2-p^-} = \frac{2+2\delta}{1-\delta} > 2$.

In view of this and the smoothness of the kernel $K_\varepsilon$, we see that the operator

$$L^{p^-}(\Omega;\mathbb{R}^2) \ni \nabla v \mapsto p_\varepsilon(|\nabla v|) \in C(\overline{\Omega})$$

is compact (see Lemma 3.5.1). So, (3.71)–(3.72) imply that $p_\varepsilon(|\nabla v_k^\varepsilon|) \to p_\varepsilon(|\nabla f_{i,\varepsilon}^0|)$ in $C(\overline{\Omega})$. Passing then to a subsequence if necessary, we have (see Propositions 3.3.1 and 3.5.1):

$$v_k^\varepsilon(x) \to f_{i,\varepsilon}^0(x) \ \text{ a.e. in } \Omega. \tag{3.73}$$

$$v_k^\varepsilon \rightharpoonup f_{i,\varepsilon}^0 \ \text{ weakly in variable } L^{p_\varepsilon(|\nabla v_k^\varepsilon|)}(\Omega),$$

$$\nabla v_k^\varepsilon \rightharpoonup \nabla f_{i,\varepsilon}^0 \ \text{ weakly in variable } L^{p_\varepsilon(|\nabla v_k^\varepsilon|)}(\Omega;\mathbb{R}^2).$$

Hence, $f_{i,\varepsilon}^0 \in W^{1,p_\varepsilon(|\nabla f_{i,\varepsilon}^0|)}(\Omega)$.

Further we notice that, for each $k \in \mathbb{N}$, $\gamma_{i,0} \le v_k^\varepsilon(x) \le \gamma_{i,1}$ a.a. in $\Omega$. Then it follows from (3.73) that the limit function $f_{i,\varepsilon}^0(x)$ is also subjected to the same restriction. Thus, $f_{i,\varepsilon}^0 \in W^{1,p_\varepsilon(|\nabla f_{i,\varepsilon}^0|)}(\Omega) \cap L^\infty(\Omega)$ is a feasible solution to minimization problem (3.64)–(3.66).

It remains to show that $f_{i,\varepsilon}^0$ is a minimizer of this problem. Indeed, taking into account the properties (3.68), (3.72) and the fact that $\theta \in L^\infty(\Omega,\mathbb{R}^2)$, we see that the sequence

$$\left\{\left|R_\eta \nabla v_k^\varepsilon := \nabla v_k^\varepsilon - \eta^2\,(\theta, \nabla v_k^\varepsilon)\,\theta\right| \in L^{p_\varepsilon(|\nabla v_k^\varepsilon|)}(\Omega;\mathbb{R}^2)\right\}_{k\in\mathbb{N}}$$

is bounded in variable space $L^{p_\varepsilon(|\nabla v_k^\varepsilon|)}(\Omega;\mathbb{R}^2)$ and weakly convergent to $|R_\eta \nabla f_{i,\varepsilon}^0|$ in $L^{p^-}(\Omega;\mathbb{R}^2)$. Hence, by Proposition 3.3.1, the following lower semicontinuous

property

$$\liminf_{k\to\infty}\int_\Omega |R_\eta\nabla v_k^\varepsilon(x)|^{p_\varepsilon(|\nabla v_k^\varepsilon|)}\,dx \geq \int_\Omega |R_\eta\nabla f_{i,\varepsilon}^0(x)|^{p_\varepsilon(|\nabla f_{i,\varepsilon}^0|)}\,dx$$

holds. Combining this relation with the following ones

$$\begin{aligned}\lim_{k\to\infty}\|v_k^\varepsilon - f_i\|^2_{H^{-1}(\Omega)} &= \left\|f_{i,\varepsilon}^0 - f_i\right\|^2_{H^{-1}(\Omega)},\\ \lim_{k\to\infty}\left[D(v_k^\varepsilon) - cD(f_i)\right]^2 &= \left[D(f_{i,\varepsilon}^0) - cD(f_i)\right]^2,\end{aligned}$$

which are direct consequence of Lemma 3.5.2 and compactness of the embedding $L^2(\Omega)\subset H^{-1}(\Omega)$, we finally obtain

$$\begin{aligned}\zeta_\varepsilon &= \inf_{v\in\Xi_{i,\varepsilon}} J_{i,\varepsilon}(v) = \lim_{k\to\infty} J_{i,\varepsilon}\left(v_k^\varepsilon\right) = \liminf_{k\to\infty} J_{i,\varepsilon}\left(v_k^\varepsilon\right)\\ &\geq \int_\Omega |R_\eta\nabla f_{i,\varepsilon}^0(x)|^{p_\varepsilon(|\nabla f_{i,\varepsilon}^0|)}\,dx + \frac{\mu}{2}\left\|f_{i,\varepsilon}^0 - f_i\right\|^2_{H^{-1}(\Omega)}\\ &\quad + \frac{\lambda}{4}\left[D(f_{i,\varepsilon}^0) - cD(f_i)\right]^2 = J_{i,\varepsilon}(f_{i,\varepsilon}^0).\end{aligned}$$

Thus, $f_{i,\varepsilon}^0$ is a minimizer to the problem (3.64)–(3.66). □

Taking this existence result into account, we pass to the study of approximation properties of the problems (3.64)–(3.66). Namely, the main question we are going to discuss further is whether we can establish the convergence of minima of (3.64)–(3.66) to minima of (3.31)–(3.32) as $\varepsilon$ tends to zero. In other words, we aim to show that some optimal solutions to (3.31)–(3.32) can be approximated by the solutions of (3.64)–(3.66). To this end, we make use of some results of the variational convergence of minimization problems [303]-[307] and begin with some auxiliaries (see also [308]-[312] for other aspects of this concept).

**Lemma 3.5.3.** *Let $\{\varepsilon_k\}_{k\in\mathbb{N}}$ be a sequence of positive numbers converging to zero as $k\to\infty$. Let*

$$\{v_k\}_{k\in\mathbb{N}} \quad \textit{and} \quad \left\{p_k := 1+\delta+\frac{a^2(1-\delta)}{a^2+|(\nabla K_{\varepsilon_k} * v_k)|^2}\right\}_{k\in\mathbb{N}}$$

*be sequences such that*

$$v_k \in \Xi_{i,\varepsilon_k}, \quad \forall\, k \in \mathbb{N}, \tag{3.74}$$

$$v_k(x) \to v(x) \quad a.e.\ in\ \Omega, \tag{3.75}$$

$$v_k \to v \quad strongly\ in\ L^2(\Omega), \tag{3.76}$$

$$\nabla v_k \rightharpoonup \nabla v \quad weakly\ in\ L^{p^-}(\Omega;\mathbb{R}^2), \tag{3.77}$$

$$\left\| |\nabla v_k(\cdot)|^{p_k(\cdot)} \right\|_{L^1(\Omega)} \le C \text{ for some positive constant } C \text{ not depending on } k, \tag{3.78}$$

$$p_k(x) \to p(x) := 1 + \delta + \frac{a^2(1-\delta)}{a^2 + |\nabla v|^2} \quad a.e.\ in\ \Omega. \tag{3.79}$$

$$Then \quad v \in \Xi_i \quad and \quad J_i(v) \le \liminf_{k\to\infty} J_{i,\varepsilon_k}(v_k), \quad \forall\, i = 1, 2, 3.. \tag{3.80}$$

*Proof.* The following relations

$$\lim_{k\to\infty} \|v_k - f_i\|^2_{H^{-1}(\Omega)} = \|v - f_i\|^2_{H^{-1}(\Omega)}\,, \tag{3.81}$$

$$\lim_{k\to\infty} [D(v_k) - cD(f_i)]^2 = [D(v) - cD(f_i)]^2 \tag{3.82}$$

are a direct consequence of Lemma 3.5.2, compactness of the embedding $L^2(\Omega) \subset H^{-1}(\Omega)$, and condition (3.76). We also notice that, in view of representation

$$R_\eta \nabla v_k := \nabla v_k - \eta^2\,(\theta, \nabla v_k)\,\theta, \quad \forall\, k \in \mathbb{N},$$

Proposition 3.3.1 and the initial assumptions (3.77)–(3.79) lead to the conclusion:

$$\nabla v \in L^{p(\cdot)}(\Omega;;\mathbb{R}^2) \quad \text{and} \quad \liminf_{k\to\infty} \int_\Omega |R_\eta \nabla v_k(x)|^{p_k(x)}\,dx \ge \int_\Omega |R_\eta \nabla v(x)|^{p(x)}\,dx.$$

As a result, combining the last inequality with (3.81)–(3.82), we arrive at the announced relation $(3.80)_2$.

It remains to show that $v$ is a feasible solution to the problem (3.31)–(3.32), i.e., $v \in \Xi_i$. To this end, we take into account the inclusion $\nabla v \in L^{p(\cdot)}(\Omega;;\mathbb{R}^2)$ established above and the fact that $v_k \in \Xi_{i,\varepsilon_k}$ for each $k \in \mathbb{N}$. Then it follows from (3.75) that $\gamma_{i,0} \le v(x) \le \gamma_{i,1}$ almost everywhere in $\Omega$, and, therefore, $v \in \Xi_i$. □

**Lemma 3.5.4.** *For each feasible solution $v \in \Xi_i$ to the original problem* (3.31)–

(3.32), *there can be found a sequence* $\{v_\varepsilon\}_{\varepsilon\to 0}$ *such that*

$$v_\varepsilon \in \Xi_{i,\varepsilon}, \quad \forall\, \varepsilon \in (0,\varepsilon_0) \text{ with } \varepsilon_0 > 0 \text{ sufficiently small}, \tag{3.83}$$

$$v_e(x) \to v(x) \quad a.e. \text{ in } \Omega \text{ as } \varepsilon \to 0, \tag{3.84}$$

$$v_\varepsilon \to v \quad \text{strongly in } L^2(\Omega), \tag{3.85}$$

$$\nabla v_\varepsilon \to \nabla v \quad \text{strongly in } L^{p^-}(\Omega;\mathbb{R}^2), \tag{3.86}$$

$$\big\||\nabla v_\varepsilon(\cdot)|^{p_\varepsilon(\cdot)}\big\|_{L^1(\Omega)} \le C \quad \text{for some positive constant } C \text{ not depending on } \varepsilon, \tag{3.87}$$

$$p_\varepsilon(x) := 1+\delta+\frac{a^2(1-\delta)}{a^2+|(\nabla K_\varepsilon * v_\varepsilon)|^2} \to p(x) := 1+\delta+\frac{a^2(1-\delta)}{a^2+|\nabla v|^2} \quad a.e. \text{ in } \Omega, \tag{3.88}$$

$$J_i(v) \ge \limsup_{\varepsilon\to 0} J_{i,\varepsilon}(v_\varepsilon). \tag{3.89}$$

*Proof.* Let $v$ be an arbitrary feasible solution to the problem (3.31)–(3.32). We define the sequence $\{v_\varepsilon\}_{\varepsilon\to 0}$ as a smooth mollification of $v$ with the kernel $K_\varepsilon$, i.e.,

$$v_\varepsilon(x) := (K_\varepsilon * v)(x) = \int_\Omega K_\varepsilon(x-y)v(y)\,dy, \quad \forall\, x \in \Omega.$$

Then properties (3.84)–(3.86) are direct consequences of the Steklov smoothing procedure (see (i)–(iii)). Moreover, in view of (3.84) and the fact that $\gamma_{i,0} \le v(x) \le \gamma_{i,1}$ a.e. in $\Omega$, we can suppose that the same restriction for $v_\varepsilon$

$$\gamma_{i,0} \le v_\varepsilon(x) \le \gamma_{i,1} \quad \text{a.e. in } \Omega \tag{3.90}$$

holds true with $\varepsilon > 0$ small enough.

Since $v_\varepsilon \to v$ strongly in $W^{1,p^-}(\Omega)$, it follows without loss of generality that $\nabla v_\varepsilon(x) \to \nabla v(x)$ almost everywhere in $\Omega$. As a result, this implies the pointwise convergence (3.88). Hence,

$$|R_\eta \nabla v_\varepsilon(x)|^{p_\varepsilon(x)} \to |R_\eta \nabla v(x)|^{p(x)} \quad \text{a.e. in } \Omega.$$

From this and the fact that $|R_\eta \nabla v(x)|^{p(x)} \in L^1(\Omega)$, we deduce:

$$|R_\eta \nabla v_\varepsilon|^{p_\varepsilon(\cdot)} \to |R_\eta \nabla v|^{p(\cdot)} \quad \text{strongly in } L^1(\Omega). \tag{3.91}$$

Thus, $\big\||R_\eta \nabla v_\varepsilon(\cdot)|^{p_\varepsilon(\cdot)}\big\|_{L^1(\Omega)} \le C$ for some positive constant $C$ not depending on $\varepsilon$. Hence, in view of estimates (3.34), we get: $\nabla v_\varepsilon \in L^{p_\varepsilon(\cdot)}(\Omega;;\mathbb{R}^2)$ for $\varepsilon$ small enough. From this and (3.90), the assertion (3.83) follows. Moreover, the following equality

$$\lim_{\varepsilon\to 0}\int_\Omega |R_\eta \nabla v_\varepsilon|^{p_\varepsilon(\cdot)}\,dx = \int_\Omega |R_\eta \nabla v|^{p(\cdot)}\,dx \tag{3.92}$$

immediately follows from (3.91).

It remains to observe that

$$\lim_{k\to\infty} \|v_k - f_i\|^2_{H^{-1}(\Omega)} = \|v - f_i\|^2_{H^{-1}(\Omega)}\,, \tag{3.93}$$

$$\lim_{k\to\infty} [D(v_k) - cD(f_i)]^2 = [D(v) - cD(f_i)]^2\,, \tag{3.94}$$

by Lemma 3.5.2 and compactness of the embedding $L^2(\Omega) \subset H^{-1}(\Omega)$. As a result, we conclude from (3.92), (3.93), and (3.94) that, in fact, instead of the announced inequality (3.89), we have $J_i(v) = \lim_{\varepsilon\to 0} J_{i,\varepsilon}(v_\varepsilon)$. The proof is complete. □

We are now in a position to prove the main result of this section.

**Theorem 3.5.2.** *Assume that the original minimization problem* (3.31)–(3.32) *has a non-empty set of minimizers. Let* $\left\{f^0_{i,\varepsilon} \in \Xi_{i,\varepsilon}\right\}_{\varepsilon>0}$ *be a sequence of solutions to the corresponding minimization problems* (3.64)–(3.66). *Let* $\left\{p_\varepsilon := 1 + \delta + \frac{a^2(1-\delta)}{a^2 + \left|(\nabla K_\varepsilon * f^0_{i,\varepsilon})\right|^2}\right\}_{\varepsilon>0}$ *be the sequence of associated exponents.*

*Assume that the sequence* $\{p_\varepsilon\}_{\varepsilon>0}$ *is compact with respect to the pointwise convergence in* $\Omega$. *Then there exists an element* $f^0_i \in \Xi$ *such that, up to a subsequence,*

$$f^0_{i,\varepsilon}(x) \to f^0_i(x) \quad \text{a.e. in } \Omega \text{ as } \varepsilon \to 0, \tag{3.95}$$

$$f^0_{i,\varepsilon} \to f^0_i \quad \text{strongly in } L^2(\Omega), \tag{3.96}$$

$$\nabla f^0_{i,\varepsilon} \rightharpoonup \nabla f^0_i \quad \text{weakly in } L^{p^-}(\Omega;\mathbb{R}^2), \tag{3.97}$$

$$\left\||\nabla f^0_{i,\varepsilon}(\cdot)|^{p_\varepsilon(\cdot)}\right\|_{L^1(\Omega)} \le C \quad \text{for some positive constant } C \text{ not depending on } \varepsilon, \tag{3.98}$$

$$\inf_{v\in\Xi_{i,\varepsilon}} J_i(v) = J_i(f^0_i) = \lim_{\varepsilon\to 0} J_{i,\varepsilon}(f^0_{i,\varepsilon}) = \lim_{\varepsilon\to 0} \inf_{v\in\Xi_{i,\varepsilon}} J_{i,\varepsilon}(v_\varepsilon). \tag{3.99}$$

*Proof.* First, we observe that a given sequence of minimizers for approximating problems (3.64)–(3.66) is compact with respect to the convergence (3.95)–(3.97). Indeed, for an arbitrary test function $\varphi \in C^\infty_c(\mathbb{R}^2)$, we have:

$$\varphi \in H^{1,p_\varepsilon(\cdot)}(\Omega), \quad \forall\, \varepsilon > 0.$$

Let's assume that this function satisfies the pointwise constraints $\gamma_{i,0} \le \varphi(x) \le \gamma_{i,1}$ in $\Omega$. Then, $\varphi \in \Xi_{i,\varepsilon}$ for all $\varepsilon > 0$, and, therefore, we can suppose that

$$J_{i,\varepsilon}(f^0_{i,\varepsilon}) = \inf_{v\in\Xi_{i,\varepsilon}} J_{i,\varepsilon}(v_\varepsilon) \le J_{i,\varepsilon}(\varphi) \le \sup_{\varepsilon>0} J_{i,\varepsilon}(\varphi) \le C < +\infty \quad \forall\, \varepsilon > 0.$$

Hence,

$$\sup_{\varepsilon>0} \int_\Omega |R_\eta \nabla f^0_{i,\varepsilon}(\cdot)|^{p_\varepsilon(\cdot)}\, dx \le C \quad \text{and} \quad \sup_{\varepsilon>0} \|f^0_{i,\varepsilon}\|_{L^2(\Omega)} \le \sqrt{\|\Omega|}\gamma_{i,1}. \tag{3.100}$$

Combining this issue with estimates (3.34), we see that the sequence $\left\{f^0_{i,\varepsilon} \in \Xi_{i,\varepsilon}\right\}_{\varepsilon>0}$ is bounded in $W^{1,p^-}(\Omega)$. Hence, there exist a subsequence $\left\{f^0_{i,k} \in \Xi_{i,\varepsilon_k}\right\}_{k\in\mathbb{N}}$ of $\left\{f^0_{i,\varepsilon} \in \Xi_{i,\varepsilon}\right\}_{\varepsilon>0}$, and a function $f^0_i \in W^{1,p^-}(\Omega)$ such that

$$\begin{aligned} f^0_{i,k} &\to f^0_i \text{ strongly in } L^q(\Omega) \; for \; all \; q \in [1,(p^-)^*), \\ f^0_{i,k} &\rightharpoonup f^0_i \text{ weakly in } W^{1,p^-}(\Omega) \; as \; k \to \infty, \end{aligned} \tag{3.101}$$

where, by Sobolev embedding theorem, $(p^-)^* = \frac{2p^-}{2-p^-} = \frac{2+2\delta}{1-\delta} > 2+\delta$. From this, the conditions (3.95)–(3.97) follow, whereas (3.98) is a consequence of (3.34) and the boundedness property (3.100).

Thus, we may suppose that for the subsequence $\left\{f^0_{i,k} \in \Xi_{\varepsilon_k}\right\}_{k\in\mathbb{N}}$ all preconditions of Lemma 3.5.3 are fulfilled. Therefore, property (3.80) leads us to the conclusion that $f^0_i \in \Xi_i$ and

$$\liminf_{k\to\infty} \inf_{v\in\Xi_{i,e_k}} J_{i,\varepsilon_k}(v) = \liminf_{k\to\infty} J_{i,\varepsilon_k}(f^0_{i,k}) \geq J_i(f^0_i) \geq \inf_{v\in\Xi_i} J_i(v) = J_i(f^*_i), \tag{3.102}$$

where $f^*_i \in \Xi$ is a minimizer for (3.31)–(3.32).

Then Lemma 3.5.4 implies the existence of a realizing sequence $\left\{f^*_{i,\varepsilon} \in \Xi_{i,\varepsilon}\right\}_{\varepsilon>0}$ such that $f^*_{i,\varepsilon} \to f^*_i$ as $\varepsilon \to 0$ in the sense of relations (3.84)–(3.88), and

$$J_i(f^*_i) \geq \limsup_{\varepsilon\to 0} J_{i,\varepsilon}(f^*_{i,\varepsilon}).$$

Utilizing this fact, we have

$$\begin{aligned} \inf_{v\in\Xi_i} J_i(v) = J_i(f^*_i) &\geq \limsup_{\varepsilon\to 0} J_{i,\varepsilon}(f^*_{i,\varepsilon}) \geq \limsup_{\varepsilon\to 0} \inf_{v\in\Xi_{i,\varepsilon}} J_{i,\varepsilon}(v) \\ &\geq \limsup_{k\to\infty} \inf_{v\in\Xi_{i,\varepsilon_k}} J_{i,\varepsilon_k}(v) = \limsup_{k\to\infty} J_{i,\varepsilon_k}(f^0_{i,k}). \end{aligned} \tag{3.103}$$

From this and (3.102) we deduce that

$$\liminf_{k\to\infty} J_{i,\varepsilon_k}(f^0_{i,k}) \geq \limsup_{k\to\infty} J_{i,\varepsilon_k}(f^0_{i,k}).$$

Hence, we can combine (3.102) and (3.103) to get

$$J_i(f^0_i) = J_i(f^*_i) = \inf_{v\in\Xi_i} J_i(v) = \lim_{k\to\infty} \inf_{v\in\Xi_{i,\varepsilon_k}} J_{i,\varepsilon_k}(v). \tag{3.104}$$

Using these relations and the fact that the problem (3.31)–(3.32) is solvable, we may suppose that $f^*_i = f^0_i$. Since equality (3.104) holds for all subsequences of $\left\{f^0_{i,\varepsilon}\right\}_{\varepsilon>0}$, which are convergent in the sense of relations (3.95)–(3.97), it follows that these limits coincide and, therefore, $f^0_i$ is the limit of the whole sequence

$\left\{f^0_{i,\varepsilon}\right\}_{\varepsilon>0}$. Then, using the same argument for the sequence of minimizers as we did for the subsequence $\left\{f^0_{i,\varepsilon_k}\right\}_{k\in\mathbb{N}}$, we finally obtain

$$\begin{aligned}\liminf_{\varepsilon\to 0}\inf_{v\in\Xi_{i,\varepsilon}} J_{i,\varepsilon}(v) &= \liminf_{\varepsilon\to 0} J_{i,\varepsilon}(f^0_{i,\varepsilon}) \geq J_i(f^0_i) = \inf_{v\in\Xi_i} J_i(v)\\ &\geq \limsup_{\varepsilon\to 0} J_{i,\varepsilon}(f^*_{i,\varepsilon}) \geq \limsup_{\varepsilon\to 0}\inf_{v\in\Xi_{i,\varepsilon}} J_{i,\varepsilon}(v)\\ &= \limsup_{\varepsilon\to 0} J_{i,\varepsilon}(f^0_{i,\varepsilon}),\end{aligned}$$

and this concludes the proof. □

**Remark 3.5.1.** *It is worth to emphasize a few principle issues from Theorem 3.5.2. The first one is that, in practice, the assumption concerning solvability of the original optimization problem is not so restricted and, in principle, it can be omitted. Indeed, any digital color image $f = [f_1, f_2, f_3]^t$ is originally defined on some grid $G$. So, each of its spectral channels $f_i\Big|_G$ can be associated with some real-valued matrix. Hence, we can always suppose that the exponent $p(|\nabla f_i|)\Big|_G$ is the restriction on the same grid of some Lipschitz-continuous function $p(\cdot):\Omega\to\mathbb{R}$. Then arguing as in the proof of Theorem 3.5.1, the solvability of the problem* (3.31)–(3.32) *can be easily established.*

*The second point, that should be emphasized here, is the assumption about the compactness property of the sequence of associated exponents* $\left\{p_\varepsilon := 1+\delta+\frac{a^2(1-\delta)}{a^2+\left|(\nabla K_\varepsilon * f^0_{i,\varepsilon})\right|^2}\right\}_{\varepsilon>0}$ *with respect to the pointwise convergence in $\Omega$.*

*Since this property is crucial in Theorem 3.5.2, we propose to consider it as an easily realized in practice criterion for the verification of whether the approximating sequence $\left\{f^0_{i,\varepsilon}\in\Xi_{i,\varepsilon}\right\}_{\varepsilon>0}$ leads to some optimal solution of the original problem.*

## 3.6 Numerical results

To illustrate the implementation of the proposed model (3.31)–(3.32) to the simultaneous denoising and contrast enhancement of color images, we make use of the optimality conditions in the form of (3.62). In other words, we have dropped the two-side constraints $\gamma_{i,0}\leq v(x)\leq\gamma_{i,1}$ from the sets $\Xi_i$, and instead we control the fulfilment of this two-side constraint at each step of the numerical approximations.

Since, in practical implementations, it is reasonable to define the solution of the problem (3.31)–(3.32) using a gradient descent strategy, we can start with some initial image $f = [f_1, f_2, f_3]^t \in L^2(\Omega;\mathbb{R}^3)$ and pass to the following system of three initial-boundary value problems for quasi-linear parabolic equations with

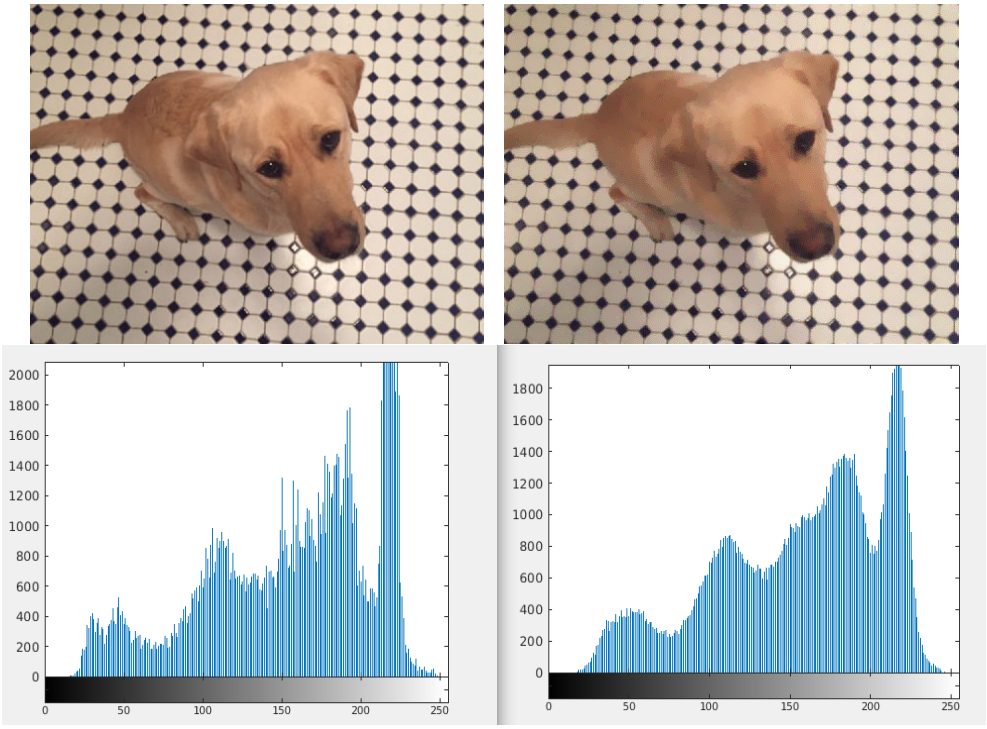


Figure 3.1: Original image (left) and its smoothed version without contrasting ($\mu = 0$) (right).

Neumann boundary conditions

$$\begin{aligned}
\frac{\partial f_i^0}{\partial t} &= \operatorname{div}\left[p(x)|R_\eta \nabla f_i^0|^{p(|\nabla f_i^0|)-2} R_\eta \nabla f_i^0\right] \\
&\quad - \eta^2 \operatorname{div}\left[p(x)\left(|R_\eta \nabla f_i^0|^{p(|\nabla f_i^0|)-2} R_\eta \nabla f_i^0, \theta\right)\theta\right] \\
&\quad - 2a^2(1-\delta)\operatorname{div}\left[|R_\eta \nabla f_i^0|^{p(|\nabla f_i^0|)} \frac{\log\left(|R_\eta \nabla f_i^0|\right)}{\left(a^2 + |\nabla f_i^0|^2\right)^2} \nabla f_i^0\right] \\
&\quad - \lambda\left(D(f_i^0) - cD(f_i)\right) \int_\Omega W(x,y) \frac{f_i^0(x) - f_i^0(y)}{\sqrt{\kappa^2 + |f_i^0(x) - f_i^0(y)|^2}}\, dy \\
&\quad - \mu(-\Delta)^{-1}(f_i^0 - f_i) = 0, \quad \text{in} \quad (0,T)\times\Omega, \qquad (3.105) \\
&\left(|\nabla f_i^0|^{p(|\nabla f_i^0|)-2} \nabla f_i^0, \nu\right) = 0 \quad \text{on} \quad (0,T)\times\partial\Omega, \qquad (3.106) \\
&f_i^0(0,\cdot) = f_i(\cdot), \quad i = 1,2,3, \quad \text{in} \quad \Omega. \qquad (3.107)
\end{aligned}$$

For numerical simulations, we set: $\delta = \kappa$ in (3.24) and (3.21), and $\eta = 1 - \kappa$ in (3.19), $\kappa = 0.001$, $\lambda = 0.1$, and $\mu = 2$. As for the noise estimator $a > 0$ in (3.21),

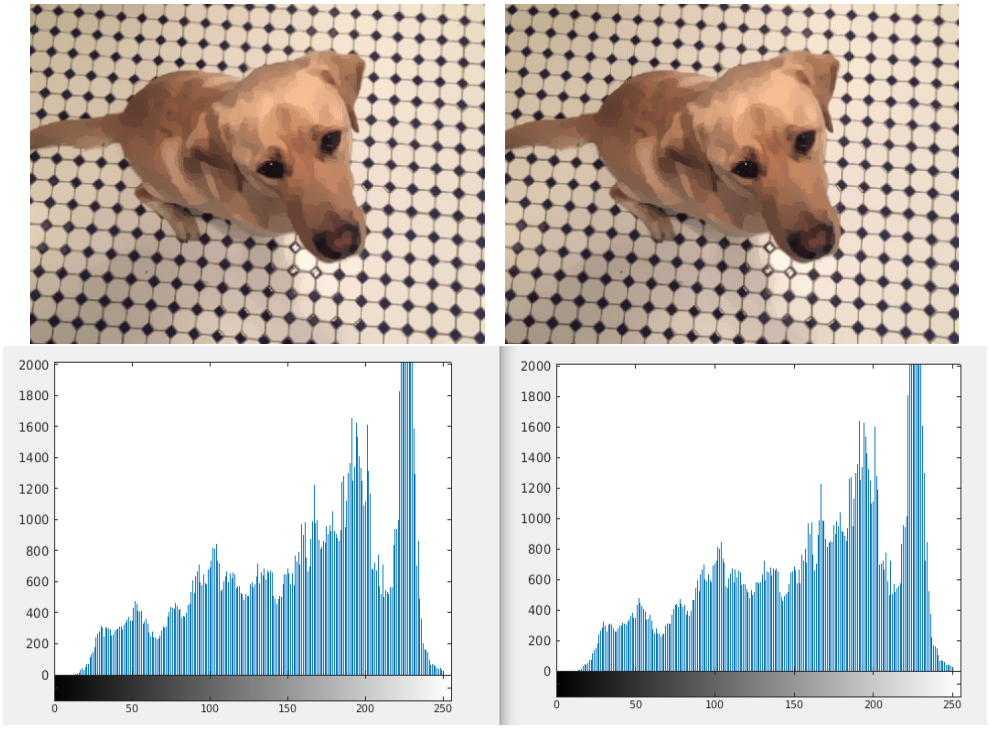


Figure 3.2: Variants of contrast enhancement with the corresponding histograms (from the left to the right): $c = 2$ and $window = 5$, $c = 2$ and $window = 7$.

we use the choice of Black et al. [313], i.e.

$$a = \frac{1.4826}{\sqrt{2}} MAD(\nabla f_i),$$

where $MAD$ denotes the median absolute deviation of the corresponding spectral channel $f_i$ of original image $f = [f_1, f_2, f_3]^t$ that can be computed as

$$MAD(\nabla f_i) = \text{median} \left[ \left| |\nabla f_i| - \text{median} \left( |\nabla f_i| \right) \right| \right]$$

and $\text{median} \left( \left| \nabla \widetilde{S}_i \right| \right)$ represents the median over the band $S_i : G_H \to \mathbb{R}$ to the gradient amplitude.

To guarantee the stability of the proposed algorithm, we make use of the following condition

$$2 \left[ \frac{1}{\kappa} + \lambda + \mu \right] \Delta t < 1.$$

There are numerous approaches to solve quasi-linear partial differential equations (see the references [314, 315] for various techniques). Since we are dealing with pixels in image processing, finite differences approaches and an explicit

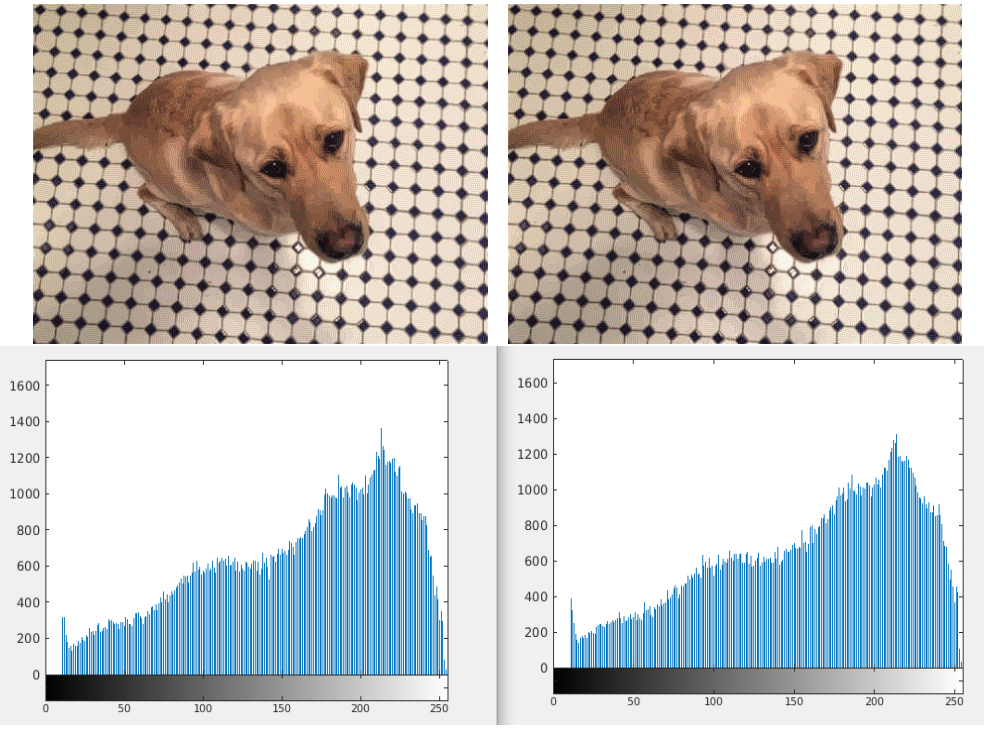


Figure 3.3: Variants of contrast enhancement with the corresponding histograms (from the left to the right): $c = 10$ and $window = 5$, $c = 10$ and $window = 7$.

scheme of the forward Euler method are arguably the best options. The number of iterations for each spectral channel can be defined experimentally. We used $10^3$-iterations. As for the size of the kernel $W(x, y)$ used for $D$, this size manages the scale of the contrast enhancement. In our experiments, we used it equal to $3, 5, 7, 15$, albeit it can be related to the size of the input image.

The most expensive computation is the one of $D$ and $\nabla D$ embedded in the computation of the right-hand side of the system (3.105). For acceleration of these computations, we can refer to [276], where the efficient Bernstein polynomials approximation has been proposed.

As follows from the result of numerical simulations (see Fig. 3.3–3.9), parameters $c$, $\mu$, $\lambda$, and the size of $window$ for the kernel $W(x, y)$ are crucial for the contrast enhancement and these parameters have to be tuned in dependence on the desired result. In particular, we observe that at a large scale ($window$) and low contrast level $c$, the proposed model can produce an image with more details, but with the same lighting sensation as the original one. To show how the choice of the parameters $c$, $\mu$, $\lambda$, and $window$ affect the results of contrast enhancement, we supplied all images in Fig. 3.1–3.9 by the histograms of their luma components which represent the perceptual brightness of the color images

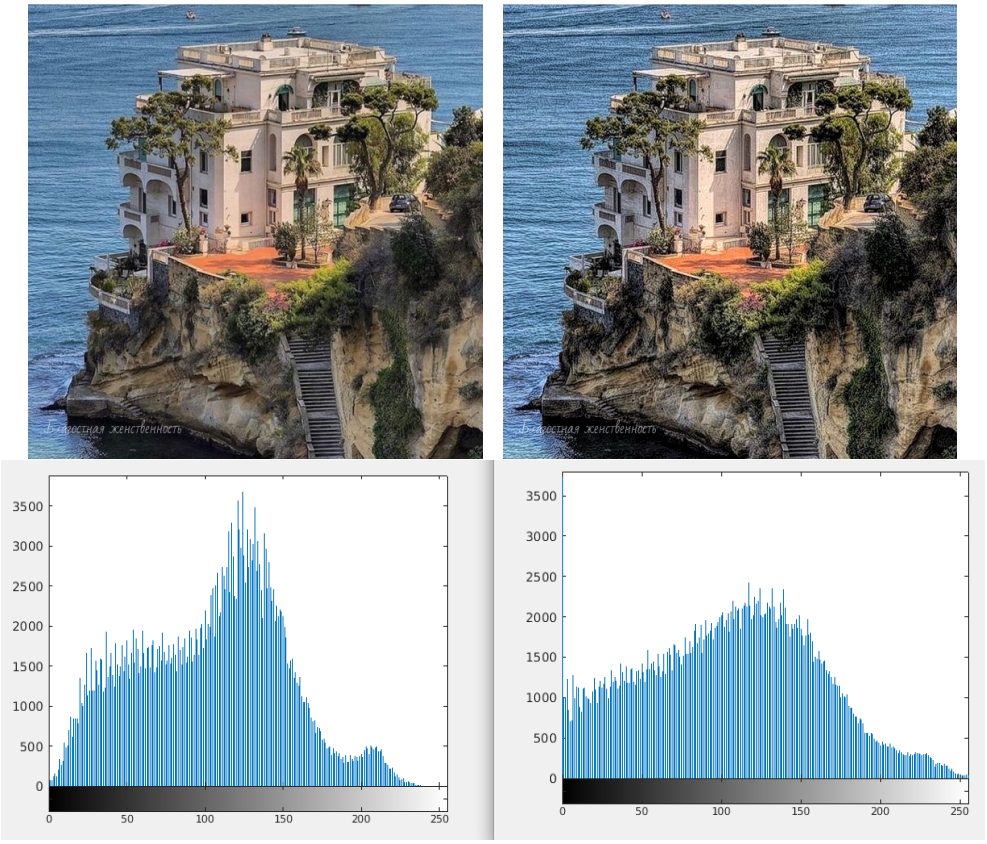


Figure 3.4: Variants of contrast enhancement with the corresponding histograms (from the left to the right): original image, restored image with $c = 20$ and $window = 15$.

$I : \Omega \to \mathbb{R}^3$. To this end, we used the following representation for the luma $Y_I(x) = \alpha_R I_R(x) + \alpha_G I_G(x) + \alpha_B I_B(x)$ with

$$\alpha_R = 0.299, \quad \alpha_G = 0.587, \quad \alpha_B = 0.114.$$

Here, $I_R$, $I_G$, and $I_N$ stand for the intensities of a given image in R, G and B spectral channels, respectively.

In particular, as follows from the obtained histograms, the proposed variational model is sufficiently sensitive to the choice of the weight coefficient $c$, whereas the size of $window$ for the kernel $W(x, y)$ affects the contrast enhancement in rather a mild manner (see Fig. 3.2–3.3).

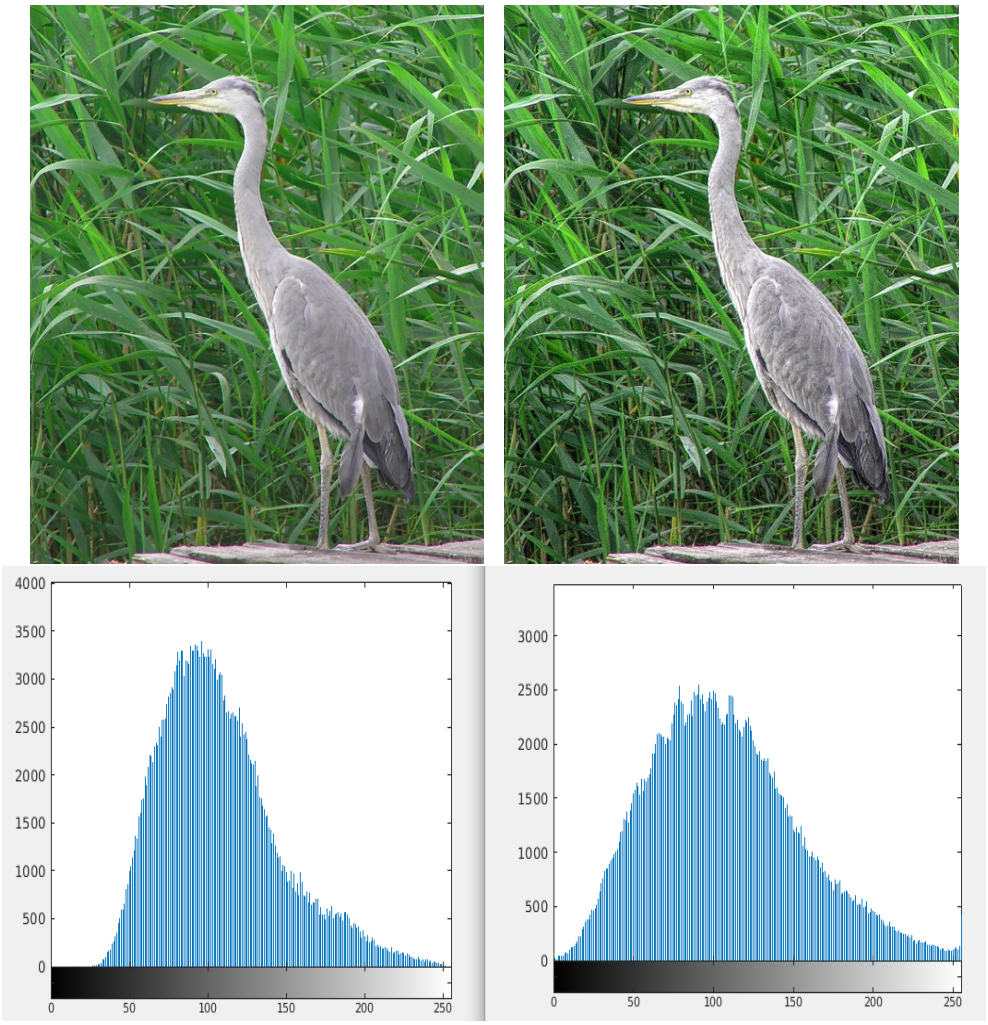


Figure 3.5: Variants of contrast enhancement with the corresponding histograms (from the left to the right): original and restored with $c = 10$ and $window = 7$.

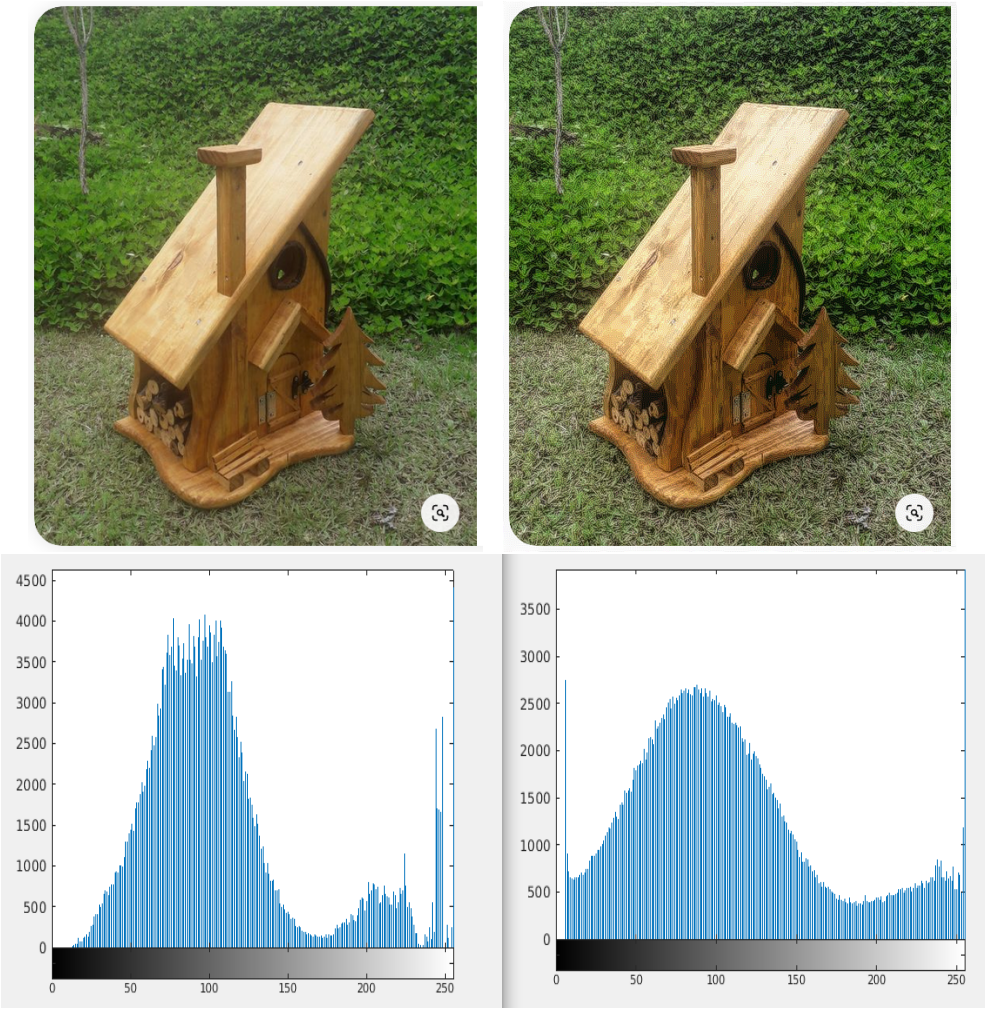


Figure 3.6: Variants of contrast enhancement with the corresponding histograms (from the left to the right): original image, restored image with $c = 10$ and $window = 5$.

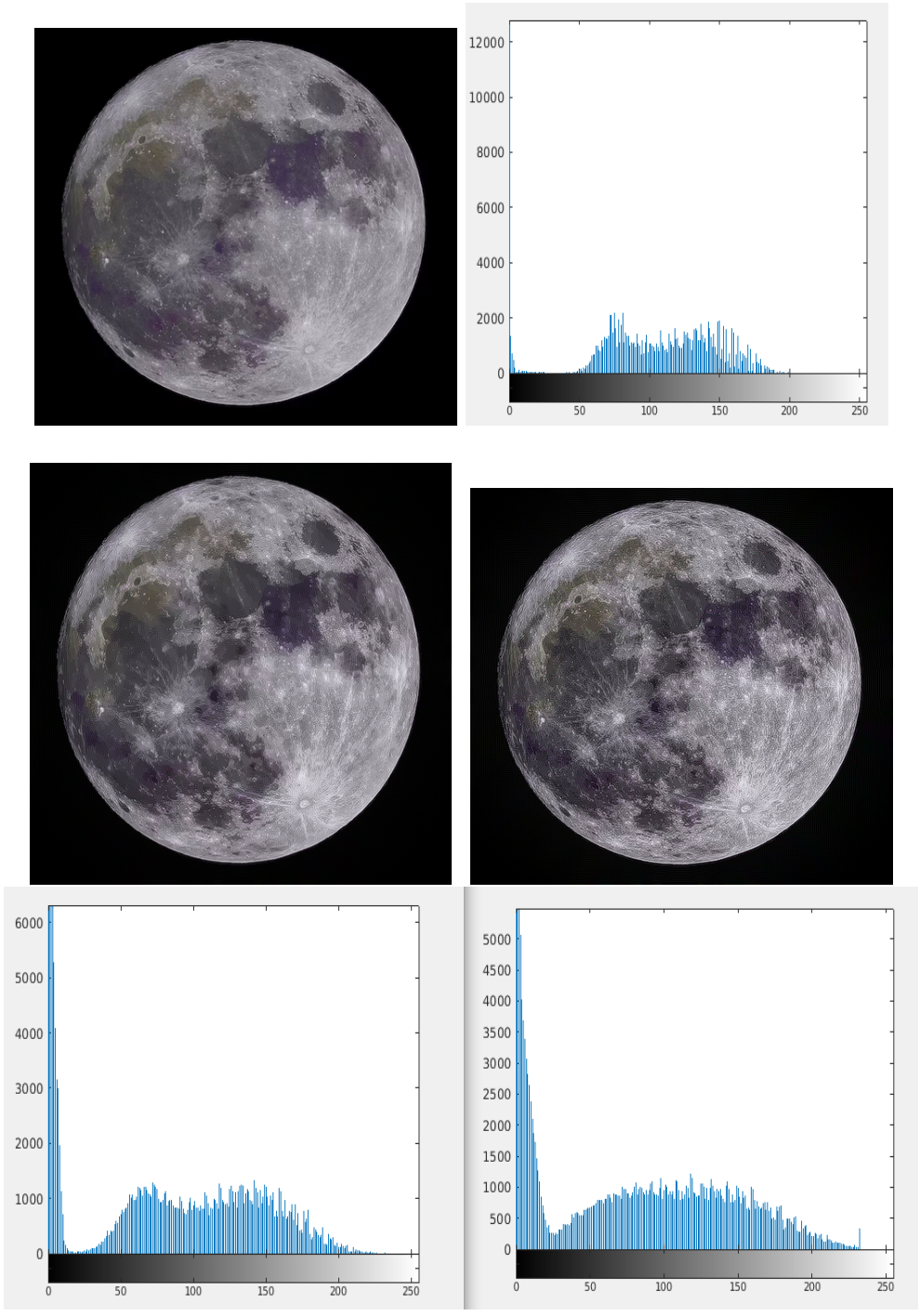


Figure 3.7: Influence of the contrast enhancement scale on the result (from the left to the right): original, $c = 10$ and $window = 5$, $c = 20$ and $window = 5$.

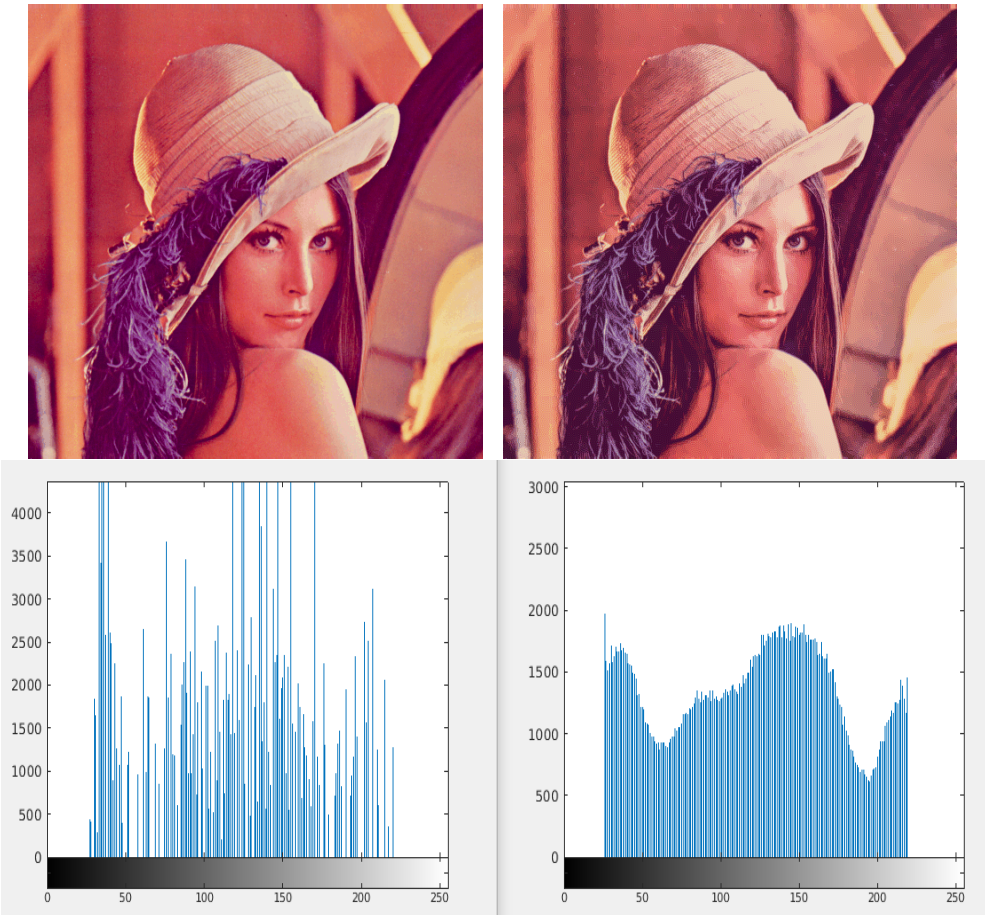


Figure 3.8: Variants of contrast enhancement with the corresponding histograms (from the left to the right): original image, restored image with $c = 10$ and $window = 5$.


Figure 3.9: Variants of contrast enhancement with the corresponding histograms (from the left to the right): original image, restored image with $c = 10$ and $window = 5$.

# Conclusions

In this thesis, a new variational model in Sobolev-Orlicz spaces with non-standard growth conditions of the objective functional is proposed. In particular, some applications are discussed for the simultaneous contrast enhancement and denoising of color images.
It is proved that increasing the average local contrast measure improves the perceived contrast of the image. Sufficient conditions for the convergence of the minimization algorithm are obtained. Finally, an iterative algorithm for practical implementations is considered.
The contrast scale and level in the model are adjustable, so that the proposed approach can be considered as fully adaptive. The enhancement method for color images works directly on the RGB images without any pre- and/or post-processing.
Future research activities aim to the automatic adaptation of the parameters to the content of the considered image, as well as to the development of numerical schemes for the fast computation of restored images.

# Bibliography

[1] Fan, L., Zhang, F., Fan, H., Zhang, C.: Brief review of image denoising techniques. Visual Computing for Industry, Biomedicine, and Art 2, 7, DOI:10.1186/s4249201900167. (2019)

[2] Donoho, D.L., Johnstone I.M.: Ideal spatial adaptation by wavelet shrinkage. Biometrika 81(3):425455. (1994). https://doi.org/10.1093/biomet/81.3.425

[3] Shin, D.H., Park, R.H., Yang, S., Jung, J.H.: Block-based noise estimation using adaptive gaussian filtering. IEEE Trans Consum Electron 51(1):218226. (2005). https://doi.org/10.1109/TCE.2005.1405723

[4] Liu, W., Lin, W.: Additive white Gaussian noise level estimation in SVD domain for images. IEEE Trans Image Process 22(3):872883. (2013). https://doi.org/ 10.1109/TIP.2012.2219544

[5] Diwakar, M., Kumar, M.: A review on CT image noise and its denoising. Biomed Signal Process Control. 42. 73-88. (2018). https://doi.org/10.1016/j.bspc.2018.01.010

[6] Li, X.L., Hu, Y.T., Gao, X.B., Tao, D.C., Ning, B.J.: A multiframe image super-resolution method. Signal Process 90(2):405414. (2010). https://doi.org/10.1016/j.sigpro.2009.05.028

[7] Lebrun, M., Colom, M., Buades, A., Morel, J.M.: Secrets of image denoising cuisine. Acta Numer. 21. 475576. (2012)

[8] Gonzalez, R.C., Woods, R.E.: Image processing. Digit. Image Process. 2. (2007)

[9] Yan, R., Shao, L., Liu, L., Liu, Y.: Natural image denoising using evolved local adaptive filters. Signal Process. 103. 3644. (2014)

[10] Gonzalez, R.C., Woods, R.E.: Digital image processing. 3rd edition. Prentice-Hall, Inc, Upper Saddle River. (2006)

[11] Al-Ameen, Z., Al-Ameen, S., Sulong, G.: Latest methods of image enhancement and restoration for computed tomography: a concise review. Appl Med Inf 36(1):112. (2015)

[12] Jain, A.K.: Fundamentals of digital image processing. Prentice-hall, Inc, Upper Saddle River. (1989)

[13] Benesty, J., Chen, J.D., Huang, Y.T.: Study of the widely linear wiener filter for noise reduction. Abstracts of IEEE international conference on acoustics, speech and signal processing, IEEE, Dallas, TX, USA, pp 205208. (2010). https://doi.org/10.1109/ICASSP.2010.5496033

[14] Pitas, I., Venetsanopoulos, A.N.: Nonlinear digital filters: principles and applications. Kluwer, Boston. (1990). https://doi.org/10.1007/978-1-4757-6017-0

[15] Yang, R., Yin, L., Gabbouj, M., Astola, J., Neuvo, Y.: Optimal weighted median filtering under structural constraints. IEEE Trans Signal Process 43(3):591-604. (1995). https://doi.org/10.1109/78.370615

[16] Tomasi, C., Manduchi, R.: Bilateral filtering for gray and color images. Abstracts of the sixth international conference on computer vision IEEE, Bombay, India, 839846. (1998). https://doi.org/10.1109/ICCV.1998.710815

[17] Katsaggelos, A.K.: Digital image restoration. Springer Publishing Company. Berlin. (2012)

[18] Tikhonov, A.N., Arsenin, V.Y.: Solutions of ill-posed problems. (trans: John F). Wiley, Washington. (1977)

[19] Dobson, D.C., Santosa, F.: Recovery of blocky images from noisy and blurred data. SIAM J Appl Math 56(4):11811198. (1996). https://doi.org/10.1137/S003613999427560X

[20] Nikolova, M.: Local strong homogeneity of a regularized estimator. SIAM J Appl Math 61(2):633658. (2000). https://doi.org/10.1137/ S0036139997327794

[21] Perona, P., Malik, J.: Scale-space and edge detection using anisotropic diffusion. IEEE Trans Pattern Anal Mach Intell. 12 (7). 629-639. (1990). https://doi.org/10.1109/34.56205

[22] Weickert, J.: Anisotropic diffusion in image processing. Teubner, Stuttgart. (1998)

[23] Catté, F., Lions, P.L., Morel, J.M., Coll, T.: Image selective smoothing and edge detection by nonlinear diffusion. SIAM J Numer Anal 29 (1). 182193. 29 (3). 845866 (1992)

[24] Esedo$\bar{g}$lu, S., Osher, S.J.: Decomposition of images by the anisotropic rudin-osher-fatemi model. Commun Pure Appl Math 57(12):16091626. (2004). https://doi.org/10.1002/cpa.20045

[25] Rudin, L.I., Osher, S., Fatemi, E.: Nonlinear total variation based noise removal algorithms. Paper presented at the eleventh annual international conference of the center for nonlinear studies on experimental mathematics: computational issues in nonlinear science. Elsevier North-Holland, Inc, New York, 259268. (1992). https://doi.org/10.1016/0167-2789(92)90242-F

[26] Chambolle, A., Pock, T.: A first-order primal-dual algorithm for convex problems with applications to imaging. J Math Imaging Vis 40(1):120145. (2011). https://doi.org/10.1007/s10851-010-0251-1

[27] Rudin, L.I., Osher, S.: Total variation based image restoration with free local constraints. Abstracts of the 1st international conference on image processing. IEEE, Austin, 3135. (1994)

[28] Bowers, K.L., Lund, J.: Computation and control IV, progress in systems and control theory. Birkhauser, Boston. 323331. (1995). https://doi.org/10.1007/978-1-4612-2574-4

[29] Vogel, C.R., Oman, M.E.: Iterative methods for total variation denoising. SIAM J Sci Comput 17(1):227238. (1996). https://doi.org/10.1137/0917016

[30] Lou, Y.F., Zeng, T.Y., Osher, S., Xin, J.: A weighted difference of anisotropic and isotropic total variation model for image processing. SIAM J Imaging Sci 8(3):17981823. (2015). https://doi.org/10.1137/14098435X

[31] Zibulevsky, M., Elad, M.: L1-L2 optimization in signal and image processing. IEEE Signal Process Mag 27(3):7688. (2010). https://doi.org/10.1109/MSP.2010.936023

[32] Hu, Y., Jacob, M.: Higher degree total variation (HDTV) regularization for image recovery. IEEE Trans Image Process 21(5):25592571. (2012). https://doi.org/10.1109/TIP.2012.2183143

[33] Beck, A., Teboulle, M.: Fast gradient-based algorithms for constrained total variation image denoising and deblurring problems. IEEE Trans Image Process 18(11):24192434. (2009). https://doi.org/10.1109/TIP.2009.2028250

[34] Shao , L., Yan, R., Li, X., Liu, Y.: From heuristic optimization to dictionary learning: a review and comprehensive comparison of image denoising algorithms, IEEE Trans. Cybern. 44 (7). 10011013. (2014)

[35] Shapiro, L., George, C.: Stockman g: Computer Vision. Prentice-Hall. (2001)

[36] Hardie, R.C., Barner, K.E.: Rank conditioned rank selection filters for signal restoration. IEEE Trans. Image Process. 3 (2). (1994)

[37] Dogra, A., Goyal, B., Agrawal, S.: Osseous and digital subtraction angiography image fusion via various enhancement schemes and Laplacian pyramid transformations. Future Gener. Comput. Syst. 82. 149157. (2018)

[38] You, Y.L., Xu, W., Tannenbaum, A., Kaveh, M.: Behavioral analysis of anisotropic diffusion in image processing, IEEE Trans. Image Process. 5 (11). 15391553. (1996)

[39] Scherzer, O., Weickert, J.: Relations between regularization and diffusion filtering. J. Math. Imaging Vis. 12 (1). 4363. (2000)

[40] Osher, S., Rudin, L.I.: Feature-oriented image enhancement using shock filters. SIAM J. Numer. Anal. 27 (4). 458474. (1990)

[41] Alvarez, L., Mazorra, L.: Signal and image restoration using shock filters and anisotropic diffusion, SIAM J. Numer. Anal. 31 (2). 590605. (1994)

[42] Gilboa, G., Sochen, N., Zeevi, Y.Y.: Forward-and-backward diffusion processes for adaptive image enhancement and denoising, IEEE Trans. Image Process. 11 (7). 689703. (2002)

[43] Gilboa, G., Sochen, N., Zeevi, Y.Y.: Image enhancement and denoising by complex diffusion processes. IEEE Trans. Pattern Anal. Mach. Intell. 26 (8). 10201036. (2004)

[44] Qiu, Z., Yang, L., Lu, W.: A new feature-preserving nonlinear anisotropic diffusion for denoising images containing blobs and ridges. Pattern Recognit. Lett. 33 (3). 319330. (2012)

[45] Hajiaboli, M.R.: An anisotropic fourth-order diffusion filter for image noise removal. Int. J. Comput. Vis. 92 (2). 177191. (2011)

[46] Lysaker, M., Lundervold, A., Tai, X.C.: Noise removal using fourth-order partial differential equation with applications to medical magnetic resonance images in space and time. IEEE Trans. Image Process. 12 (12). 15791590. (2003)

[47] Hajiaboli, M.R.: A self-governing hybrid model for noise removal. Pacific-Rim Symposium on Image and Video Technology. 295305. (2009)

[48] Zeng, W., Lu, X., Tan, X.: Non-linear fourth-order telegraph-diffusion equation for noise removal. IET Image Process. 7 (4). 335342. (2013)

[49] You, Y.L., Kaveh, M.: Fourth-order partial differential equations for noise removal. IEEE Trans. Image Process. 9 (10). 17231730. (2000)

[50] Chao, S.M., Tsai, D.M.: An improved anisotropic diffusion model for detail and edge preserving smoothing. Pattern Recognit. Lett. 31 (13). 20122023. (2010)

[51] Chen, D., MacLachlan, S., Kilmer, M.: Iterative parameter choice and multigrid methods for anisotropic diffusion denoising. SIAM J. Sci. Comput. 33 (5). 29722994. (2011)

[52] Yaroslavsky, L., Eden, M.: Fundamentals of Digital Optics: Digital Signal Processing in Optics and Holography. Birkhäuser, Boston. (1996)

[53] Yaroslavsky, L.P.: Digital Picture Processing: An Introduction. Springer Science & Business Media. 9. (2012)

[54] Smith, S.M., Brady, J.M.: SUSAN-a new approach to low level image processing. Int. J. Comput. Vis. 23 (1). 45-78. (1997)

[55] Zhang, M., Gunturk, B.K.: Multiresolution bilateral filtering for image denoising. IEEE Trans. Image Process. 17 (12). 2324-2333. (2008)

[56] Elad, M.: On the origin of the bilateral filter and ways to improve it. IEEE Trans. Image Process. 11 (10). 11411151. (2002)

[57] Chaudhury, K.N., Sage, D., Unser, M.: Fast O(1) bilateral filtering using trigonometric range kernels. IEEE Trans. Image Process. 20 (12). 3376-3382. (2011)

[58] Chaudhury, K.N.: Acceleration of the shiftable O(1) algorithm for bilateral filtering and nonlocal means. IEEE Trans. Image Process. 22 (4). 1291-1300. (2013)

[59] Durand, F., Dorsey, J.: Fast bilateral filtering for the display of high-dynamic-range images. ACM Transactions on Graphics (TOG). 21. 257-266. (2002)

[60] Porikli, F.: Constant Time O(1) Bilateral Filtering. (2008)

[61] Yang, Q., Tan, K.H., Ahuja, N.: Real-time O(1) bilateral filtering. Computer Vision and Pattern Recognition, 2009. CVPR 2009. IEEE Conference 2009. 557564.

[62] Farbman, Z., Fattal, R., Lischinski, D., Szeliski, R.: Edge-preserving decompositions for multi-scale tone and detail manipulation. ACM Transactions on Graphics (TOG), 27. 67. (2008)

[63] Goyal, B., Dogra, A., Agrawal, S., Sohi, B.S.: A three stage integrated denoising approach for grey scale images. J. Ambient Intell. Humaniz. Comput. 116. (2018)

[64] Jin, L., Xiong, C., Liu, H.: Improved bilateral filter for suppressing mixed noise in color images. Digit. Signal Process. 22 (6). 903912. (2012)

[65] Shi, W., Li, J., Wu, M.: An image denoising method based on multiscale wavelet thresholding and bilateral filtering. Wuhan Univ. J. Nat. Sci. 15 (2). 148-152. (2010)

[66] Peng, H., Rao, R., Dianat, S.A.: Multispectral image denoising with optimized vector bilateral filter. IEEE Trans. Image Process. 23 (1). 264273. (2014)

[67] Yu, H., Zhao, L., Wang, H.: Image denoising using trivariate shrinkage filter in the wavelet domain and joint bilateral filter in the spatial domain. IEEE Trans. Image Process. 18 (10). 23642369. (2009)

[68] He, K., Sun, J., Tang, X.: Guided image filtering. European Conference on Computer Vision. 1-14. (2010)

[69] Buades, A., Coll, B., Morel, J.M.: A review of image denoising algorithms, with a new one. Multiscale Model. Simul. 4 (2). 490530. (2005)

[70] Zhang, X., Feng, X., Wang, W.: Two-direction nonlocal model for image denoising. IEEE Trans. Image Process. 22 (1). 408412. (2013)

[71] Mahmoudi, M., Sapiro, G.: Fast image and video denoising via nonlocal means of similar neighborhoods. IEEE Signal Process. Lett. 12 (12). 839842. (2005)

[72] Wang, S., Xia, Y., Liu, Q., Luo, J., Zhu, Y., Feng, D.D.: Gabor feature based nonlocal means filter for textured image denoising. J. Vis. Commun. Image Represent. 23 (7). 10081018. (2012)

[73] Goossens, B., Luong, H., Pizurica, A., Philips, W.: An improved non-local denoising algorithm. International Workshop on Local and Non-Local Approximation in Image Processing (LNLA 2008). 143156. (2008)

[74] Gilboa, G., Osher, S.: Nonlocal operators with applications to image processing. SIAM J Multiscale Model Simul. 7 (3). 10051028. (2009) https://doi.org/10.1137/070698592

[75] Buades, A., Coll, B., Morel, J.M.: A non-local algorithm for image denoising. Abstracts of 2005 IEEE computer society conference on computer vision and pattern recognition. IEEE, San Diego, 6065. (2005). https://doi.org/10.1109/CVPR.2005.38

[76] Coupe, P., Yger, P., Prima, S., Hellier, P., Kervrann, C., Barillot, C.: An optimized blockwise nonlocal means denoising filter for 3-d magnetic resonance images. IEEE Trans Med Imaging. 27 (4). 425441. (2008). https://doi.org/10.1109/TMI.2007.906087

[77] Thaipanich, T., Oh, B.T., Wu, P.H., Xu, D.R., Kuo, C.C.J.: Improved image denoising with adaptive nonlocal means (ANL-means) algorithm. IEEE Trans Consum Electron. 56 (4). 2623-2630. (2010). https://doi.org/10.1109/TCE.2010.5681149

[78] Wang, J., Guo, Y.W., Ying, Y.T., Liu, Y.L., Peng, Q.S.: Fast non-local algorithm for image denoising. Abstracts of 2006 international conference on image processing. IEEE, Atlanta. 1429-1432. (2006). https://doi.org/10.1109/ICIP.2006.312698

[79] Pang, C., Au, O.C., Dai, J.J., Yang, W., Zou, F.: A fast NL-means method in image denoising based on the similarity of spatially sampled pixels. Abstracts of 2009 IEEE international workshop on multimedia signal processing. IEEE, Rio De Janeiro. 1-4. (2009).

[80] Tschumperlé, D., Brun, L.: Non-local image smoothing by applying anisotropic diffusion PDE's in the space of patches. Abstracts of the 16th IEEE international conference on image processing. IEEE, Cairo. 2957-2960. (2009). https://doi.org/10.1109/ICIP.2009.5413453

[81] Grewenig, S., Zimmer, S., Weickert, J.: Rotationally invariant similarity measures for nonlocal image denoising. J Vis Commun Image Represent. 22 (2). 117-130. (2011). https://doi.org/10.1016/j.jvcir.2010.11.001

[82] Fan, L.W., Li, X.M., Guo, Q., Zhang, C.M.: Nonlocal image denoising using edge-based similarity metric and adaptive parameter selection. Sci China Inf Sci. 61 (4):049101. (2018). https://doi.org/10.1007/s11432-017-9207-9

[83] Kheradmand, A., Milanfar, P.: A general framework for regularized, similarity-based image restoration. IEEE Trans Image Process. 23 (12):5136-5151. (2014). https://doi.org/10.1109/TIP.2014.2362059

[84] Fan, L.W., Li, X.M., Fan, H., Feng, Y.L., Zhang, C.M.: Adaptive texture- preserving denoising method using gradient histogram and nonlocal self- similarity priors. IEEE Trans Circuits Syst Video Technol. (2018). https://doi.org/10.1109/TCSVT.2018.2878794

[85] Wei, J.: Lebesgue anisotropic image denoising. Int J Imaging Syst Technol. 15 (1):64-73. (2005). https://doi.org/10.1002/ima.20039

[86] Kervrann, C., Boulanger, J.: Local adaptivity to variable smoothness for exemplar-based image regularization and representation. Int J Comput Vis. 79 (1):45-69. (2008). https://doi.org/10.1007/s11263-007-0096-2

[87] Lou, Y.F., Favaro, P., Soatto, S., Bertozzi, A.: Nonlocal similarity image filtering. Abstracts of the 15th international conference on image analysis and processing. ACM, Vietri sul Mare, 62-71. (2009). https://doi.org/10.1007/978-3-642-04146-4_9

[88] Zimmer, S., Didas, S., Weickert, J.: A rotationally invariant block matching strategy improving image denoising with non-local means. Abstracts of international workshop on local and non-local approximation in image processing. IEEE, Lausanne. 103-113. (2008)

[89] Yan, R.M., Shao, L., Cvetkovic, S.D., Klijn, J.: Improved nonlocal means based on pre-classification and invariant block matching. J Disp Technol. 8 (4):212-218. (2012). https://doi.org/10.1109/JDT.2011.2181487

[90] Dabov, K., Foi, A., Katkovnik, V., Egiazarian, K.: Image denoising by sparse 3-D transform-domain collaborative filtering. IEEE Trans Image Process. 16 (8). 2080-2095. (2007). https://doi.org/10.1109/TIP.2007.901238

[91] Sutour, C., Deledalle, C.A., Aujol, J.F.: Adaptive regularization of the nl-means: application to image and video denoising. IEEE Trans Image Process. 23 (8):35063521. (2014). https://doi.org/10.1109/TIP.2014.2329448

[92] Zoran, D., Weiss, Y.: From learning models of natural image patches to whole image restoration. Abstracts of 2011 international conference on computer vision. IEEE, Barcelona. 479-486. (2011). https://doi.org/10.1109/ICCV.2011.6126278

[93] Gu, S.H., Xie, Q., Meng, D.Y., Zuo, W.M., Feng, X.C., Zhang, L.: Weighted nuclear norm minimization and its applications to low level vision. Int J Comput Vis. 121 (2). 183-208. (2017). https://doi.org/10.1007/s11263-016-0930-5

[94] Gu, S.H., Zhang, L., Zuo, W.M., Feng, X.C.: Weighted nuclear norm minimization with application to image denoising. Abstracts of 2014 IEEE conference on computer vision and pattern recognition. IEEE, Columbus. 2862-2869. (2014). https://doi.org/10.1109/CVPR.2014.366

[95] Xu, S., Zhou, Y., Xiang, H., Li, S.: Remote sensing image denoising using patch grouping-based nonlocal means algorithm. IEEE Geosci. Remote Sens. Lett. 14 (12). 22752279. (2017)

[96] Treece, G.: The bitonic filter: linear filtering in an edge-preserving morphological framework. IEEE Trans. Image Process. 25 (11). 5199-5211. (2016)

[97] Takeda, H., Farsiu, S., Milanfar, P.: Kernel regression for image processing and reconstruction. IEEE Trans Image Process. 16 (2). 349-366. (2007). https://doi.org/10.1109/TIP.2006.888330

[98] Zhang, K.B., Gao, X.B., Tao, D.C., Li, X.L.: Multi-scale dictionary for single image super-resolution. Abstracts of 2012 IEEE conference on computer vision and pattern recognition. IEEE, Providence. 1114-1121. (2012). https://doi.org/10.1109/CVPR.2012.6247791

[99] Aharon, M., Elad, M., Bruckstein, A.: rmK-SVD: an algorithm for designing overcomplete dictionaries for sparse representation. IEEE Trans Signal Process. 54 (11). 4311-4322. (2006). https://doi.org/10.1109/TSP.2006.881199

[100] Elad, M., Aharon, M.: Image denoising via sparse and redundant representations over learned dictionaries. IEEE Trans Image Process. 15 (12). 37363745. (2006). https://doi.org/10.1109/TIP.2006.881969

[101] Zhang, L., Zuo, W.M.: Image restoration: from sparse and low-rank priors to deep priors [lecture notes]. IEEE Signal Process Mag. 34 (5). 172179. (2017). https://doi.org/10.1109/MSP.2017.2717489

[102] Mairal, J., Bach, F., Ponce, J., Sapiro, G., Zisserman, A.: Non-local sparse models for image restoration. Abstracts of the 12th international conference on computer vision. IEEE, Kyoto. 2272-2279. (2009). https://doi.org/10.1109/ICCV.2009.5459452

[103] Zhang, L., Dong, W.S., Zhang, D., Shi, G.M.: Two-stage image denoising by principal component analysis with local pixel grouping. Pattern Recogn. 43 (4). 1531-1549. (2010). https://doi.org/10.1016/j.patcog.2009.09.023

[104] Dong, W.S., Zhang, L., Shi, G.M., Li, X.: Nonlocally centralized sparse representation for image restoration. IEEE Trans Image Process. 22 (4). 1620-1630. (2013). https://doi.org/10.1109/TIP.2012.2235847

[105] Markovsky, I.: Low rank approximation: algorithms, implementation, applications. Springer Publishing Company. Berlin. (2011)

[106] Liu, G.C., Lin, Z.C., Yu, Y.: Robust subspace segmentation by low-rank representation. Abstracts of the 27th international conference on machine leaning. ACM. Haifa. 663-670. (2010)

[107] Ji, H., Liu, C.Q., Shen, Z.W., Xu, Y.H.: Robust video denoising using low rank matrix completion. Abstracts of 2010 IEEE computer vision and pattern recognition. IEEE, San Francisco. 17911798. (2010). https://doi.org/10.1109/CVPR.2010.5539849

[108] Ji, H., Huang, S.B., Shen, Z.W., Xu, Y.H.: Robust video restoration by joint sparse and low rank matrix approximation. SIAM J Imaging Sci. 4 (4). 1122-1142. (2011). https://doi.org/10.1137/100817206

[109] Liu, X.Y., Ma, J., Zhang, X.M., Hu, Z.Z.: Image denoising of low-rank matrix recovery via joint frobenius norm. J Image Graph. 19 (4). 502-511. (2014)

[110] Yuan, Z., Lin, X.B., Wang, X.N.: The LSE model to denoise mixed noise in images. J Signal Process. 29 (10). 1329-1335. (2013)

[111] Dong, W.S., Shi, G.M., Li, X.: Nonlocal image restoration with bilateral variance estimation: a low-rank approach. IEEE Trans Image Process. 22 (2). 700-711. (2013). https://doi.org/10.1109/TIP.2012.2221729

[112] Eriksson, A., van den Hengel, A.: Efficient computation of robust weighted low-rank matrix approximations using the L1 norm. IEEE Trans Pattern Anal Mach Intell. 34 (9). 1681-1690. (2012). https://doi.org/10.1109/TPAMI.2012.116

[113] Liu, R.S., Lin, Z.C., De la Torre, F.: Fixed-rank representation for unsupervised visual learning. Abstracts of 2012 IEEE conference on computer vision and pattern recognition. IEEE, Providence. 598-605. (2012)

[114] Bertalmío, M.: Denoising of photographic images and video: fundamentals, open challenges and new trends. Springer Publishing Company, Berlin. (2018) https://doi.org/10.1007/978-3-319-96029-6

[115] Guo, Q., Zhang, C.M., Zhang, Y.F., Liu, H.: An efficient SVD-based method for image denoising. IEEE Trans Circuits Syst Video Technol. 26. 868-880. (2016) https://doi.org/10.1109/TCSVT.2015.2416631

[116] Liu, G.C., Lin, Z.C., Yan, S.C., Sun, J., Yu, Y., Ma, Y.: Robust recovery of subspace structures by low-rank representation. IEEE Trans Pattern Anal Mach Intell. 35 (1). 171-184. (2013). https://doi.org/10.1109/TPAMI.2012.88

[117] Cai, J.F., Candès, E.J., Shen, Z.W.: A singular value thresholding algorithm for matrix completion. SIAM J Optim. 20 (4). 1956-1982. (2010). https://doi.org/10.1137/080738970

[118] Hou, J.H.: Research on image denoising approach based on wavelet and its statistical characteristics. Dissertation, Huazhong University of Science and Technology. (2007)

[119] Jiao, L.C., Hou, B., Wang, S., Liu, F.: Image multiscale geometric analysis: theory and applications. Xidian University press, Xi'an. (2008)

[120] Zhang, L., Bao, P., Wu, X.L.: Multiscale lmmse-based image denoising with optimal wavelet selection. IEEE Trans Circuits Syst Video Technol. 15 (4). 469-481. (2005). https://doi.org/10.1109/TCSVT.2005.844456

[121] Xiong, Z., Ramchandran, K., Orchard, M.T., Zhang, Y.Q.: A comparative study of DCT-and wavelet-based image coding. IEEE Trans. Circuits Syst. Video Technol. 9 (5). 692-695. (1999)

[122] Mallat, S.: A Wavelet Tour of Signal Processing. Elsevier. (1999)

[123] Misiti, M., Misiti, Y., Oppenheim, G., Michel, J.P.: Wavelet Toolbox: For Use With Matlab. (1996)

[124] Mallat, S.G.: A theory for multiresolution signal decomposition: the wavelet representation. IEEE Trans. Pattern Anal. Mach. Intell. 11 (7). 674-693. (1989)

[125] Jain, P., Tyagi, V.: Spatial and frequency domain filters for restoration of noisy images. IETE J Educ. 54 (2). 108-116. (2013). https://doi.org10.1080/09747338.2013.10876113

[126] Hamza, A.B., Luque-Escamilla, P.L., Martínez-Aroza, J., Román-Roldán, R.: Removing noise and preserving details with relaxed median filters. J Math Imaging Vis. 11 (2). 161-177. (1999). https://doi.org/10.1023/A:1008395514426

[127] Choi, H., Baraniuk, R.: Analysis of wavelet-domain wiener filters. Abstracts of IEEE-SP international symposium on time-frequency and time-scale analysis. IEEE, Pittsburgh. 613-616. (1998). https://doi.org/10.1109/TFSA.1998.721499

[128] Combettes, P.L., Pesquet, J.C.: Wavelet-constrained image restoration. Int J Wavelets Multiresolution Inf Process. 2 (4). 371-389. (2004). https://doi.org/10.1142/S0219691304000688

[129] da Silva, R.D., Minetto, R., Schwartz, W.R., Pedrini, H.: Adaptive edge-preserving image denoising using wavelet transforms. Pattern Anal Applic. 16 (4). 567-580. (2013). https://doi.org/10.1007/s10044-012-0266-x

[130] Malfait, M., Roose, D.: Wavelet-based image denoising using a markov random field a priori model. IEEE Trans Image Process. 6 (4). 549-565. (1997). https://doi.org/10.1109/83.563320

[131] Portilla, J., Strela, V., Wainwright, M.J., Simoncelli, E.P.: Image denoising using scale mixtures of gaussians in the wavelet domain. IEEE Trans Image Process. 12 (11). 1338-1351. (2003). https://doi.org/10.1109/TIP.2003.818640

[132] Strela, V.: Denoising via block wiener filtering in wavelet domain. Abstracts of the 3rd European congress of mathematics. Birkhäuser, Barcelona. 619-625. (2001). https://doi.org/10.1007/978-3-0348-8266-8_55

[133] Yao, X.B.: Image denoising research based on non-local sparse models with low-rank matrix decomposition. Dissertation, Xidian University. (2014)

[134] Hou, Y., Zhao, C., Yang, D., Cheng, Y.: Comments on image denoising by sparse 3-D transform-domain collaborative filtering. IEEE Trans. Image Process. 20 (1). 268-270. (2011)

[135] Chen, Y.Y., Pock, T.: Trainable nonlinear reaction diffusion: a flexible framework for fast and effective image restoration. IEEE Trans Pattern Anal Mach Intell. 39 (6). 1256-1272. (2017). https://doi.org/10.1109/TPAMI.2016.2596743

[136] Schmidt, U., Roth, S.: Shrinkage fields for effective image restoration. Abstracts of 2014 IEEE conference on computer vision and pattern recognition. IEEE, Columbus. 2774-2781. (2014). https://doi.org/10.1109/CVPR.2014.349

[137] Kim, J., Lee, J.K., Lee, K.M.: Accurate image super-resolution using very deep convolutional networks. Abstracts of 2016 IEEE conference on computer vision and pattern recognition. IEEE, Las Vegas. 1646-1654. (2016). https://doi.org/10.1109/CVPR.2016.182

[138] Nah, S., Kim, T.H., Lee, K.M.: Deep multi-scale convolutional neural network for dynamic scene deblurring. Abstracts of 2017 IEEE conference on computer vision and pattern recognition. IEEE, Honolulu. 257-265. (2017). https://doi.org/10.1109/CVPR.2017.35

[139] Jain, V., Seung, H.S.: Natural image denoising with convolutional networks. Abstracts of the 21st international conference on neural information processing systems. ACM, Vancouver. 769-776. (2008)

[140] Vincent, P., Larochelle, H., Bengio, Y., Manzagol, P.A.: Extracting and composing robust features with denoising autoencoders. Abstracts of the 25th international conference on machine learning. ACM, Helsinki. 1096-1103. (2008). https://doi.org/10.1145/1390156.1390294

[141] Xie, J.Y., Xu, L.L., Chen, E.H.: Image denoising and inpainting with deep neural networks. Abstracts of the 25th international conference on neural information processing systems. Volume 1. ACM, Lake Tahoe. 341-349. (2012)

[142] Zhang, K., Zuo, W.M., Chen, Y.J., Meng, D.Y., Zhang, L.: Beyond a Gaussian denoiser: residual learning of deep CNN for image denoising. IEEE Trans Image Process. 26 (7). 3142-3155. (2017). https://doi.org/10.1109/TIP.2017.2662206

[143] Zhang, K., Zuo, W.M., Zhang, L.: FFDNet: toward a fast and flexible solution for CNN-based image denoising. IEEE Trans Image Process. 27 (9). 4608-4622. (2018). https://doi.org/10.1109/TIP.2018.2839891

[144] Cruz, C., Foi, A., Katkovnik, V., Egiazarian, K.: Nonlocality-reinforced convolutional neural networks for image denoising. IEEE Signal Process Lett. 25 (8). 1216-1220. (2018). https://doi.org/10.1109/LSP.2018.2850222

[145] Yang, H.Y., Wang, X.Y., Niu, P.P., Liu, Y.C.: Image denoising using nonsubsampled shearlet transform and twin support vector machines. Neural Netw. 57. 152-165. (2014)

[146] Dogra, A., Agrawal, S., Goyal, B.: Efficient representation of texture details in medical images by fusion of Ripplet and DDCT transformed images. Trop. J. Pharm. Res. 15 (9). 1983-1993. (2016)

[147] Dogra, A., Goyal, B., Agrawal, S.: Bone vessel image fusion via generalized Reisz wavelet transform using averaging fusion rule. J. Comput. Sci. 21. 371-378. (2017)

[148] Dogra, A., Agrawal, S., Goyal, B., Khandelwal, N., Ahuja, C.K.: Color and grey scale fusion of osseous and vascular information. J. Comput. Sci. 17. 103-114. (2016)

[149] Dogra, A., Agrawal, S., Khandelwal, N., Ahuja, C.: Osseous and vascular information fusion using various spatial domain filters. Asian J. Res. Chem. 9 (7). 937. (2016)

[150] Goyal, B., Agrawal, S., Sohi, B.S., Dogra, A.: Noise reduction in MR brain image via various transform domain schemes. Asian J. Res. Chem. 9 (7). 919. (2016)

[151] Dogra, A., Goyal, B., Agrawal, S.: From multi-scale decomposition to non-multi-scale decomposition methods: a comprehensive survey of image fusion techniques and its applications. IEEE Access. 5. 16040-16067. (2017)

[152] Yadav, J., Dogra, A., Goyal, B., Agrawal, S.: A review on image fusion methodologies and applications. Res. J. Pharm. Technol. 10 (4). 1239. (2017)

[153] Goyal, B., Dogra, A., Agrawal, S., Sohi, B.S.: Dual way residue noise thresholding along with feature preservation. Pattern Recognit. Lett. 94. 194-201. (2017)

[154] Dogra, A., Kadry, S., Goyal, B., Agrawal, S.: An efficient image integration algorithm for night mode vision applications. MultimedIS Tools Appl. 1-18. (2018)

[155] Dogra, A., Goyal, B., Agrawal, S.: Current and future orientation of anatomical and functional imaging modality fusion. Biomed. Pharmacol. J. 10 (4). 1661-1663. (2017)

[156] Dogra, A., Patterh, M.S.: CT and MRI brain images registration for clinical applications. J. Cancer Sci. Ther. 6. 018-026. (2014)

[157] Dogra, A., Bhalla, P.: CT and MRI brain images matching using ridgeness correlation. Biomed. Pharmacol. J. 7 (2). 20. (2014)

[158] Kumar, R.: (2010). https://in.mathworks.com/matlabcentral/fileexchange/28112-diffusion-filtering-for-image-denoising

[159] Chaudhury, K.N., Rithwik, K.: Image denoising using optimally weighted bilateral filters: a sure and fast approach. Image Processing (ICIP). IEEE International Conference. 108-112. (2015)

[160] Weiss, Y., Freeman, W.T.: What makes a good model of natural images? IEEE Conference on Computer Vision and Pattern Recognition. 1-8. June. (2007)

[161] Chambolle, A., Caselles, V., Cremers, D., Novaga, M., Pock, T.: An introduction to total variation for image analysis. Theor. Found. Numer. Methods Sparse Recov. 9. 263-340. 227. (2010)

[162] Liu, Q., Xiong, B., Zhang, M.: Adaptive sparse norm and nonlocal total variation methods for image smoothing. Math. Probl. Eng. (2014)

[163] Donoho, D.L., Johnstone, I.M.: Adapting to unknown smoothness via wavelet shrinkage. J. Am. Stat. Assoc. 90 (432). 12001224. (1995)

[164] Donoho, D.L., Johnstone, I.M.: Threshold selection for wavelet shrinkage of noisy data. Proceedings of 16th Annual International Conference of the IEEE Engineering in Medicine and Biology Society. 1. A24-A25. (1994)

[165] Luisier, F., Blu, T., Unser, M.: A new sure approach to image denoising: interscale orthonormal wavelet thresholding, IEEE Trans. Image Process. 16 (3). 593-606. (2007)

[166] Easley, G., Labate, D., Lim, W.Q.: Sparse directional image representations using the discrete shearlet transform. Appl. Comput. Harmon. Anal. 25 (1). 25-46. (2008)

[167] Rangarajan, A., Chellappa, R.: Markov random field models in image processing. M.A. Arbib (Ed.). The Handbook of Brain Theory and Neural Networks. 564-567. (1995)

[168] Takeda, H., Farsiu, S., Milanfar, P.: Deblurring using regularized locally adaptive kernel regression. IEEE Trans. Image Process. 17 (4). 550-563. (2008)

[169] Burger, H.C., Schuler, C.J., Harmeling, S.: Image denoising: can plain neural networks compete with BM3D? IEEE Conference on Computer Vision and Pattern Recognition. 2392-2399. (2012)

[170] Dabov, K., Foi, A., Katkovnik, V., Egiazarian, K.: Joint image sharpening and denoising by 3D transform-domain collaborative filtering. Proc. Int. TICSP Workshop Spectral Meth. Multirate Signal Process., SMMSP. Citeseer. (2007)

[171] Dabov, K., Foi, A., Katkovnik, V., Egiazarian, K.: BM3D image denoising with shape-adaptive principal component analysis. SPARS'09-Signal Processing with Adaptive Sparse Structured Representations. (2009)

[172] Deledalle, C.A., Salmon, J., Dalalyan, A.S.: Image denoising with patch based PCA: local versus global. BMVC. 81. 425-455. (2011)

[173] Kumar, B.S.: Image denoising based on gaussian/bilateral filter and its method noise thresholding. Signal Image Video Process. 6 (7). 1159-1172. (2013)

[174] Kumar, B.S.: Image denoising based on non-local means filter and its method noise thresholding, Signal Image Video Process. 7 (6). 1211-1227. (2013)

[175] Yang, X., Fei, B.: A wavelet multiscale denoising algorithm for magnetic resonance (MR) images. Meas. Sci. Technol. 22 (2). 025803. (2011)

[176] Kumar, M., Diwakar, M.: CT image denoising using locally adaptive shrinkage rule in tetrolet domain. J. King Saud Univ. Comput. Inf. Sci. 30 (1). 41-50. (2018)

[177] Jian, S., Wen, W.: Study on underwater image denoising algorithm based on wavelet transform. 806. 012006. DOI:10.1088/1742-6596/806/1/012006. (2017)

[178] Sharmila, T.S., Ramar, K.: Efficient analysis of hybrid directional lifting technique for satellite image denoising. Signal Image Video Process. 8 (7). 1399-1404. (2014)

[179] Liu, S., Liu, M., Li, P., Zhao, J., Zhu, Z., Wang, X.: SAR image denoising via sparse representation in shearlet domain based on continuous cycle spinning. IEEE Trans. Geosci. Remote Sens. 55 (5). 2985-2992. (2017)

[180] Shen, Y., Chen, Y., Liu, Q., Lou, S., Yu, W., Wang, X., Chen, H.: Improved anscombe transformation and total variation for denoising of lowlight infrared images. Infrared Phys Technol. 93. 192-198. (2018)

[181] Geman, S., Geman, D.: Stochastic relaxation, Gibbs distributions, and the Bayesian restoration of images. IEEE Trans. Pattern Anal. Machine Intell. 6. 721-41. (1984)

[182] Mumford, D., Shah, J.: Optimal approximations by piecewise smooth functions and associated variational problems. Comm. Pure Applied. Math. 42. 577-685. (1989)

[183] Crandall, M.G., Ishii, H., Lions, P.L.: User's guide to viscosity solutions of second order partial linear differential equations, Bull. Amer. Math. Soc. (N.S.) 27. 1-67. (1992)

[184] Manjón, J.V., Coupe, P.: MRI denoising using deep learning. Patch-Based Techniques in Medical Imaging: 4th International Workshop. Patch-MI 2018. Held in Conjunction with MICCAI 2018. Granada, Spain. September 20, 2018. Proceedings 4. 12-19. Springer International Publishing

[185] Gondara, L., Wang, K.: Mida: Multiple imputation using denoising autoencoders. Advances in Knowledge Discovery and Data Mining: 22nd Pacific-Asia Conference, PAKDD 2018, Melbourne, VIC, Australia. June 3-6, 2018, Proceedings, Part III 22. 260-272. Springer International Publishing

[186] Tassano, M., Delon, J., Veit, T.: Dvdnet: A fast network for deep video denoising. IEEE International Conference on Image Processing (ICIP). 1805-1809. (2019)

[187] Davy, A., Ehret, T., Morel, J.M., Arias, P., Facciolo, G.: A non-local CNN for video denoising. IEEE International Conference on Image Processing (ICIP). 2409-2413. (2019)

[188] Liu, P., Basha, E., Li, M.D., Xiao, Y., Sanelli, Y., Fang, R.: Deep evolutionary networks with expedited genetic algorithms for medical image denoising. Med Image Anal. 54. 306-315. (2019)

[189] Mumford, D., Shah, J.: Optimal approximation by piecewise smooth functions and associated variational problems. Commun. Pure Appl. Math. 42. 577685. (1989)

[190] Lysaker, M., Osher, S., Tai, X.C.: Noise removal using smoothed normals and surface fitting. IEEE Trans. Image Proc. 13 (10). 3451457. (2004)

[191] Zhu, W., Chan, T.F.: Image denoising using mean curvature. SIAM J. Imaging Sci. 5. 1-32. (2012)

[192] Brito, C., Chen, K.: Multigrid algorithm for high order denoising. SIAMJ. ImagingSci. 3 (3). 363389. (2010)

[193] Bonettini, S., Landi, G., Loli Piccolomini, E., Zanni, L.: Scaling techniques for gradient projection-type methods in astronomical image deblurring. Int. J. Comput. Math.. 90 (1). 929. (2013)

[194] Yan, M.: Convergence analysis of SART: Optimization and statistics. Int. J. Comput. Math.. 90 (1). 3047. (2013)

[195] Wang, F., Ng, M.K.: A fast minimization method for blur and multiplicative noise removal. Int. J. Comput. Math.. 90 (1). 4861. (2013)

[196] Häuser, S., Steidl, G.: Convex multiclass segmentation with Shearlet regularization. Int. J. Comput. Math.. 90 (1). 6281. (2013)

[197] Barendt, S., Modersitzki, J.: A variational model for SPECT reconstruction with a nonlinearly transformed attenuation prototype. Int. J. Comput. Math.. 90 (1). 8291. (2013)

[198] Brito-Loeza, C., Chen, K.: Fast iterative algorithms for solving the minimization of curvature-related functionals in surface fairing. Int. J. Comput. Math.. 90 (1). 92108. (2013)

[199] Tasdizen, T., Whitaker, R., Burchard, P., Osher, S.: Geometric surface processing via normal maps. ACM Trans. Graph.. 22 (4). 10121033. (2003)

[200] Droske, M., Rumpf, M.: A level set formulation for Willmore flow. Interfaces Free Bound. 6 (3). 361378. (2004)

[201] Elsey, M., Esedo$\bar{g}$lu, S.: Analogue of the total variation denoising model in the context of geometry processing. Multiscale Model. Simul.. 7 (4). 15491573. (2009)

[202] Bredies, K., Dong, Y., Hintermüller, M.: Spatially dependent regularization parameter selection in total generalized variation models for image restoration. Int. J. Comput. Math.. 90 (1). 109123. (2013)

[203] Chumchob, N., Chen, K., Brito-Loeza, C.: A new variational model for removal of combined additive and multiplicative noise and a fast algorithm for its numerical approximation. Int. J. Comput. Math.. 90 (1). 140161. (2013)

[204] Jin, Z., Yang, X.: Analysis of a new variational model for multiplicative noise removal. J. Math. Anal. Appl. 362:415426. (2010)

[205] Irony, R., Cohen-Or, D., Lischinski, D.: Colorization by example. Proceedings of the Sixteenth Eurographics Conference on Rendering Techniques, EGSR 2005. Switzerland. Eurographics Association. 201-210. (2005)

[206] Levin, A., Lischinski, D., Weiss, Y.: Colorization using optimization. ACM Trans. Graph.. 23. 689-694. (2004)

[207] Sapiro, G.: Inpainting the colors. ICIP 2005. IEEE International Conference on Image Processing. 60. 698-701. (2005)

[208] Sapiro, G., Yatziv, L.: Fast image and video colorization using chrominance blending. IEEE Trans. Image Process. 15. 1120-1129. (2006)

[209] Sýkora, D., Buriánek, J., Zára, J.: Unsupervised colorization of black-and-white cartoons. Proceedings of the 3rd International Symposium on Non-photorealistic Animation and Rendering, NPAR 2004. New York. NY. USA. ACM. 121-127. (2004)

[210] Muller, M.U., Shepherd, J.D., Dymond, J.R.: Support vector machine classification of woody patches in New Zealand from synthetic aperture radar and optical data, with LiDAR training. J. Appl. Remote Sens. 9 (1). Id: 095984. (2015)

[211] Garkusha, I.N., Hnatushenko, V.V., Vasyliev, V.V.: Research of influence of atmosphere and humidity on the data of radar imaging by Sentinel-1. IEEE 37th International Conference on Electronics and Nanotechnology (ELNANO). DOI:10.1109/elnano.2017.7939787. (2017)

[212] Garkusha, I.N., Hnatushenko, V.V., Vasyliev, V.V.: Using Sentinel-1 data for monitoring of soil moisture. IEEE International Geoscience and Remote Sensing Symposium (IGARSS). DOI:10.1109/igarss.2017.8127291. (2017)

[213] Saradjian, M.R., Hosseini, M.: Comparison of optical, radar and hybrid soil moisture estimation models using experimental data. J. Appl. Remote Sens. 5 (1). Id: 053524. (2011)

[214] Hnatushenko, V.V., Kogut, P.I., Uvarow, M.V.: Variational Approach for Rigid Co-Registration of Optical/SAR Satellite Images in Agricultural Areas. Journal of Computational and Applied Mathematics. 400. Id: 113742. (2022)

[215] Antil, H., Rautenberg, C.N.: Sobolev spaces with non-Muckenhoupt weights, fractional elliptic operators, and applications. SIAM Journal on Mathematical Analysis. 51 (3). 2479-2503. (2019)

[216] Blomgren, P.: Total variation methods for restoration of vector valued images. Ph.D. Thesis. 384-387. (1998)

[217] Blomgren, P., Chan, T.F., Mulet, P., Wong, C.: Total variation image restoration: Numerical methods and extensions. Proceedings of the 1997 IEEE International Conference on Image Processing. 384-387. III (1997)

[218] Bungert, L., Coomes, D.A., Ehrhardt, M.J., Rasch, J., Reisenhofer, R., Schönlieb, R. & C.B.: Blind image fusion for hyperspectral imaging with the directional total variation. Inverse Problems. 34 (4). (2018)

[219] Bungert, L., Ehrhardt, M.J.: Robust Image Reconstruction with Misaligned Structural Information. IEEE Access. 8. 222944-222955. (2020)

[220] Chen, Y., Levine, S., Rao, M.: Variable exponent, linear growth functionals in image restoration. SIAM Journal Appl. Math. 66 (4). 1383-1406. (2006)

[221] Antil, H., Bartels, S.: Spectral approximation of fractional PDEs in image processing and phase field modeling. Computational Methods in Applied Mathematics. 17 (4). 661-678. (2017)

[222] Roncal, L., Stinga, P.R.: Fractional Laplacian on the torus. Commun. Contemp. Math.. 18 (3). Id: 1550033. (2016)

[223] Caffarelli, L., Silvestre, L.: An extension problem related to the fractional Laplacian. Comm. Part. Diff. Eqs.. 32 (7-9). 767-907. (2016)

[224] Stinga, P.R., Torrea, J.L.: Extension problem and Harnack's inequality for some fractional operators. Comm. Part. Diff. Eqs.. 35 (11). 2092-2122. (2010)

[225] Goyal, B., Dogra, A., Agrawal, S., Sohi, B.S., Sharma, A.: Image denoising review: From classical to state-of-the-art approaches. Information Fusion. 55. 220-244. (2020)

[226] Gao, F., Masek, J., Schwaller, M., Hall, F.: On the blending of the Landsat and MODIS surface reflectance: Predicting daily Landsat surface reflectance. IEEE Trans. Geosci. Remote Sens.. 44 (8). 2207-2218. (2006)

[227] Wang, P., Gao, F., Masek, J.G.: Operational data fusion framework for building frequent Landsat-like imagery. IEEE Trans. Geosci. Remote Sens.. 52 (11). 7353-7365. (2014)

[228] Filgueiras, R., Mantovani, E.C., Fernandes-Filho, E.I., da Cunha, F.F., Althoff, D., Dias, S.H.B.: Fusion of MODIS and Landsat-Like Images for Daily High Spatial Resolution NDVI. Remote Sens.. 2 (8). 1297. (2020)

[229] Ju, J., Roy, D.P.: The availability of cloud-free Landsat ETM+ date over the conterminous united states and globally. Remote Sens. Environ.. 112 (3). 1196-1211. (2008)

[230] Kogut, P.I., Kupenko, O.P., Uvarov, N.V.: On increasing of resolution of satellite images via their fusion with imagery at higher resolution. J. of Optimization. Differential Equations and Their Applications. 29 (1). 54-78. (2021)

[231] Hilker, T., Wulder, M.A., Coops, N.C., Linke, J., McDermid, G., Masek, J.G., Gao, F., White, J.C.: A new data fusion model for high spatial and temporal resolution mapping of forest disturbance based on Landsat and MODIS. Remote Sens. Environ.. 113 (8). 1613-1627. (2009)

[232] Masek, J.G., Vermote, E.F., Saleous, N.E., Wolfe, R., Hall, F.G., Huemmrich, F., Gao, F., Kutler, J., Lim, T.K.: A Landsat surface reflectance data set for North American, 19902000. IEEE Geosci. Remote Sens. Lett.. 3 (1). 69-72. (2006)

[233] Rustanto, A., Booij, M.J.: Evaluation of MODIS-Landsat and AVHRR-Landsat NDVI data fusion using a single pair base reference image: a case study in a tropical upstream catchment on Java, Indonesia. Int. J. Digit. Earth 15. 164-197. (2022)

[234] Loncan, L., De Almeida, L.B., Bioucas-Dias, J.V., Briottet, X., Chanussot, J., Dobigeon, N., Fabre, S., Liao, W., Licciardi, G.A., Simoes, M., Tourneret, J.Y., Veganzones, M.A., Vivone, G., Wei, Q., Yokoya, N.: Hyperspectral pansharpening: a review. IEEE Geoscience and Remote Sensing Magazine. 3 (3). 27-46. (2015)

[235] Horn, B.K., Schunck, B.G.: Determining optical flow. Artificial Intelligence. 17. 185-203. (1981)

[236] Hinterberger, W., Scherzer, O.: Models for image interpolation based on the optical flow. Computing. 66 (3). 231-247. (2001)

[237] Chen, K., Lorenz, D.: Image sequence interpolation using optimal control. J. Math. Imaging Vis.. 41 (3). 222-238. (2011)

[238] Borz'i, A., Ito, K., Kunish, K.: Optimal control formulation for determining optical flow. SIAM J. Sci. Comput.. 24 (3). 818-847. (2002)

[239] Kogut, P.I., Manzo, R.: On vector-valued approximation of state constrained optimal control problems for nonlinear hyperbolic conservation laws. J. Dyn. Control Syst.. 19 (2). 381-404. (2013)

[240] Ballester, C., Caselles, V., Igual, L., Verdera, J., Rougé, B.: A Variational Model for P+XS Image Fusion. Int. J. Comput. Vision. 6. 43-58. (2006)

[241] Laine, A., Fan, J., Yang, W.: Wavelets for contrast enhancement of digital mammography. IEEE Engineering in Medicine and Biology Magazine. 14 (5). 536-550. (1995)

[242] Mignotte, M.: An energy-based model for the image edge-histogram specification problem. IEEE Transactions on Image Processing. 21 (1). 379386. (2012)

[243] Sapiro, G., Caselles, V.: Histogram modification via differential equations. Journal of Differential Equations. 135 (2). 238268. (1997)

[244] Sun, C.C., Ruan, S.J., Shie, M.C., Pai, T.W.: Dynamic contrast enhancement based on histogram specification. IEEE Transactions on Consumer Electronics. 51 (4). 13001305. (2005)

[245] Wang, C., Ye, Z.: Brightness preserving histogram equalization with maximum entropy: a variational perspective. IEEE Transactions on Consumer Electronics. 51 (4). 13261334. (2005)

[246] Arici, T., Dikbas, S., Altunbasak, Y.: A histogram modification framework and its application for image contrast enhancement. IEEE Transactions on Image Processing. 18 (9). 19211935. (2009)

[247] Kim, Y.T.: Contrast enhancement using brightness preserving bi-histogram equalization. IEEE Transactions on Consumer Electronics. 43 (1). 18. (1997)

[248] Chen, S.D., Ramli, A.R.: Contrast enhancement using recursive mean separate histogram equalization for scalable brightness preservation. IEEE Transactions on Consumer Electronics. 49 (4). 1301-1309. (2003)

[249] Sim, K., Tso, C., Tan, Y.: Recursive sub-image histogram equalization applied to gray scale images. Pattern Recognition Letters. 28 (10). 1209-1221. (2007)

[250] Abdullah-Al-Wadud, M., Kabir, M.H., Dewan, M., Chae, O.: A dynamic histogram equalization for image contrast enhancement. IEEE Transactions on Consumer Electronics. 53 (2). 593-600. (2007)

[251] Celik, T., Tjahjadi, T.: Automatic image equalization and contrast enhancement using gaussian mixture modeling. IEEE Transactions on Image Processing. 21 (1). 145-156. (2012)

[252] Celik, T.: Two-dimensional histogram equalization and contrast enhancement. Pattern Recognition. 45 (10). 3810-3824. (2012)

[253] Celik, T., Tjahjadi, T.: Contextual and variational contrast enhancement. IEEE Transactions on Image Processing. 20 (12). 3431-3441. (2011)

[254] Hummel, R.: Image enhancement by histogram transformation. Computer graphics and image processing. 6 (2). 184-195. (1977)

[255] Maini, R., Aggarwal, H.: A comprehensive review of image enhancement techniques. Journal of Computing. 2 (3). 919-940. (2010)

[256] Kaur, M., Kaur, J., Kaur, J.: Survey of contrast enhancement techniques based on histogram equalization. International Journal of Advanced Computer Science and Applications. 2 (7). 137-141. (2011)

[257] Chan, R., Nikolova, M., Wen, Y.W.: A variational approach for exact histogram specification. Scale Space and Variational Methods in Computer Vision. 86-97. (2012)

[258] Coltuc, D., Bolon, P., Chassery, J.M.: Exact histogram specification. IEEE Transactions on Image Processing. 15 (6). 1143-1152. (2006)

[259] Wan, Y., Shi, D.: Joint exact histogram specification and image enhancement through the wavelet transform. IEEE Transactions on Image Processing. 16 (9). 2245-2250. (2007)

[260] Nikolova, M., Wen, Y.W., Chan, R.: Exact histogram specification for digital images using a variational approach. Journal of Mathematical Imaging and Vision. 46 (3). 309-325. (2013)

[261] Nikolova, M., Steidl, G.: Fast ordering algorithm for exact histogram specification. IEEE Transactions on Image Processing. 23 (12). 5274-5283. (2014)

[262] Papadakis, N., Provenzi, E., Caselles, V.: A variational model for histogram transfer of color images. IEEE Transactions on Image Processing. 20 (6). 1682-1695. (2011)

[263] Nikolova, M.: A fast algorithm for exact histogram specification. Simple extension to colour images. Scale Space and Variational Methods in Computer Vision. 174-185. (2013)

[264] Nikolova, M., Steidl, G.: Fast hue and range preserving histogram specification: theory and new algorithms for color image enhancement. IEEE Transactions on Image Processing. 23 (9). 4087-4100. (2014)

[265] Häuser, S., Nikolova, M., Steidl, G.: Hue and range preserving rgb image enhancement (rgb-hp-enhance). Documentation for Matlab toolbox. Preprint (2015)

[266] Boccignone, G., Picariello, A.: Multiscale contrast enhancement of medical images. IEEE International Conference on Acoustics, Speech, and Signal Processing. 4. 27892792. (1997)

[267] Land, E.H., McCann, J.: Lightness and retinex theory. Journal of the Optical Society of America. 61 (1). 111. (1971)

[268] Adelson, E.H.: Checkershadow illusion. Available at http://persci.mit.edu/gallery/checkershadow. 2 (1). (1995)

[269] Rizzi, A., Gatta, C., Marini, D.: A new algorithm for unsupervised global and local color correction. Pattern Recognition Letters. 24 (11). 1663-1677. (2003)

[270] Palma-Amestoy, R., Provenzi, E., Bertalmìø, M., Caselles, V.: A perceptually inspired variational framework for color enhancement. IEEE Transactions on Pattern Analysis and Machine Intelligence. 31 (3). 458-474. (2009)

[271] Ferradans, S., Palma-Amestoy, R., Provenzi, E.: An algorithmic analysis of variational models for perceptual local contrast enhancement. Image Processing On Line. 5. 219-233. (2015)

[272] Provenzi, E., Caselles, V.: A wavelet perspective on variational perceptually-inspired color enhancement. International Journal of Computer Vision. 106 (2). 153-171. (2014)

[273] Bertalmìø, M., Caselles, V., Provenzi, E.: Issues about retinex theory and contrast enhancement. International Journal of Computer Vision. 83 (1). 101-119. (2009)

[274] Piella, G.: Image fusion for enhanced visualization: A variational approach. International Journal of Computer Vision. 83 (1). 1-11. (2009)

[275] Sugimura, D., Mikami, T., Yamashita, H., Hamamoto, T.: Enhancing color images of extremely low light scenes based on rgb/nir images acquisition with different exposure times. IEEE Transactions on Image Processing. 24 (11). 3586-3597. (2015)

[276] Pierre, F., Aujol, J.F., Bugeau, A., Steidl, G., Ta, V.Th.: Variational Contrast Enhancement of Gray-Scale and RGB Images. Journal of Mathematical Imaging and Vision. 57. 99-116. (2017)

[277] D'Apice, C., Kogut, P.I., Manzo, R., Parisi, A.: Variational Model with Nonstandard Growth Condition in Image Restoration and Contrast Enhancement. Submitted to Communications on Applied Mathematics and Computation. (2023)

[278] Jia, Z., Ng, M.K., Wang, W.: Color image restoration by saturation-value total variation. SIAM J. Imaging. Sci. 12 (2). 9722-1000. (2019)

[279] Ring, W.: Structural Properties of Solutions to Total Variation Regularization Problems. ESAIM: Mathematical Modelling and Numerical Analysis. 34 (4). 799-810. (2000)

[280] Wunderli, T.: On time flows of minimizers of general convex functionals of linear growth with variable exponent in BV space and stability of pseudosolutions. Journal of Mathematical Analysis and Applications. 364 (2). 591-598. (2010)

[281] Kohr, H.: Total variation regularization with variable Lebesgue priors. arXiv:1702.08807 [math.NA]. 2017

[282] Alaa, H., Eddine Alaa, N., Bouchriti, A., Charkaou, A.: An improved nonlinear anisotropic PDE with $p(x)$-growth conditions applied to image restoration and enhancement. Authorea. July 07. DOI: 10.22541/au.165717367.72990650/v1. (2022)

[283] Chen, Y., Levine, S., Stanich, J.: Image Restoration via Nonstandard Diffusion. (2014). figshare https://www.mathcs.duq.edu/tech-reports/tr04-01.pdf

[284] Bertalmío, M., Caselles, V., Provenzi, E., Rizzi, A.: Perceptual color correction through variational techniques. IEEE Transactions on Image Processing. 16 (4). 1058-1072. (2007)

[285] Alvarez, L., Lions, P.L., Morel, J.M.: Image selective smoothing and edge detection by nonlinear diffusion. SIAM J. Numer. Anal. 29. 845-866. (1992)

[286] Prasath, V.B.S., Urbano, J.M., Vorotnikov, D.: Analysis of adaptive forward-backward diffusion ows with applications in image processing. Inverse Problems. 31. 1-30. (2015)

[287] D'Apice, C., Kogut, P.I., Kupenko, O., Manzo, R.: On Variational Problem with Nonstandard Growth Functional and Its Applications to Image Processing. Journal of Mathematical Imaging and Vision. 65 (3). 472-491. (2023)

[288] Dautray, R., Lions, J.L.: Mathematical Analysis and Numerical Methods for Science and Technology. Vol. 5. Springer-Verlag. Berlin Heidelberg. 1985

[289] Diening, L., Harjulehto, P., Hästö, P., Růžiĉka, M.: Lebesgue and Sobolev Spaces with Variable Exponents. Springer. New York. 2011

[290] Zhikov, V.V.: Solvability of the three-dimensional thermistor problem. Proceedings of the Steklov Institute of Mathematics. 281. 98-111. (2008)

[291] Ambrosio, L., Caselles, V., Masnou, S., Morel, J.M.: The connected components of sets of finite perimeter. European Journal of Math.. 3. 39-92. (2001)

[292] D'Apice, C., Kogut, P.I., Manzo, R., Uvarov, M.: Variational model with nonstandard growth conditions for restoration of satellite optical images using synthetic aperture radar. European Journal of Applied Mathematics. 34 (1). 77-105. (2023)

[293] D'Apice, C., Kogut, P.I., Manzo, R.: On Coupled Two-Level Variational Problem in Sobolev-Orlicz Space. Differential and Integral Equations. DOI: 10.57262/die036-0708-621. Vol. 36. No. 7-8. 621-660. (2023)

[294] D'Apice, C., Kogut, P.I., Manzo, R.: A two-level variational algorithm in the Sobolev-Orlicz space to predict daily surface reflectance at LANDSAT high spatial resolution and MODIS temporal frequency. Journal of Computational and Applied Mathematics. DOI 10.1016/j.cam.2023.115339. Vol. 434. Article ID 15339. 1-23. (2023)

[295] Meyer, Y.: Oscillating Patterns in Image Processing and Nonlinear Evolution Equations. Univ. Lecture Ser. 22. AMS. Providence. RI. (2002)

[296] Lieu, L.H., Vese, L.A.: Image restoration and decomposition via bounded total variation and negative Hilbert-Sobolev spaces. Applied Mathematics & Optimization. 58. 167-193. (2008)

[297] Schönlieb, C.B.: Total variation minimization with an $H^{-1}$ constraint. Research Gate Publication. (2009)

[298] Chipot, M., de Oliveira, H.B.: Some results on the $p(u)$-Laplacian problem. Mathematische Annalen. 375. 283-306. (2019)

[299] Zhikov, V.V.: On variational problems and nonlinear elliptic equations with nonstandard growth conditions. Journal of Mathematical Sciences. 173 (5). 463-570. (2011)

[300] D'Apice, C., De Maio, U., Kogut, P.I.: An indirect approach to the existence of quasi-optimal controls in coefficients for multi-dimensional thermistor

problem. Contemporary Approaches and Methods in Fundamental Mathematics and Mechanics. Editors: Sadovnichiy, Victor A., Zgurovsky, Michael (Eds.). Springer. Chapter 24, 489-522. (2020)

[301] Kogut, P.I.: On optimal and quasi-optimal controls in coefficients for multidimensional thermistor problem with mixed Dirichlet-Neumann boundary conditions. Control and Cybernetics. 48 (1). 31-68. (2019)

[302] Evans, L.C., Gariepy, R.F.: Measure Theory and Fine Properties of Functions. CRC Press. 1992

[303] Kogut, P.I.: On approximation of an optimal boundary control problem for linear elliptic equation with unbounded coefficients. Discrete and Continuous Dynamical Systems, Series A. 34 (5). 2105-2133. (2014)

[304] Kogut, P.I.: Variational S-convergence of minimization problems. Part I. Definitions and basic properties. Problemy Upravleniya i Informatiki (Avtomatika). 5. 29-42. (1996)

[305] Kogut, P.I.: S-convergence of the conditional optimization problems and its variational properties. Problemy Upravleniya i Informatiki (Avtomatika). 4. 64-79. (1997)

[306] Kogut, P.I., Kupenko, O.P.: Approximation Methods in Optimization of Nonlinear Systems. De Gruyter Series in Nonlinear Analysis and Applications 32. Walter de Gruyter GmbH. Berlin. Boston. 2019

[307] Kogut, P.I., Leugering, L.: On S-homogenization of an optimal control problem with control and state constraints. Zeitschrift fur Analysis und ihre Anwendung. 20 (2). 395-429. (2001)

[308] D'Apice, C., De Maio, U., Kogut, P.I.: Boundary velocity suboptimal control of incompressible flow in cylindrically perforated domain. Discrete and Continuous Dynamical Systems. Serie B. 11 (2). 283-314. (2009)

[309] D'Apice, C., De Maio, U., Kogut, P.I.: Gap phenomenon in homogenization of parabolic optimal control problems. IMA Journal of Mathematical Control and Information. 25. 461-480. (2008)

[310] Manzo, R.: On Tikhonov Regularization of Optimal Neumann Boundary Control Problem for an Ill-Posed Strongly Nonlinear Elliptic Equation with an Exponential Type of Non-Linearity. Differential and Integral Equations. Vol. 33, No. 3-4. 139-162. (2020)

[311] Manzo, R.: On Nuemann Boundary Control Problem for Ill-Posed Strongly Nonlinear Elliptic Equation with p-Laplace Operator and $L^1$-Type of Nonlinearity. Ricerche di Matematica. DOI 10.1007/s11587-019-00439-x. Vol. 68. No. 2. 769-802. (2019)

[312] Kogut, P.I., Kohut, Ya., Manzo, R.: Existence Result and Approximation of an Optimal Control Problem for the Perona-Malik Equation. Ricerche di Matematica. DOI 10.1007/s11587-022-00730-4. 1-18. (2022)

[313] Black, M.J., Sapiro, G., Marimont, D.H., Heger, D.: Robust anisotropic diffusion. IEEE Trans. Image Processing. 7 (3). 421-432. (1998)

[314] Aubert, G., Kornprobst, P.: Mathematical problems in image processing: partial differential equations and the calculus of variations. 147. New York: Springer. (2006)

[315] Karami, F., Meskine, D., Sadik, K.: A new nonlocal model for the restoration of textured images. Journal of Applied Analysis and Computation. 9 (6). 20702095. (2019)